nature

https://doi.org/10.1038/s41586-020-2526-z

Supplementary information

A fabrication process for flexible single-crystal perovskite devices

In the format provided by the authors and unedited

Yusheng Lei, Yimu Chen, Ruiqi Zhang, Yuheng Li, Qizhang Yan, Seunghyun Lee, Yugang Yu, Hsinhan Tsai, Woojin Choi, Kaiping Wang, Yanqi Luo, Yue Gu, Xinran Zheng, Chunfeng Wang, Chonghe Wang, Hongjie Hu, Yang Li, Baiyan Qi, Muyang Lin, Zhuorui Zhang, Shadi A. Dayeh, Matt Pharr, David P. Fenning, Yu-Hwa Lo, Jian Luo, Kesong Yang, Jinkyoung Yoo, Wanyi Nie & Sheng Xu✉

Supplementary Information for:

A fabrication process for flexible single-crystal perovskite devices

Yusheng Lei[1*], Yimu Chen[1*], Ruiqi Zhang[1], Yuheng Li[1], Qizhang Yan[1], Seunghyun Lee[2], Yugang Yu[3], Hsinhan Tsai[4], Woojin Choi[5], Kaiping Wang[3], Yanqi Luo[1], Yue Gu[3], Xinran Zheng[6], Chunfeng Wang[7], Chonghe Wang[1], Hongjie Hu[1], Yang Li[1], Baiyan Qi[3], Muyang Lin[1], Zhuorui Zhang[1], Shadi A. Dayeh[1,3,5], Matt Pharr[2], David P. Fenning[1], Yu-Hwa Lo[3,5], Jian Luo[1,3], Kesong Yang[1], Jinkyoung Yoo[4], Wanyi Nie[4], Sheng Xu[1,3,5,8#]

[1]Department of Nanoengineering, University of Californian San Diego, La Jolla, CA 92093-0448, USA

[2]Department of Mechanical Engineering, Texas A&M University, College Station, TX 77843, USA

[3]Material Science and Engineering Program, University of Californian San Diego, La Jolla, CA 92093-0418, USA

[4]Los Alamos National Laboratory, Los Alamos, NM 87545, USA

[5]Department of Electrical and Computer Engineering, University of Californian San Diego, La Jolla, CA 92093-0407 USA

[6]Department of Physics, Tsinghua University, Beijing 100084, P.R. China

[7]College of Physics and Optoelectronic Engineering, Shenzhen University, Shenzhen 518060, P.R. China

[8]Department of Bioengineering, University of Californian San Diego, La Jolla, CA 92093-0412, USA

[*]These authors contributed equally to this work.

[#]Email: shengxu@ucsd.edu

Supplementary Discussion 1: The lithography-assisted-epitaxial-growth-and-transfer method.

With a set of unique optoelectronic properties[1-4], organic-inorganic hybrid perovskites have become an important material family for photovoltaics. Compared to their well-studied polycrystalline counterpart[5], single-crystal perovskites have shown higher carrier transport efficiency and stability due to lower defect concentrations[6-8]. Besides, their uniform orientations provide possible approaches to understand the orientation-dependent carrier behaviors[9-11], where the variations are ascribed to anisotropically distribute trap densities. Highly oriented near-single-crystal polycrystalline perovskite photovoltaics with the enhanced performance have been reported[12,13], indicating an exquisite control of crystal orientation can be an effective strategy to boost the photovoltaic efficiency[9,11], which is impossible to achieve in polycrystalline photovoltaics due to the random grain.

However, challenges for single-crystal perovskite photovoltaics remain in terms of material growth: no growth method has demonstrated simultaneous control over material thickness and area, or growth of a single crystal with a composition gradient[6,14], yet these are closely tied to photovoltaic performance. For optimal charge carrier collection efficiency in hybrid perovskite devices, a film needs to be sufficiently thin[15]; for practical device integration, the thin film needs to be grown over a reasonably large area.

So far, several attempts have been reported to control the crystal dimensions, such as mechanical cutting, roll-imprinting, and space confinement. However, those methods either lack precisely control in both the thickness and area or have strict substrate condition requirements. Single-crystal $MAPbI_3$-based photovoltaics was reported with 21% efficiency by the space confinement method[16]. However, clamping growth solutions between two holders for the crystal

growth into the nano/micro scale in a controllable way is challenging. Crystallization will always happen at the interface with the air by solvent evaporation, which disturbs the following thin crystal growth. Any solvent residues can result in serious interface hydration formation and dissolve the charge transport layers assembled during the thin film growth process[16]. The roll-imprinting method for fabricating single-crystal $MAPbI_3$ photovoltaics was reported with 4% efficiency[8]. Even though the thickness of as-fabricated single-crystal $MAPbI_3$ can reach 500 nm, the requirements on the printing substrate restrict the device structure to be lateral, which limits the performance of subsequent devices. Thin single-crystal $MAPbI_3$ films could also be fabricated by mechanical cutting and etching[17]. However, the thickness is still not considered to be sufficiently thin, and the wet chemical etching may damage the perovskites as well. More importantly, none of the existing crystal growth methods has achieved the material composition gradient, and thus the graded bandgap in hybrid perovskite crystals[18], despite its potential ability to maximize light absorption and enhance carrier collection efficiency.

To overcome those challenges, we report a solution-based lithograph-assisted-epitaxial-growth-and-transfer method. The general process of the growth/transfer method is presented in Fig. 1a and Supplementary Fig. 1a. Here, parylene (or polyimide, PI) is used as the transfer layer[19], and no metal or other electron transport layer/hole transport layer (ETL/HTL) layers are needed during the growth/transfer process. We fix the pattern geometry to be 1 μm by 1 μm, the thickness of parylene (or PI) can vary from 2 μm to 10 μm. One of the single-crystal perovskite substrates is placed into a polydimethylsiloxane (PDMS) growth mold and covered by a patterned parylene (or PI) layer. Before the growth, a freshly prepared $MAPbI_3$ gamma-butyrolactone (GBL) (1M) solution is evaporated under 80 ºC for 6 hours to achieve a near-saturated condition, which is used as the growth solution. Otherwise, because of the high

solubility of $MAPbI_3$ in GBL solvent, the growth solution will immediately dissolve parts of the single-crystal substrates and destroy the pattern.

For epitaxial single-crystal perovskite thin films growth, the as-prepared growth solution is heated up to a preset temperature. The growth mold is then placed into the pre-heated growth solution for a particular amount of growth time. Precise thickness, area, and shape control of the epitaxial single-crystal thin films can be achieved by adjusting the growth temperature, time, and the lithography layout. The design of the growth mask serves as the mechanism for controlling the thickness of the epitaxial layer.

During the growth process, the epitaxial single-crystal perovskites (e.g., $MAPbI_3$ or $MAPbBr_3$) grow three-dimensionally under the natural behaviors of this kind of material. No additional capping agents or physical covers are used to control its growth behavior. Initially, small crystals nucleate on patterned growth sites, each having an epitaxial relationship with the substrate. As growth continues, the small crystals gradually expand and merge, forming a monolithic single-crystal film. The overall growth process can be divided into four steps (Extended Data Fig. 1a). In step 1, photolithography has been applied to generate masks on the single-crystal perovskite substrate. The schematic cross-section shows that the width of the pattern (L_p) and the distance between the patterns (L_d) are about the same (L_p=L_d). If L_p is too large, it is impossible to peel off the epitaxial film because the connection between the epitaxial layer and the substrate is too strong. In step 2, the growth starts. The epitaxial crystals fill the pattern openings, until the horizontal level of epitaxial crystals and the top surface of the mask are about the same. In step 3, the epitaxial crystals are growing out of the pattern openings, where the growth rate in *x*-*y* directions ($r_{x\text{-}y}$), in principle, equals the rate in the *z* direction (r_z, $r_{x\text{-}y}$=r_z). Therefore, the grown lengths in all directions ($L_{x\text{-}y}$, L_z) are considered to be the same ($L_{x\text{-}$

$_y$=L_z). As the growth continues, adjacent crystals will start to merge. The thickness of such a merged thin film L_z is only half of the L_d. The smaller the designed L_d, the thinner the epitaxial film. In step 4, the epitaxial crystals fully merge into a continuous thin film and grow only in thickness.

Because the epitaxial nature of the growth process, all crystals grown from the individual exposed area have the same lattice structure, morphology, and orientation, which are all determined by the substrate[20]. When two adjacent epitaxial crystals are growing large enough to contact with each other, there will be no tilting or twisting of the lattice at the interface. Therefore, no grain boundaries will be formed when adjacent crystals are merging with each other.

The different stages during the growth/transfer growth process can be revealed by scanning electron microscope (SEM) images, which may better illustrate the merging of the epitaxial crystals (Extended Data Fig. 1b). Also, the high-resolution transmission electron microscope (TEM) image in Figure 1c can clearly reveal the chemical epitaxial relationship between the substrate and the as-grown thin film. X-ray diffraction (XRD) measurements in Figure 1d also serve as additional evidence that the epitaxial crystals have the same orientation as the substrate.

Additionally, it has also been found that the growth rate in different directions can be effectively tuned by using different growth temperatures and precursor concentrations (Extended Data Fig. 1c). At a low growth temperature, the growth rates in all directions are low because of the temperature-reversal growth behavior. The growth rate would be surface reaction controlled. Then the precursor molecules have sufficient time to diffuse and adsorb at the most energetically favorable locations. The tri-phase interface between the single-crystal perovskite, substrate surface, and the growth solution is more favorable for nucleation and growth than the bi-phase

120 interface between the single-crystal perovskite and the growth solution. Therefore, the precursor
121 molecules would prefer to adsorb at the tri-phase boundary, which contributes to the growth in
122 the *x*-*y* directions. This is also why in the literature, almost none of the freestanding bulk single
123 crystals has perfect cubic shapes. The footprint of these bulk single crystals on the substrate is
124 always larger than their heights[14,21,22]. The same analysis applies to the scenario when the growth
125 rate is low at a low precursor concentration. With the same pattern design, high growth
126 temperature and precursor concentration lead to vertically standing rods. Because of the high
127 growth rate under the high temperature and concentration, the crystals would quickly consume
128 the precursor molecules in their vicinity. The growth rate is diffusion controlled. Precursor
129 molecules would be depleted in between the crystals, and therefore the growth along the *x*-*y*
130 directions is slowed down due to the internal competition for precursor molecules. The growth
131 rate would be dependent on the precursor diffusion from the bulk solution, which is from the *z*
132 direction of the crystals. Fresh precursor molecules would first arrive at the top surface of the
133 crystals and thus contribute to the fast growth along the *z*-direction of the crystals.

134 After epitaxial growth, an in-plane rotation of the parylene (or PI) together with the top
135 epitaxial thin film is necessary to break the connected single-crystal micro-rods between the
136 epitaxial single-crystal layer and the single-crystal substrate; otherwise, directly lifting up the
137 epitaxial layer will break the epitaxial single-crystal layer.

138 The whole process can be divided in six steps (see Supplementary Fig. 1a for detailed
139 schematics). In step 1, a single-crystal perovskite substrate is placed into a PDMS growth mold
140 for epitaxial growth. The height of the substrate does not need to be the same as the depth of the
141 pattern in the mold. If the surface of the substrate is lower than the surface of the PDMS mold,
142 the epitaxial crystals will fill the gap first and then grow out. If the surface of the substrate is

higher than the surface of the PDMS mold, the attached soft mask can tightly cover the substrate. In step 2, a soft pre-patterned parylene (or PI) film is fixed with two glass holders on the two ends as a mechanical handle. Then, the mask is attached to the PDMS mold. In step 3, the growth solution is introduced to the growth mold for the epitaxial growth, with controlled temperature, time, and precursors. In step 4, the epitaxial single-crystal films can grow out of the mask with different thicknesses, morphologies, and compositions, depending on the growth conditions. In step 5, the top parts (i.e., the epitaxial film and the parylene or PI mask) need to be partially lifted up to separate the glass holder and the PDMS substrate. The rotational movement of the substrate is still restricted by the PDMS holder. In step 6, the parylene or PI-glass holder will be rotated to break the connection. The substrate will be detached from the growth mask.

Optical images in Supplementary Fig. 1b show the top (left) and the bottom (right) sides of the single-crystal $MAPbI_3$ after the in-plane rotation. The broken single-crystal micro-rods can be clearly seen in the soft transfer mask. XRD ω scan and photoluminescence (PL) measurements (Supplementary Fig. 1c and 1d) have also been used to further study the crystal quality before and after the in-plane rotation. From the XRD results, no obvious change can be found, indicating the crystal quality before and after the in-plane rotation is similar. PL measurements exhibit a comparable result, where the full-width-at-half-maximum (FWHM) values do not have a noticeable change before and after the in-plane rotation. Note that the PL measurements give narrower peaks from the bottom side compared with the top side, because the bottom surfaces are freshly broken from the bulky parts, whose defect levels are found to be much lower than the existing surfaces that have been treated by solvents[22,23].

After the in-plane rotation step, the following re-adhesion process can be divided into two types. For the simple transferring purpose, diethyl ether can be used as an assistant antisolvent

for transferring onto arbitrary substrates. It is worth to point out that the antisolvent for single-crystal perovskite transfer in this work is fundamentally different from that in depositing the polycrystalline perovskite, where the antisolvent is used to quickly wash the precursor solvent (e.g., dimethylformamide, DMF, and dimethyl sulfoxide, DMSO) to uniformly and rapidly crystallize the polycrystalline perovskite. In this work, the anti-solvent is to facilitate the transfer process in a more convenient way when no strong interfacial adhesion force is needed. The weak adhesion provided by the antisolvent is sufficient for experiments such as taking SEM images, measuring thickness-dependent properties, and characterizing the crystal quality of the transferred single-crystal film. As a commonly used anti-solvent in polycrystalline perovskite thin film deposition, diethyl ether has strong volatility and does not dissolve the perovskite. Therefore, diethyl ether can be used as a re-adhesion solvent.

The adhesion force between the perovskite single crystals and the substrates has been measured (Supplementary Fig. 2). It is clear to see that the simply attached single-crystal perovskite shows no adhesion at all (Supplementary Fig. 2b), indicating the Van der Waals contact and possible micro-gaps between two solids. Also, different antisolvents have similar adhesion forces (Supplementary Fig. 2c).

However, for device fabrication, a strong interfacial contact is critical. Therefore, it is necessary to spin coat a very thin layer of supersaturated growth solution onto the target substrate first, followed by transferring the single-crystal thin film onto the substrate and baking it under 80 ºC for 1 hour. The thin solution layer between the single-crystal thin film and the substrate will introduce a secondary re-growth process: the supersaturated solution will be gradually dried under heating, while new perovskites will be crystallized from the solution. The transferred single crystal film will serve as an epitaxial substrate for growing the new single

crystals. As the growth is going on, the new single-crystal perovskite can not only fill any micro-gaps between the two solids but also achieve strong adhesion with the substrate, in a similar way to the spin-coating process. The bonding introduced by the crystal growth has been proved to be able to exhibit a good adhesion with the substrate[24], and the measured strong adhesion force confirmed our analysis (Supplementary Fig. 2d).

Finally, the parylene (or PI) can be removed by dry etching or direct peeling off, depending on the thickness of the parylene (or PI) mask. For the dry etching of the parylene (or PI), O_2 (or Cl_2 and Argon) plasma serves as the etchant, which has been reported to damage perovskite by introducing a series of decomposition reactions[25]. Even though accurate etching power and time are needed to remove the polymer mask and minimize the plasma damage, surface decomposition after dry etching is inevitable. The surface after dry etching has to be cleaned to remove any decomposition residues. Here, a supersaturated $MAPbI_3$ GBL solution will be used to clean the surface by dynamic spin coating followed by 80 ºC baking for 1 min. Detailed changes in this step are presented in Supplementary Fig. 3. After the dry etching, periodic features can be seen from the SEM image (Supplementary Fig. 3a). The zoomed-in SEM image shows very rough morphology, which should be resulted from the plasma damage.

After washing the perovskite surface with the saturated GBL solution, the rough surface becomes very smooth without any noticeable particles or residues. By using the saturated solution, the perovskite will be minimally dissolved, but the non-perovskite materials can be quickly washed away by the GBL. atomic force microscopy (AFM) measurements confirm the observations by the SEM (Supplementary Fig. 3b). XRD ω scan and PL measurements also confirm the dramatic changes before and after washing the perovskite film with the saturated GBL solution (Supplementary Fig. 3c and 3d). Before the washing, the FWHM of the XRD

peaks is around 0.065, and the PL signals are very weak, indicating that the crystal quality has been degraded a lot by forming non-crystalline residues. However, the FWHM of the same sample after washing can be effectively reduced to be around 0.03, and the PL signals are much enhanced, showing that surface defects induced recombination has been largely reduced after washing.

A continuous growth system plays a critical role in realizing the graded single crystals. Otherwise, there will be clear structural interfaces of heterojunctions, which will serve as carrier recombination centers, decreasing the device performance[26]. The continuous growth system is realized by setting two pumping systems to the growth solution: one injects new precursors while the other extracts supernatant precursors (Extended Data Fig. 6a). A 20 mL container with an open hole is used to hold the growth solution. The open hole can drain unneeded precursors for realizing the continuously changed compositions in the growth solution. A single-crystal perovskite substrate in a PDMS holder is placed into the glass container. Then, perovskite precursor 1 is added into the container, where the top of the solution is at the same level as the bottom of the hole to make sure that the solution can be timely and effectively washed out. After that, a glass tube is inserted to the bottom of the container to serve as the feeding source of a different perovskite precursor 2 for changing the growth solution composition. The feeding speed is dependent on the growth speed (e.g., growth temperature, precursor concentration) and the container volume, and can change with different setups.

Here we are sharing our recipes as a reference: if a ~5 mm thick graded crystal needs 2 hours to grow at certain conditions, the whole solution (precursor 1) needs to be fully exchanged in 2 hours. With a container volume of 5 mL, the pumping speed should be 41.67 μl min^{-1}. If a high temperature/concentration and a smaller container are used, the growth time for 5 mm

thickness may be reduced to 1 hour. Using a volume of 3 mL, the pumping speed should be 50 μl min^{-1}. For very small thickness growth, the growth time is much shorter. If 0.5 mL 1 M solution is used under 80 ℃, then the pumping speed is 1 ml min^{-1} for growing a 2 μm thick film.

It is important to note that the injected new precursor (precursor 2) needs to be pre-heated to the same temperature as the growth condition. Otherwise, the freshly mixed solution during the precursor exchanging will not be able to reach the preset temperature, which makes it difficult to identify the real growth temperature. The lukewarm solution may also dissolve the already grown epitaxial single-crystal thin crystals/films. We can design different pumping speed to grow different gradient profiles. This method is applicable to general hybrid perovskites. Graded single-crystal perovskites can be grown with different ion combinations and ratios of cations and anions (Extended Data Fig. 6b).

Supplementary Discussion 2: Interfacial quality studies in the growth/transfer process.

The interfacial adhesion between different layers of materials in single-crystal perovskite electronic devices is one of the major challenges. In particular, the interface between single-crystal perovskite and other functional layers (e.g., ETL, HTL) can substantially determine the charge transfer and the device performance. Therefore, it is important to understand the interfacial quality in the growth/transfer process. In the growth/transfer process, there are two steps that involve the usage of solvents to treat the interface of the single-crystal perovskite thin films. The first is to do the re-adhesion/re-growth in the transfer process. The second is to wash the single-crystal perovskite surface after dry etching.

1. Re-adhesion/re-growth process.

In the re-adhesion/re-growth step, the supersaturated growth solution is firstly spin-coated onto the target substrate. Then, the peeled-off single-crystal $MAPbI_3$ thin film is attached to the supersaturated growth solution on the substrate. Finally, the entire system is placed onto a hotplate until full growth of new single crystals from the spin-coated supersaturated growth solution. In this whole process, the substrates are only playing as inert "holders" to mechanically support the spin-coated growth solution and are not chemically involved in the growth process. The substrates do not react with the solution or the perovskite materials. Therefore, the growth behaviors, crystal structures, and interface properties of single-crystal perovskite should not be influenced by the substrates. To clearly reveal the quality at the interface, systematic studies include TEM, XRD, optical topography, PL, temperature-dependent Hall mobility, time-resolved PL, trap density, transient photovoltage (TPV), transient photocurrent (TPC), adhesion force, and contact angle have been performed. Besides, different kinds of substrates have also been studied to qualify substrate independence. The detailed discussions can be seen below.

Different from the case of preparing polycrystalline perovskite films, the perovskite solution is spin-coated onto a substrate, followed by annealing, where the crystal quality has been proven to be substrate-dependent. The major reason is that those interfacial properties of the substrate can largely influence nucleation, growth, and formation of the perovskite and may cause an incomplete conversion from the precursor to crystals during the rapid deposition process[27-30]. However, the mechanism of preparing single crystals in this study is totally different. Unlike the rapid crystallization process in the spin-coating method, the process in this study is epitaxial growth, where the transferred single crystal thin film is serving as the real epitaxial substrate for interfacial crystal growth. The nominal substrate at the bottom is only providing the mechanical

support for the growth process. Therefore, the substrate properties should have minimal influences on the quality of interfacial crystals.

The overall crystal quality of the transferred single-crystal $MAPbI_3$ after the re-adhesion/re-growth process on different substrates has been studied by XRD and PL. XRD ω scan has been performed for the transferred single-crystal $MAPbI_3$ on different substrates (Supplementary Fig. 8a), whose FWHM is commonly used to evaluate the crystal quality[31-33]. It can be seen that the FWHM of the XRD peaks does not show noticeable changes with different kinds of substrates. PL measurements (Supplementary Fig. 8b) also exhibit similar results, where both the intensities and the FWHM of the peaks do not change with different substrates, indicating that the possibility of radiative recombination and the crystal quality are similar to each other[34].

However, substrates with different wetting behavior of the precursor solution will influence the adhesion force between the crystals and the substrate. If wetting is poor, even though the re-growth can still happen, the bonding between the single crystal and the substrate will be weak. Adhesion forces have been measured under good and poor wetting conditions on different substrates. Usually, the wetting is considered to be poor if the contact angle is between 90° and 180°, and good if the contact angle is less than 90° (Supplementary Fig. 9). The contact angle can be roughly controlled by adjusting the time for treating the substrate surface using ultraviolet light ozone (UV-ozone) or oxygen plasma. As long as the time of substrate treatment is enough, all substrates used in this study produce similarly high adhesion force of the single-crystal perovskite. For example, even though the PDMS surface is one of the most difficult substrates for achieving good wetting with the precursor solution, we found 10-min UV-ozone treatment to be enough to achieve good wetting. A good wetting condition can always result in a strong

adhesion force, regardless of the substrates. Good adhesion between the single-crystal perovskite and the substrate is necessary for achieving high-performance photovoltaic devices.

To reveal the interfacial crystallinity at the interface, interfacial cross-section of the crystals on different substrates has been studied by high-resolution TEM. Specifically, Au, glass, and PDMS substrates are chosen to represent metals, oxides, and polymers. The results can be seen in Extended Data Fig. 2. All of those high-resolution TEM results show distinct boundaries between the single-crystal thin film and the substrate, where no noticeable polycrystalline or amorphous structures can be found in the single-crystal $MAPbI_3$, indicating that the re-adhesion/re-growth process maintains the high-quality lattice structure of $MAPbI_3$. The reason is that the re-adhesion process is also an epitaxial growth process: during the re-adhesion process, the transferred single-crystal $MAPbI_3$ thin film actually serves as the real "substrate" to guide the epitaxial growth. The transferred single-crystal $MAPbI_3$ thin film, which will not be dissolved in the supersaturated solution, can be considered as a huge "seed crystal" to guide the epitaxial growth. At a relatively slow growth rate of the chemical growth compared with the rapid dynamic spin coating, it is favorable to form epitaxial single crystal from the supersaturated solution. Therefore, the re-growth process will always follow the epitaxy and maintain a high-quality lattice structure.

Additionally, hybrid perovskite includes organic and inorganic components. The results from the high-resolution TEM show only the inorganic framework. It is worthwhile to quantitatively investigate the influence of the sensitive organic component[35] on the trap and defect states.

(1) Thickness-dependent PL studies.

Thickness-dependent PL has been studied to investigate the interfacial crystal quality. Supplementary Fig. 4a shows the schematic setup: a transparent substrate (glass) has been used to perform the re-adhesion/re-growth process so that the confocal laser beam is able to access the interfacial area. A control device with a simple physical contact to the glass substrate has also been measured. With different focal levels, as shown in Supplementary Fig. 4b, the PL intensity decreases because of the self-absorption from deeper focal levels in the single-crystal perovskite. The corresponding FWHM of the PL peaks at different focal levels show that the interfacial regions in both devices have the largest FWHM (Supplementary Fig. 4c), indicating relatively lower crystal quality at the interface compared with those in the bulk. Such a relatively lower crystal quality at the interface can also be revealed from the thickness-dependent carrier lifetime, carrier mobility, crystallinity, and trap density (Extended Data Fig. 4b and 4c, and Supplementary Fig. 13).

The re-adhesion/re-growth device exhibits a slightly larger FWHM value than the control device near the interface, which means the re-adhesion/re-growth step reasonably degrades the interfacial crystal quality in comparison with naturally grown single crystals. The mechanisms are discussed in the following paragraphs.

(2) Hall mobility studies.

Hall mobility has been used to provide additional evidence for evaluating the interfacial crystal quality. In general, interfaces formed under different conditions can significantly influence the charge dynamics. Supplementary Fig. 5a shows the schematics of the measurement setup. A control device is fabricated by depositing four Au electrodes using E-beam evaporation on top of one surface of a single-crystal perovskite. The results in Supplementary Fig. 5b show

345 that the interfacial Hall mobility in the growth/transfer device exhibits a moderate loss and a
346 slightly larger variation compared with the control device.

347 To understand the mechanism of the interfacial mobility loss, temperature-dependent Hall
348 measurements have been used to study the interfacial scattering. In theory, the main factor for
349 determining the carrier mobility is the scattering: impurity scattering and phonon scattering,
350 which can be described by the Matthiessen's Rule[36,37]:

351 $$\frac{1}{\mu} = \frac{1}{\mu_{impurities}} + \frac{1}{\mu_{lattice}}$$

352 where μ is the actual mobility, $\mu_{impurities}$ is the mobility of the material if impurity is the only
353 source of scattering, and $\mu_{lattice}$ is the mobility of the material if phonon is the only source of
354 scattering. Normally, with an increasing temperature, phonon concentration increases and starts
355 to dominate the scattering. Theoretical calculations have already revealed that the mobility
356 in perovskite is dominated by phonon interaction at room temperature[38-41], where the relationship
357 between the mobility and the temperature is expected to be described by an inverse power-law
358 with $\mu \propto T^{-3/2}$. The effect of impurity scattering, however, decreases with increasing
359 temperature because the average thermal speeds of the carriers are increased. These two effects
360 operate simultaneously on the carriers through Matthiessen's rule: at lower temperatures,
361 impurity scattering dominates; while at higher temperatures, phonon scattering dominates.

362 From the measurements, all devices exhibit an inverse power-law temperature dependence
363 (Supplementary Fig. 5c). In the high temperature tetragonal phase, the power exponents are fitted
364 to be -1.46 and -1.44 for the control device and the growth/transfer device, respectively. The
365 power exponents being very close to -3/2 suggests that phonon scattering (in the form of a
366 deformation potential scattering) is dominating the charge transport in both tetragonal phases,

and the difference between the two devices is negligible. However, as the temperature decreases to around 150 K, the crystal undergoes a transition from the tetragonal phase to the orthorhombic phase with a relatively abrupt changing of mobility. After that, even though the mobility continues to increase with cooling, power exponents become smaller, around -0.47 and -0.33 for the control device and the growth/transfer device, respectively. The change of the power exponents associated with the phase transition suggests that the carrier scattering in the tetragonal and orthorhombic phases are governed by different mechanisms. The smaller power exponent obtained suggests an enhanced weight of impurity scattering, where such a phenomenon is more noticeable in the growth/transfer device, indicating an increased impurity scattering.

(3) Interfacial trap density studies.

Interfacial trap densities of a similar device setup have been measured to confirm the Hall mobility studies. The results are seen in Supplementary Fig. 6. Here, the SiO_2 layer is deposited by sputtering to control the measurement heights in the thickness direction of the single-crystal perovskite. The thicker the SiO_2 layer, the further the measured region is away from the interface. The results also show a similar trend to the Hall mobility studies, confirming that the re-growth step can slightly degrade the interfacial crystal quality, which is reflected by a higher trap density of the growth/transfer device.

Additionally, we measured the overall carrier lifetime and carrier mobility using TPV and TPC to estimate how the interfacial quality can influence the overall crystal properties. Supplementary Fig. 15b and 15c show the measurement results. The growth/transfer process can decrease the carrier mobility and lifetime by ~4-5%, which is considered to be insignificant. The

interfacial quality can be improved by surface/interface passivation to enhance the device performance.

Based on all studies above, we conclude that in the growth/transfer process, the substrates do not play a role more than a mechanical support. The as-transferred single-crystal $MAPbI_3$ thin film serves as the real "substrate" to guide the epitaxial growth. As long as the transferred single-crystal $MAPbI_3$ is not dissolved in the supersaturated solution, the subsequent re-growth/re-adhesion process will always result in the single-crystal structure rather than the polycrystalline structure at the interface. Although the interfacial crystal quality shows slight degradation because of a higher level of impurity scattering as evidenced by the temperature-dependent Hall mobility measurements, the physical lattice structure and the crystallinity near the interface of the growth/transfer device do not change. The measured electronic dynamics of the growth/transfer device are on par with those of the bulk single crystals.

2. The GBL solution washing process

In the GBL solution washing process after dry etching, the non-crystalline residues on the surface of the single-crystal film can be effectively removed (Supplementary Fig. 3). SEM and AFM studies confirm the dramatic change of morphologies. XRD ω scan and PL measurements confirm the dramatic change of crystal quality before and after washing the perovskite film with the saturated GBL solution. Detailed discussions can be seen in the Supplementary Discussion 1.

Supplementary Discussion 3: The scaled growth/transfer process.

The size of the single-crystal perovskite thin films can be scaled up by multiple transfer/fabrication. Additionally, refining the growth/transfer process can be effective in scaling up the thin film size. Basically, the growth/transfer process can be divided into three stages: 1.

Epitaxial growth; 2. Peeling off; 3. Transferring. The scale can be further increased by addressing the following aspects.

For the first stage of epitaxial growth, the larger size of the growth substrate and the patterned mask, the larger area of the epitaxial single-crystal perovskite film. The large size of the substrate can be achieved by enlarging the crystal growth time[42]. The single-crystal perovskite wafer of size 120 mm × 70 mm × 52 mm has been demonstrated[43]. The size of the parylene (or PI) patterned mask can be as large as what the stranded lithography process allows.

For the second stage of peeling off, the most critical thing is to avoid breaking the epitaxial single-crystal perovskite film. The larger the single-crystal thin film, the higher the possibility of forming cracks. When the single-crystal thin film is larger, the size of the connected micro-rods and the mask are also larger. Therefore, it will be more difficult to avoid bending during the in-plane rotation. In this study, the transfer yield is found to be lower with larger single-crystal thin films, because the larger single-crystal thin films are easier to be broken during the in-plane rotation process. Even though increasing the thickness of the mask layer can help, the size with acceptable yield is still within ~2 cm × 2 cm. To solve this problem, replacing the soft mask with a more rigid mask (e.g., Cu foil) is found to be effective. A patterned Cu foil (20 μm thickness, by laser drilling, Extended Data Fig. 3b) is used, which can realize ~5.5 cm × 5.5 cm single-crystal perovskite film. The rigid Cu mask can largely avoid bending during the in-plane rotation, which significantly reduces the possibility of breaking the epitaxial single-crystal perovskite.

Finally, for the stage of transferring, the only concern is that the mask should be able to be etched without damaging the perovskite. Soft masks such as parylene (or PI) can be easily dry-etched, which has minimal influence on the device performance, as discussed in the manuscript.

For rigid masks, e.g., the 20 μm Cu foil, the mask can be liftoff from the perovskite thin film after the transfer.

Besides, the scaled fabrication of single-crystal perovskite microstructure arrays is also feasible. Single-crystal perovskite-based light emitting diode (LED) devices have been fabricated (Extended Data Fig. 8a). The pixel size can be anywhere from 1 μm to 100 μm, with potential applications for flexible single-crystal perovskite LED displays with tunable color, high resolution, high stability, and high quantum efficiency.

Supplementary Discussion 4: Crystal quality after the growth/transfer method.

XRD, optical topography, and PL have been used to study the epitaxial single-crystal thin film fabricated by the growth/transfer method. During the growth/transfer process, there are two major factors that will influence the quality of the as-prepared single-crystal thin films: epitaxial growth and transfer/re-adhesion.

1. Epitaxial growth:

Because of the high solubility of perovskite in their growth solutions, the concentration/growth temperature of the solution used in the growth/transfer method is important. Too high concentrations/growth temperature will cause an inhomogeneous merging and result in an inhomogeneous monolithic surface, which is reflected as a wide FWHM in the XRD (Supplementary Fig. 11a-11c). In homo-epitaxial growth where there is no interfacial strain, such XRD peak broadening can be due to the small crystalline size, as explained by the Scherrer equation[44]:

$$\tau = \frac{K\lambda}{\beta cos\ \theta}$$

where τ is the mean domain size, K is the shape factor, λ is the wavelength of the X-ray, β is the

broadening at the FWHM, and θ is the Bragg angle. In a particular material, the domain size τ is inversely proportional to the β. Even though the sub-micrometer particles or crystallites in the inhomogeneous monolithic thin films show the same orientation, they represent small domains and result in the XRD peak broadening.

After optimizing the growth concentration/growth temperature, FWHM values in the XRD ω scan are studied to evaluate the mosaicity of the as-grown single-crystal perovskite thin films[45]. Comparable FWHM values from the as-grown single-crystal thin films with the corresponding bulk single crystals demonstrate their similar crystal qualities (Fig. 1d), which mean the growth/transfer process will not sacrifice the quality of the as-grown epitaxial single-crystal thin films. The growth/transfer method can potentially be applied to a general perovskite in the perovskite family with very different growth temperatures and crystallization conditions.

2. Transfer/re-adhesion:

Even though the growth process can be well-controlled, the single-crystal thin film quality can still largely degrade if a suitable transfer/re-adhesion process is not followed (Supplementary Fig. 11d-11f).

During the in-plane rotation, directly peeling off the epitaxial single-crystal films from one side will break it into many pieces (Supplementary Fig. 11e top). This is because of the unique growth process of the growth/transfer method: the epitaxial single crystals need to fill the pattern first before growing out of the parylene (or PI) mask layer to merge into a thin film. Therefore, the pattern in the mask layer is filled with single-crystal micro-rods that serve as the connection between the epitaxial thin film and the substrate. Such a connection is strong and needs to be broken before the transfer. Otherwise, the brittle single-crystal thin film can get easily broken. Therefore, the in-plane rotation is critical to break those micro-rods and avoid breaking the

epitaxial single-crystal during the transfer.

During the re-adhesion process, the concentration of the growth solution must be supersaturated. Otherwise, the growth solution will etch the single-crystal thin films quickly and may dissolve them partially, which lowers their crystallinity (Supplementary Fig. 11f).

The overall crystal quality fabricated by the growth/transfer is studied using PL with an excitation wavelength of 533 nm. A well-controlled single-crystal thin film can not only exhibit a similar PL spectrum, but also show an I_{PL}/I_E (PL intensity/laser emission intensity) that is close to the bulk crystals (Fig. 1e). However, a degraded single-crystal thin film shows a PL peak broadening and an unstable I_{PL}/I_E, similar to the polycrystalline thin film (Supplementary Fig. 12).

Supplementary Discussion 5: Diffusion length calculations.

The optimal thickness for the photovoltaic material needs to strike a balance between the photogenerated carrier diffusion length and optical light absorption length. To ensure efficient charge collection, polycrystalline perovskite films are usually made sufficiently thin. The existence of crystallographic structural defects within the grain and at grain boundaries, where defects serve as trap states causing serious charge recombination, can heavily limit the charge carrier diffusion length to be typically less than 1 μm[46,47]. Prior studies have demonstrated that this balance in spin-coated polycrystalline perovskite is attained for a material thickness of ~500 nm[48]. Recently, with an advanced non-solvent method to produce low-defect polycrystalline perovskite films, high-efficiency solar cells with thickness ~1.1 μm have been reported, where the thick films are found to be more efficient on light conversion[49]. On the other hand, it has been concluded that the incoming light should be mostly absorbed by the polycrystalline

perovskite with a thickness around 2 μm[50], indicating polycrystalline perovskite solar cells with a thickness 0.6~1 μm can efficiently collect the free carriers but do not make the best use of light.

As the single-crystal carrier dynamics and light absorption behavior are different from the polycrystalline[6], it is necessary to re-investigate the best thickness for an single-crystal absorber. According to the literature, the carrier diffusion length L_D can be calculated by[46]:

$$L_D = \sqrt{\frac{K_B \cdot T \cdot \mu \cdot \tau}{e}}$$

where K_B is the Boltzmann's constant, T is the temperature, μ is the carrier mobility, τ is the carrier lifetime, and e is the electron charge.

To calculate L_D for estimating a rough single-crystal perovskite thickness, the carrier mobility and lifetime are measured by time of flight (ToF) and time-resolved PL under 1-Sun intensity, respectively (Extended Data Fig. 4b and 4c). For the ToF measurement, all devices share the same Au/single-crystal perovskite/indium tin oxide (ITO) structure fabricated by e-beam evaporation and sputtering. By controlling the same deposition conditions for the ITO layer (power, time, and gas flow), possible plasma damage to the sample is controlled to be similar to each other.

The carrier mobility μ can be calculated from the carrier transit time by[22]:

$$\mu = \frac{d^2}{Vt}$$

where d is the thickness of the target region, V is the applied voltage, and t is the measured carrier transit time. The average carrier lifetime of the single crystals is measured by time-resolved PL[21].

Measured results show that both the carrier mobility and carrier lifetime are thickness-related and exhibit saturating tendencies, which indicate a "maximum" L_D if the film thickness increases to a certain level (Extended Data Fig. 4a). Usually, mobility will not change with different thickness. However, unlike well-established solvent engineering in polycrystalline perovskite thin film preparation, current perovskite single crystals grown by wet chemical methods are found to have high surface defect centers[22,23,51], which are orders of higher than those in polycrystalline films[52]. Additionally, thinner single-crystal films have a relatively higher surface-to-volume ratio, indicating that the surface can play an important role, especially when the surface properties are dominating. The reduced surface-to-volume ratio in thicker single-crystal films will result in a better overall crystal quality with higher carrier mobility and lifetime (Extended Data Fig. 4b and 4c).

To clearly exhibit such a property, thickness-dependent XRD, PL, and trap density[21] have been studied to quantitatively evaluate the crystalline quality of the epitaxial thin films (Supplementary Fig. 13). The FWHM values from both XRD and PL decrease with increasing the film thickness, indicating thicker films exhibit better crystal qualities. However, such changes seem to plateau from ~20 μm, where there is almost no change with further increasing the crystal thickness. To study the trap density, P-type devices have been fabricated with two Au electrodes by e-beam evaporation. Devices with different single-crystal thicknesses are measured. All samples are scanned under forward bias only with the same scan condition to avoid any influence of hysteresis, and all samples are disconnected for 6 hours to avoid the polarization influence from the previous scan to the next one[53]. The results also exhibit lower trap densities in thicker devices, which correspond to an overall better crystal quality. Therefore, the calculated carrier diffusion length shows a thickness-dependent phenomenon, which results from the

saturated carrier mobility and carrier lifetime because of the better crystal quality in thicker single-crystal thin films.

Supplementary Discussion 6: The in situ fabricated devices.

Different from the spin coating technique for preparing polycrystalline perovskite thin films, lithography steps have been carried in the growth/transfer process, so the nano/micro fabrication process needs to be considered as an influencing factor on the device performance. Generally speaking, the shape of the current density-voltage (*J-V*) curve can roughly tell the cell performance. Large series resistance can influence the short circuit current density (J_{SC}), but in that case, the shape of the curve is normally s-shaped. If the fill factor (FF) is moderate, the series resistance should be acceptable. However, the FF and open circuit voltage (V_{OC}) do not have a strong correlation. Relatively speaking, an FF greater than 75% can still have a low V_{OC}. The V_{OC} is highly related to the bandgap and interfacial recombination. While the bandgap is the same for all samples in this case, the interfacial recombination is sensitive to the surface defect states.

Perovskite single crystals grown by wet chemical methods are found to have high surface defect centers[22,23], which are orders of magnitude higher than those in polycrystalline films[52]. These surface defect states will mainly influence the *Voc*[54-61]. Even though many approaches have been established to passivate the surface/interface defects in polycrystalline perovskite[62-65], there is still a lack of strategy to passive single-crystal perovskites. Also, thinner devices have a higher surface-to-volume ratio than thicker devices, and are thus more prone to operational errors and easier to be influenced by the re-adhesion/re-growth and solution treatment (e.g., washed by the GBL saturated solution). Evidence can be seen in Supplementary Fig. 15b and 15c, where

569 TPC and TPV measurements are used to qualify the carrier lifetime and mobility changes after
570 washing the single-crystal perovskite with different thicknesses by the GBL saturated solution. It
571 is clear that the crystal quality in a thinner film is more easily influenced by surface treatments.
572 Therefore, to isolate the influence of fabrication steps on the quality of the crystal
573 surface/interface and thus the V_{OC}, particularly of the thinner films, devices based on the single-
574 crystal perovskite film without transferring (i.e., delamination, re-adhesion, or GBL washing)
575 have been fabricated. These in situ fabricated devices are used to characterize the V_{OC}, which are
576 shown in the inset of Figure 2b. The configurations of these in situ fabricated devices are kept
577 the same as Au/poly(bis(4-phenyl)(2,4,6-trimethylphenyl)amine) (PTAA)/single-crystal
578 perovskite/TiO_2/ITO, where PTAA is the hole transport layer patterned by photolithography and
579 etching, TiO_2 is the electron transport layer deposited by atomic layer deposition, and Au and
580 ITO are both electrodes deposited by sputtering (Extended Data Fig. 3). In such a structure
581 where no solvent treatment is applied, the influence of the fabrication steps on the V_{OC} is
582 minimized. Also, because there is only one surface (top surface) that experiences the solution
583 treatment, the V_{OC} values resulted from the in situ fabricated devices are more accurate and
584 revealing. So, we can study the dependence of V_{OC} on the single-crystal perovskite thickness in a
585 more accurate way and exclude the influence of other confounding factors from fabrication steps.
586 In the *J-V* curves of Figure 2b, the increase of V_{OC} from ~0.6 to ~2 μm is considered to be
587 because thicker films have better crystal qualities and are more immune to the fabrication steps
588 induced degradation in crystal quality. The decrease of V_{OC} beyond 2 μm can be explained by the
589 inset of Figure 2b. Without extra re-growth and solvent treatments, the single-crystal thin film
590 can keep its original best surface quality. A thicker film leads to a lower V_{OC}, which is due to the
591 interfacial charge accumulation caused by the weaker build-in field in the thicker films. Note that

592 even though in situ devices use a different structure from the growth/transfer devices, as long as
593 the structure of all in situ devices is the same, the conclusion of studying the thickness-dependent
594 V_{OC} is valid.
595
596 **Supplementary Discussion 7: The neutral mechanical plane (NMP) design and mechanical**
597 **simulations.**
598 The NMP is defined as a conceptual plane within a beam or cantilever. When loaded by a
599 bending force, the beam bends so that the inner surface is in compression and the outer surface is
600 in tension. The NMP is the surface within the beam between these zones, where the material of
601 the beam is not under stress, either compression or tension. Therefore, if a critical material (layer)
602 of interest is sufficiently thin and can be located in/near the NMP, the generated strain in the
603 material will be diminishingly small. As such, this approach provides a means of rendering the
604 nominally brittle single-crystal perovskite as flexible (Extended Data Fig. 5a left).
605 To design such a structure, a result from a simple one-dimension (1D) bending is first
606 implemented to provide insights into this system (Extended Data Fig. 5a right)[66]:
607 $$h = \frac{d_1E_1A_1 + d_2E_2A_2 + d_3E_3A_3}{E_1A_1 + E_2A_2 + E_3A_3}$$
608 where h is the distance from the bottom of the system to the neutral plane, d is the distance from
609 the bottom of the system to the middle plane of each individual layer, E is the Young's modulus
610 of the given layer, and A is the cross-sectional area.
611 In this study, the thickness of the middle single-crystal $MAPbI_3$ is 2 μm, and the modulus is
612 14 GPa; the thickness of the bottom polyethylene terephthalate (PET)/ITO is 70 μm, and the
613 modulus is 2 GPa. Other device component materials, including ITO, SnO_2, and Spiro-MeOTAD
614 are not discussed here to simplify the model. In addition to these layers, we first design a top

615 layer with a suitable modulus and thickness to locate the NMP at the middle of the single-crystal
616 $MAPbI_3$ layer. For flexible or wearable devices, an overall small thickness is preferred for better
617 conformability with nonplanar surfaces and a smaller form factor. Therefore, a thin top layer in
618 the NMP structure is highly desired, which suggests that the top layer should have a modulus
619 similar to or larger than that of the PET/ITO. Here, we use a mixture of PDMS and 1-methoxy-2-
620 propanol acetate (SU8) to form such a top layer. The purpose of mixing SU8 into the PDMS is to
621 increase modulus of the top layer. The resultant modulus of the SU8/PDMS is measured to be
622 around 2.5 GPa.

623 Based on these values and using the above equation, to locate the NMP at the center of the
624 perovskite layer ($h = d_2$) requires a thickness of 62 μm for the top SU8/PDMS layer. Also, for the
625 entire structure (PET/ITO/SnO_2/single-crystal perovskite/Spiro-MeoTAD/Au/SU8-PMDS),
626 because of the small thicknesses and generally symmetric positions of other additional layers, the
627 calculated NMP is still near the center of the perovskite layer, which indicates the simplified
628 structure is reasonable. This model provides a quick and simple approach to the initial design of
629 the multilayer stacks, as to place the critical components (i.e., the single-crystal $MAPbI_3$ layer)
630 near the neutral axis, thereby reducing the levels of strain it experiences during bending.

631 Still, discrepancies may arise between experimental observations and predictions from the
632 1D model, due to Poisson effects and large deformations of the system not accounted for in this
633 simple 1D bending equation. As such, to better design the system, we analyzed the full three-
634 dimension (3D) mechanical response of this system.

635 The commercial software package ABAQUS enables simulating the full 3D mechanical
636 response of the single-crystal perovskite devices. The composite layer (SU8/PDMS, single-
637 crystal perovskite, and PET) consists of 8-node linear brick elements (C3D8H). The simulation

638 implements values of the elastic modulus of SU8/PDMS, single-crystal perovskite, and PET of
639 2.5 GPa, 14 GPa, and 2 GPa, respectively. The simulation also implements linear elastic
640 constitutive models for each material but includes non-linear geometric effects (finite
641 deformation) to enable large out of plane deformation. In the simulations, the largest value of the
642 maximum principal strain is found to be near the edge of the single-crystal perovskite layer due
643 to 3D and Poisson effects. Computing this maximum value of strain at the critical radius of
644 curvature from the experiments (the one that induces fracture) allows for an estimation of the
645 failure strain of perovskite materials[67] (Supplementary Fig. 17). For our tested/simulated system,
646 this corresponds to a critical failure strain of ~0.36% for single-crystal perovskite layer, which
647 suggests this layer itself is quite brittle. Again, however, the overall system exhibits good
648 flexibility (maintaining mechanical integrity down to a bending radius of 2.5 mm) due to the
649 NMP design.

650 Finally, we should note, that in using these simulations, a few assumptions are made that
651 may not always be correct, depending largely on details of the fabrication process and the
652 experimental testing procedure:

653 1. Boundary conditions: In the 3D simulations, all layers are ideally attached, i.e., no slip or
654 de-bonding occurs. However, slip or de-bonding may occur during the experiments, e.g., if the
655 fabrication procedure does not lead to strong bonding between layers.

656 2. Input force (moment): Unlike in the experiments, a moment is applied to the device in the
657 simulation. As such, the resulting deformation in the simulation does not have a constant bending
658 radius of curvature along the length of the specimen.

659 3. Material parameters: The fabricated device may exhibit different material properties than
660 are used in the simulation (e.g., modulus of the perovskite). Likewise, the critical strain to cause

fracture may be different from what is reported (e.g., in the literature) and the actual material used in the experiments.

The results in Figure 4c do exhibit a discrepancy between the NMP structure and the completed device structure. Different from a bending radius of $r \sim 2.5$ mm in the NMP structure, the entire photovoltaic device exhibits a noticeable efficiency decrease at $r \sim 3$ mm. This difference in bending radius should be due to the influences introduced by the additional layers in the photovoltaic device, including ITO, SnO_2, Spiro-MeOTAD, and Au, even though those layers do not change much the overall NMP position of the single-crystal hybrid perovskite.

Supplementary Discussion 8: Bandgap measurements and calculations.

Ultraviolet photoelectron spectroscopy (UPS) measurements are carried out on graded single crystals with different growth time. Because the graded single crystal growth is under continuous solution exchanging, different growth time can result in different thicknesses and surface compositions. Thus, the surface bandgap at different growth time can represent the bandgap at different distances from the substrate interface of the graded bandgap single-crystal thin film.

In the UPS measurements, He I (21.22 eV) is used as the radiation source. The position of the electron affinity (Fermi level) *versus* vacuum is the difference between the high binding energy cutoff (Fig. 3b inset) and the He I radiation energy (21.22 eV). The position of VBM is the difference between the Fermi level and the low binding energy cutoff (Fig. 3b). Therefore, the location of the valence band maximum (VBM) can be calculated from the UPS measurements. Semi-log scale has also been plotted to double-check the cutting off positions[68,69], which can be seen in Supplementary Fig. 23. In the semi-log scale, there are no noticeable small

intensities either, suggesting that the determination of the onset should be accurate. Additionally, we carefully measure the onset again to get accurate calculations of the VBM in the semi-log scale. We also compare the difference between the linear-scale and semi-log scale, and the difference between them in this case is negligible.

To obtain the full band structure, the bandgap value also needs to be measured for calculating the conduction band minimum (CBM). The bandgap values are measured via ultraviolet–visible spectroscopy (UV–vis) in the reflection mode (Fig. 3c) and PL (Supplementary Fig. 20a). Since the UV-vis light will penetrate deeper into the crystal than the He-I, the UV-vis measurement represents an averaged bandgap of the different compositions within the penetration depth. To precisely measure the bandgap of a single composition in the graded structure, we use the growth solution, with the same composition as the surface of the crystal at a particular growth time, to grow a single composition epitaxial single-crystal thin film. The calculated entire band structure is presented in Fig. 3c.

Supplementary Discussion 9: First-principles density functional theory (DFT) calculations.

Structural and electronic properties of $MAPb_{0.5+x}Sn_{0.5-x}I_3$ are calculated using first-principles density functional theory (DFT). A 2 × 2 × 2 supercell of tetragonal $MAPbI_3$ are built to model Sn-doped $MAPbI_3$, which contains a total number of 384 atoms with 32 Pb atoms. The Pb atoms are substituted by Sn to build the $MAPb_{0.5+x}Sn_{0.5-x}I_3$ supercells with x decreasing from $x = 0.5$ to $x = 0$ in 0.125 decrements. This yields a total number of five structures. These structures are fully optimized and used to calculate the density of states (DOS) and electronic band structures.

DFT calculations are carried out using the Vienna Ab Initio Simulation Package (VASP)[70].

The core-valence interaction is described by the Projector-Augmented Wave (PAW) pseudopotential. The electron-electron exchange-correlation function is treated using the Generalized Gradient Approximation (GGA) parametrized by Perdew, Burke, and Ernzerhof (PBE)[71]. The wave functions are expanded in a plane-wave basis set with a cutoff energy of 400 eV. All structures are fully optimized until all components of the residual forces are smaller than 0.03 eV/Å. The convergence threshold for self-consistent-field iteration is set at 10^{-5} eV. The Brillouin zone of the 384-atom supercells is sampled by the Γ point for optimization. A denser *k*-point mesh of 2 × 2 × 1 is used for the static run. Electronic band structures are calculated along with the high-symmetrical points of body-centered tetragonal lattice[72].

With the Sn substitution, the Sn-I bonds are obviously shorter than the original Pb-I bonds. Therefore, the cell volume shrinks as Sn concentration increases. Extended Data Fig. 7a shows the calculated electronic band structures for $MAPb_{0.5+x}Sn_{0.5-x}I_3$ with increasing the Sn composition. The VBM for each structure is normalized to zero point. All structures show direct bandgaps at the Γ point. The bandgap energies calculated with GGA decreases as the Sn composition increases. Although GGA is well-known to underestimate the bandgap energy, it correctly shows a trend (relative energy) among models with similar crystal structures and chemical compositions. Electron and hole effective masses are fitted near the band edges by:

$$\frac{1}{m_e^*} = \frac{1}{\hbar^2}\frac{\partial^2 E_C}{\partial k^2}$$

$$\frac{1}{m_h^*} = \frac{1}{\hbar^2}\frac{\partial^2 E_V}{\partial k^2}$$

where m_e^* is the electron effective mass, m_h^* is the hole effective mass, $\hbar$ is the reduced Planck constant, E_C is the conduction band energy, E_V is the valence band energy, and k is the wavevector. As shown in Extended Data Fig. 7b, m_e^* barely changes, while m_h^* decreases as the

Sn concentration increases. This trend is obvious where the valence band becomes more dispersive from $x = 0.5$ to $x = 0$. The results indicate a smaller hole mobility as the Sn concentration increases in $MAPb_{0.5+x}Sn_{0.5-x}I_3$.

Further, to analyze the changes of band edges as a function of the Sn composition, we align DOS for the five $MAPb_{0.5+x}Sn_{0.5-x}I_3$ structures to Hydrogen 1s state in MA molecules. Because the discrete energy level of the hydrogen atom in MA molecules is highly independent on the band edge-derived states, the Hydrogen 1s state in MA molecules can be used as an energy reference to determine relative positions of band edges. In this case, the VBM continuously increases while the CBM barely changes as the Sn concentration increases (Extended Data Fig. 7c). This trend is in good agreement with our experimental results and indicates that the decrease of the bandgap as the Sn concentration increases is mainly induced by the increase of VBM.

Supplementary Discussion 10: Improved performance by the graded band structure.

To explain possible reasons for the enhanced performance in bandgap-graded single-crystal $MAPb_{0.5+x}Sn_{0.5-x}I_3$ photovoltaics, several experiments have been designed. The main reasons are found to be the enhanced J_{SC} and relatively high V_{OC}.

For the J_{SC}, it is due to the Sn doping, which results in reduced bandgap and exciton binding energy in comparison with the $MAPbI_3$[73,74]. Both the light absorption range and the excited carrier concentration in the $MAPb_{0.5+x}Sn_{0.5-x}I_3$ get enhanced, which leads to an enhanced output current. This phenomenon is reflected by the electron-beam-induced current (EBIC) and external quantum efficiency spectra (EQE) measurements. From the EBIC results, uniform current intensities exist in the $MAPbI_3$ and $MAPb_{0.5}Sn_{0.5}I_3$ while a gradient current intensity is measured in the $MAPb_{0.5+x}Sn_{0.5-x}I_3$. The reduced current in the Pb area is due to a broader bandgap and a

752 higher exciton binding energy. The uniform current intensity distribution in the single-crystal
753 $MAPbI_3$ and compositionally uniform $MAPb_{0.5}Sn_{0.5}I_3$ also serves as additional evidence for the
754 absence of twins or small angle grain boundaries during the expanding/merging growth process.
755 From the EQE measurements, the larger absorption range and higher current density of the
756 $MAPb_{0.5+x}Sn_{0.5-x}I_3$ than the $MAPbI_3$ indicate that the Sn doping decreases the bandgap and
757 therefore enhances the EQE.

758 For the V_{OC}, it is related to the bandgap and the recombination in a particular photovoltaic
759 structure[75-77]. Sn doping normally largely decreases the V_{OC} of the photovoltaics because of the
760 decreased absorber bandgap[73,78]. However, the V_{OC} in the $MAPb_{0.5+x}Sn_{0.5-x}I_3$ photovoltaics is
761 only slightly decreased from that of the $MAPbI_3$. To investigate the possible reason of the high
762 V_{OC} of $MAPb_{0.5+x}Sn_{0.5-x}I_3$, the carrier mobility and lifetime have been studied by ToF and TPV,
763 respectively. For the carrier mobility, it's clear to see that the mobility of the $MAPb_{0.5+x}Sn_{0.5-x}I_3$
764 has been improved to as high as that of the $MAPb_{0.5}Sn_{0.5}I_3$ (Fig. 3f inset), which is because of the
765 high intrinsic mobility in Sn-based hybrid perovskite[78]. For the carrier lifetime, even though
766 doping the Sn to Pb perovskite in a uniform composition single crystal normally largely
767 decreases the lifetime, the graded Pb-Sn single crystal exhibits a relatively long lifetime among
768 the three single crystals (Fig. 3f). Given the same (Au/single-crystal perovskite/ITO) device
769 structure in the measurements, such a large carrier lifetime in the $MAPb_{0.5+x}Sn_{0.5-x}I_3$ is because of
770 the graded bandgap of the $MAPb_{0.5+x}Sn_{0.5-x}I_3$. In the EBIC mapping in Fig. 3d, the interfacial
771 region of graded $MAPb_{0.5+x}Sn_{0.5-x}I_3$ (within ~20 nm from the interface with the substrate, whose
772 composition is very close to $MAPb_{0.5}Sn_{0.5}I_3$, see Supplementary Figure 27) always gives a higher
773 current signal than the compositionally uniform $MAPb_{0.5}Sn_{0.5}I_3$, which also suggest a lower local
774 recombination rate.

Compared with the typical absorber band structure, the graded band structure can have a positive influence on the carrier transport: we can divide the graded bandgap into innumerable individual bandgaps of an innumerable series of heterojunctions connected back to back. Each individual junction serves two functions: a light absorber and an ETL/HTL for its neighboring junctions. The latter function is absent in a typical single composition absorber. The recombination possibility of as-generated charge carriers in the absorber is largely suppressed[79,80], which leads to a relatively high V_{OC} in the $MAPb_{0.5+x}Sn_{0.5-x}I_3$ photovoltaics.

Supplementary Discussion 11: Improved bending stability of the single-crystal photovoltaics.

Researches have already studied the mechanical properties of perovskite in both polycrystalline and single-crystal structures[67,81-85]. Even though both are considered to be brittle, the modulus in the polycrystalline perovskite is founded to be slightly higher than that in the single-crystal perovskite[86], which may be because of the anisotropic mechanical properties in single crystals[87,88]. Therefore, single-crystals perovskite with smaller modulus promises better integration with the human body for wearable applications.

So far, the stability issue has been considered to be the most critical factor in hindering applications of perovskite devices[89-91]. Different from the polycrystalline structure in most of the current perovskite devices, the single-crystal structure has proved to have much better stabilities. In polycrystalline perovskite, O_2 and moisture can easily go through the entire thickness of the layer from the innumerable grain boundaries to react with the perovskite and degrade the device performance[92,93]. Polycrystalline perovskite devices have been widely studied for years, but their intrinsic stability problems are still not solved. Grain boundaries also contribute to a higher

defect density, a stronger carrier recombination, and an easier ion migration[94-100]. In flexible devices, multiple-time bending can inevitably deteriorate the grain boundaries, potentially increasing the charge transfer barrier and carrier recombination rates, and accelerating material degradation[97,99,101-103]. However, grain boundaries are absent in single-crystal perovskites, suggesting that flexible devices made of single-crystal perovskites may exhibit enhanced device lifetime and stability.

This hypothesis is tested and confirmed by experimental data. Polycrystalline photovoltaics show significant performance degradation under the same cyclic bending tests (Supplementary Fig. 31), which may be caused by fast material and device degradation at the grain boundaries during bending. Single-crystal devices of the same device configuration exhibit much better stabilities under cyclic bending tests, indicating noticeable advantages of flexible devices based on single-crystal perovskites.

To further prove this conclusion, cycling-dependent material properties have been studied by using XRD ω scan and lateral current -voltage (*I-V*) characterizations (Supplementary Fig. 32). The size of polycrystalline and single-crystal films, and the two Au electrodes deposited by e-beam evaporation, are fixed to be the same for all devices. Lateral conductivity of the polycrystalline film after 300-time bending at a radius of 5 mm decreases to be only 31.1% of the intact one. In contrast, lateral conductivity of the single-crystal film still maintains 83.7% of the intact one, indicating a lower charge transfer barrier in the single-crystal film generated by the cyclic bending. XRD ω scan results support this conclusion. The FWHM of the polycrystalline film after bending becomes larger while the peaks from the single-crystal film does not change noticeably, which evidently indicates that single-crystal thin films are more resistant to fatigue. Consider the same operational conditions, such a difference is attributed to the deteriorated grain

boundaries (increased series resistance) and the degraded materials (e.g., impurities, ion migration, and decomposition) in the polycrystalline thin film in comparison to the single-crystal film.

Considering the high intrinsic structural defects and the instability issue of polycrystalline perovskite, replacing polycrystalline films with single-crystal films for flexible devices may provide a way for better device performance and longer device lifetime.

Supplementary Discussion 12: Photovoltaic device performance tests.

Each single-crystal photovoltaic device (0.5 cm × 0.5 cm) in the array is individually measured with a shadow mask. If not specified, all tests are using one $MAPb_{0.5+x}Sn_{0.5-x}I_3$ single-crystal photovoltaic device in the array without bending. The device in the center of 5 by 5 array is selected to do all of the measurements. The polycrystalline photovoltaic devices are also coated with SU8/PDMS top layers for fair comparisons. All tests (except the stress stability tests) are under constant 1-Sun from a standard solar simulator source with air mass 1.5 global filters. A 10 min light soaking is applied to all of the measurements. A small desktop fan is used to dissipate the heat generated by illumination.

In the stability comparison tests between the single-crystal and polycrystalline photovoltaics (Fig. 4d-4f), two compositionally uniform polycrystalline films (i.e., $MAPbI_3$ and $MAPb_{0.5}Sn_{0.5}I_3$), and a graded Pb-Sn single-crystal film are used, because there is currently no method to deposit graded polycrystalline films. We adopt the same HTL/ETL contact interfaces for the polycrystalline photovoltaics as the graded single-crystal photovoltaics, because the interfaces are paramount in photovoltaic device performance and stability[30,104]. For the thermal stability, the devices are all completed with PET and PDMS encapsulation. Then, the devices are

844 placed into an oven for aging. Because all devices are encapsulated, the humidity condition
845 should not be an influential factor. The aging time for the thermal tests is two hours. For the
846 humidity tests, the devices are not encapsulated, and the aging time is 30 mins because otherwise
847 the oxidation of Sn^{2+} can rapidly dominate the degradation mechanism.

848 The humidity control can be realized by calculation from the water vapor pressure
849 according to the thermodynamic equilibrium with condensed states, which can be controlled by
850 adjusting the amount of water in the air in a sealed space. The saturated water vapor pressure
851 look-up table is used to calculate the needed amount of water for different humidity at a certain
852 temperature, which can be applied to control the relative humidity. A glass box is used as the
853 confined space, where different amounts of water are added. Then, the box is placed into an oven
854 to keep the temperature to be 30℃ until the water is fully evaporated. In this way, the relative
855 humidity in the glass box can be designed accurately at different levels. For example, from the
856 look-up table, the saturated vapor pressure of water under 30 ℃ can be found to be 0.0042 MPa,
857 which means that at 30 ℃, 100% relative humidity refers to a partial pressure of water vapor of
858 0.0042 MPa. Therefore, the volume ratio of water vapor is 4.2%. If the relative humidity is 70%,
859 the total volume of water vapor in a container of 1 m^3 size will be 4.2% × 70% × 1000 = 29.4 L,
860 which is 21.0 g (according to the condition at 30 ℃). In our study, we need to add 0.00265 g
861 water (2.62 μl) into a 125 cm^3 glass box to achieve a 70% humidity. Similarly, if the relative
862 humidity is 30%, the total volume of water in 1 m^3 container will be 4.2% × 30% × 1000 = 12.6
863 L, which is 9.0 g (according to the condition at 30 ℃), and the amount of the water we need to
864 add to a 125 cm^3 glass box will be 0.00114 g (1.12 μl). In the experiments, to avoid additional
865 background humidity from the natural environment before the experiment, the glass box will be

placed into an oven at 100 ℃ for overnight to create a dry environment. A portable commercial humidity sensor is attached to the internal wall of the glass box for calibration purposes.

For the long-time stability tests, all of the devices are stored in a dark dry box for monthly measurements.

Supplementary Discussion 13: Stability of the single-crystal photovoltaics in continuous JV measurements.

Maximum power point tracking under continuous 1-sun illumination has been performed to study the device stability. A small desktop fan is used to dissipate the heat generated by illumination. The results are summarized in Extended Data Fig. 10.

From the measurement results, all devices show a relatively rapid degradation during the first 100 hours, followed by steady degradation rates. In contrast to the shelf-stability in the Figure 4f, where the single-crystal devices are much more stable than the polycrystalline devices, continuous illumination tests show similar degradation rates among these devices, even though the single-crystal structure has better material stability against moisture, heat, O_2, and strong light intensity (Figure 4d, 4e, Extended Data Fig. 9, and Supplementary Figs. 34, 35, 41). Additionally, continuous illumination tests can easily degrade the device performance even within a short time by comparing it with the shelf-stability test (Figure 4f). Therefore, the major degradation mechanism under continuous illumination may not be from the perovskite material, but from the Spiro HTL layer. Even though a small fan is used, the continuous illumination tests can still generate a lot of heat, which accelerates the degradation of the Spiro molecules with thermal and light instability[105-107]. The Spiro material becomes the bottleneck for the device stability, rather than the perovskites.

Therefore, the Spiro has been replaced with PTAA for the continuous illumination tests again. Device performance using PTAA is not comparable with that using Spiro. Although the V_{OC} is moderate (average ~1.01 V), the FF (average ~0.68) and the current density (average ~19-20 mA cm^{-2}) of PTAA based devices are always lower than those of Spiro based devices. Normalized power conversion efficiency (PCE) shows a fair comparison among these PTAA based devices (Supplementary Fig. 36). After replacing the Spiro with PTAA, the differences among those curves are more pronounced, because the HTL becomes less of a bottleneck for the device stability. The single-crystal devices exhibit a much slower degradation rate than those of the polycrystalline devices, indicating that the single-crystal structure has a better stability than the polycrystalline structure. Given the same device structure and the same ETL/HTL, such differences in the stability between single-crystal and polycrystalline devices are considered to be from the reduced ion migration in single crystals[108]. Unlike conventional photovoltaic materials, perovskites are appreciable ionic solids, which can be directly reflected by continuous *I-V* or *J-V* measurements. The ion migration has been shown to contribute to the degradation of perovskite photovoltaics[109], even though the exact mechanisms are still debatable[110]. For example, reactions between HTL/ETL layers and migrating I^- can cause barriers for carrier injection that quickly decreases the device performance[111]. The ion migration can also lead to the formation of a local electric field in the perovskite material to deprotonate the organic cations[112]. Theoretical calculations predict activation energies of between 0.08 and 0.58 eV for the migration of I^-, between 0.46 and 1.12 eV for MA^+, and between 0.8 and 2.31 eV for Pb^{2+}, respectively[113-115]. Both anions (I^-) and cations (MA^+, Pb^{2+}) can migrate due to the presence of vacancies, interstitials, and anti-site substitutions[116]. However, because levers of those defects

are lower in the single-crystal perovskite than the polycrystalline perovskite, such ion migration and thus device degradation are largely suppressed[95].

Supplementary Discussion 14: Stability differences between single-crystal Pb-Sn photovoltaics and polycrystalline Pb-Sn photovoltaics.

Usually, excessive Sn in Pb-Sn perovskite can significantly lower the V_{OC}[117], switch the Sn^{2+} oxidation routes[118], and decrease the decomposition enthalpies to accelerate the material degradation. The oxidative tendency of Sn^{2+} to Sn^{4+} in Sn-based perovskite can rapidly degrade the device as typically seen in the polycrystalline $MAPb_{0.5}Sn_{0.5}I_3$ devices. In this work, the single-crystal $MAPb_{0.5+x}Sn_{0.5-x}I_3$ devices show much better stability than the polycrystalline devices. Several possible reasons for the slower oxidation rate from Sn^{2+} to Sn^{4+} in the single crystal are discussed below.

1. Encapsulation

The device is fully encapsulated in the glove box by both top and bottom polymer layers (PET and PDMS/SU8). Those polymers serve as not only strain releasing layers for enhancing the flexibility, but also as encapsulation layers for keeping the material away from O_2 and moisture. The encapsulation may be the most important reason for inhibiting the Sn^{2+} oxidation.

2. Mixed Pb-Sn system

In contrast to the pure Sn-based perovskite photovoltaics, replacing Sn with 50−85% of Pb produces PCEs ranging from 12 to 17% and moderate stability[118-123]. Even though the exact mechanism is still not very clear, one possible explanation has recently been proposed: the oxidation mechanism in the Pb-Sn system is different from that in the pure Sn system[118,123-125]. In pure Sn-based perovskites, the main oxidation product is SnO_2 and SnI_4. However, by

incorporating Pb into Sn-based perovskites, the oxidation proceeds in a different route, and the main I-containing product becomes I_2 rather than SnI_4 in the case of the pure Sn system.

The formation of SnI_4 and SnO_2 involves the cooperative action of several Sn-I octahedra, where the I ions bonded to one Sn cation can be transferred onto adjacent Sn cations with which the I was shared. Pb, however, cannot be easily oxidized to Pb^{4+} and is unlikely to form PbI_4. Hence, if many of the Sn sites are occupied by Pb, the cooperative mechanism is far less favorable. Instead, I_2 is formed, and this requires three times as many Sn−I bonds to be broken, which can be expected to be slow. Therefore, the surrounding Pb atoms can stabilize Sn^{2+} and slow down its oxidation. Such an effect will be more pronounced when the percentage of Pb atoms is higher.

Both experimental and theoretical studies have been carried out to further understand the improved stability in Pb-Sn single-crystal perovskites. Absorption measurements on Pb-Sn based single-crystals and purely Sn-based single-crystals after one-day stress aging under 100 ℃ are used to understand the oxidation product as well as the chemical degradation route. The samples are dissolved into the GBL solution. The results are in Supplementary Fig. 38. The degradation products for $MASnI_3$ and $MAPb_{0.5}Sn_{0.5}I_3$ are very different: the compound for purely Sn-based perovskite is SnI_4, while that of the lead-containing compound is I_2. The measured different oxidation products in those two perovskite systems can be explained by different oxidation reaction routes[118]:

$$MA(Pb:Sn)I_3 + (n_1)O_2 = (n_2)MAI[g] + (n_3)SnO_2 + (n_4)PbI_2 + (n_5)I_2[g] \quad (1)$$

$$MA(Pb:Sn)I_3 + (n_1)O_2 = (n_2)MAI[g] + (n_3)SnI_4[g] + (n_4)SnO_2 + (n_5)PbI_2 \quad (2)$$

In the purely Sn-based perovskite, because of the strong SnI_4 signal in the absorption spectrum, the oxidation mechanism is more likely to be the reaction (2). The reaction (1) is considered to be the mechanism for the Pb-Sn perovskite.

To double confirm this conclusion, we also calculate the decomposition enthalpies in both reactions with different Pb to Sn ratios. From the calculation results (Supplementary Fig. 39), reaction (1) is energetically more favorable than reaction (2) for the Pb-Sn perovskite at any Pb to Sn ratios, indicating that the Sn^{2+} oxidation naturally prefers to happen through reaction (1), where all of the Sn-I bonds need to be broken. Therefore, compared with the purely Sn perovskite, the breaking of Sn-I bonds in the Pb-Sn perovskite is much slower, suggesting that the Pb inclusion can make Sn^{2+} oxidation slower in the perovskite.

To triple confirm the conclusion, x-ray photoelectron spectroscopy (XPS) measurements have been used to study the Sn^{2+} to Sn^{4+} ratio in perovskites to qualify the oxidation speed of Sn^{2+} (Supplementary Fig. 40). Increasing Pb can dramatically inhibit the oxidation speed of Sn^{2+} in the single-crystal perovskites, which serves as additional evidence for supporting the different oxidation mechanisms between purely Sn and Pb-Sn based perovskites. What's more, we dissolve $MAPb_{0.5+x}Sn_{0.5-x}I_3$ single crystals in GBL and use the solution to prepare the polycrystalline thin film to reveal its composition. By studying the Sn^{2+} to Sn^{4+} ratio using XPS, the Sn ratio should be between 0.2 to 0.3, where the oxidation speed is considered to be much slower than the purely Sn-based perovskite.

3. Single crystal.

The single-crystal structure is also a major reason for the improved stability, which has been widely proved to have much better stability in solar cells and photodetectors[16,23,126-128]. First, single-crystal perovskites have much lower defect densities than their polycrystalline structures.

I_2 is believed to be the most critical by-product and will cause self-degradation[129]. The formation of I_2 requires ion migration facilitated by structural defects. The well-align lattice structure of single crystals provide much lower possibilities for the formation of I_2.

Second, there is no grain boundary in single crystals, which indicates that the reaction routes are heavily inhibited. For the Sn-based polycrystalline perovskite, O_2 can relatively easily go through the entire layer via the innumerable grain boundaries. The degradation routes can not only come from the self-doping of Sn^{4+}, but also from the grain boundaries facilitated Sn^{2+} oxidation in the entire layer. However, in the single-crystal structure, the O_2 can only react with the single crystal surface, and only the formed Sn^{4+} and other impurities can further drive the degradation by self-doping from the surface to the bulk parts. Comparing these two oxidation approaches, we think the self-doping oxidation will be much slower than the direct reaction with O_2. Due to the cutoff of the O_2 oxidation route, the degradation rate in single-crystals is highly inhibited.

To test this hypothesis, both single-crystal $MAPb_{0.5}Sn_{0.5}I_3$ and polycrystalline $MAPb_{0.5}Sn_{0.5}I_3$ have been measured by XPS. The samples are all prepared in a glove box and are aged under the same environment outside the glove box. The measured results show that the fresh polycrystalline $MAPb_{0.5}Sn_{0.5}I_3$ exhibits strong Sn^{4+} peaks (Supplementary Fig. 41). Oxidation may have happened during sample transfer and loading. On the other side, the single-crystal $MAPb_{0.5}Sn_{0.5}I_3$ sample shows negligible Sn^{4+} peaks, indicating that the oxidation speed in the single-crystal sample is much slower than that in the polycrystalline. Therefore, the innumerable grain boundaries in the polycrystalline provide direct pathways for the O_2 to react with the Sn^{2+}. However, in the single-crystal, only the surface part can be oxidized by the O_2,

1000 and further oxidation of the bulk parts more depends on self-doping, which is much slower than
1001 the direct O_2 oxidation.

1002 What's more, *in-situ* XPS depth profile studies by ion milling have also been carried out to
1003 further understand the difference between single-crystal $MAPb_{0.5}Sn_{0.5}I_3$ and polycrystalline
1004 $MAPb_{0.5}Sn_{0.5}I_3$ (Extended Data Fig. 9). In the single-crystal sample, the Sn^{4+} is mainly formed at
1005 the surface of the single crystal, and the deeper bulk parts still keep Sn^{2+}. However, in the
1006 polycrystalline, even though the Sn^{4+} ratio in deeper bulk parts is reducing, the oxidation speed is
1007 much higher than that in the single-crystal.

1008 To summarize, the rapid oxidation of Sn^{2+} in polycrystalline perovskites is because of the
1009 existence of grain boundaries, which provide a direct pathway for the O_2 to diffuse through the
1010 entire material. Because of the high-quality crystal structure, single-crystal perovskites do not
1011 have those direct oxidation pathways, and the self-doping mechanism is determining the
1012 oxidation rate, which is much slower than reacting with the O_2.

1013

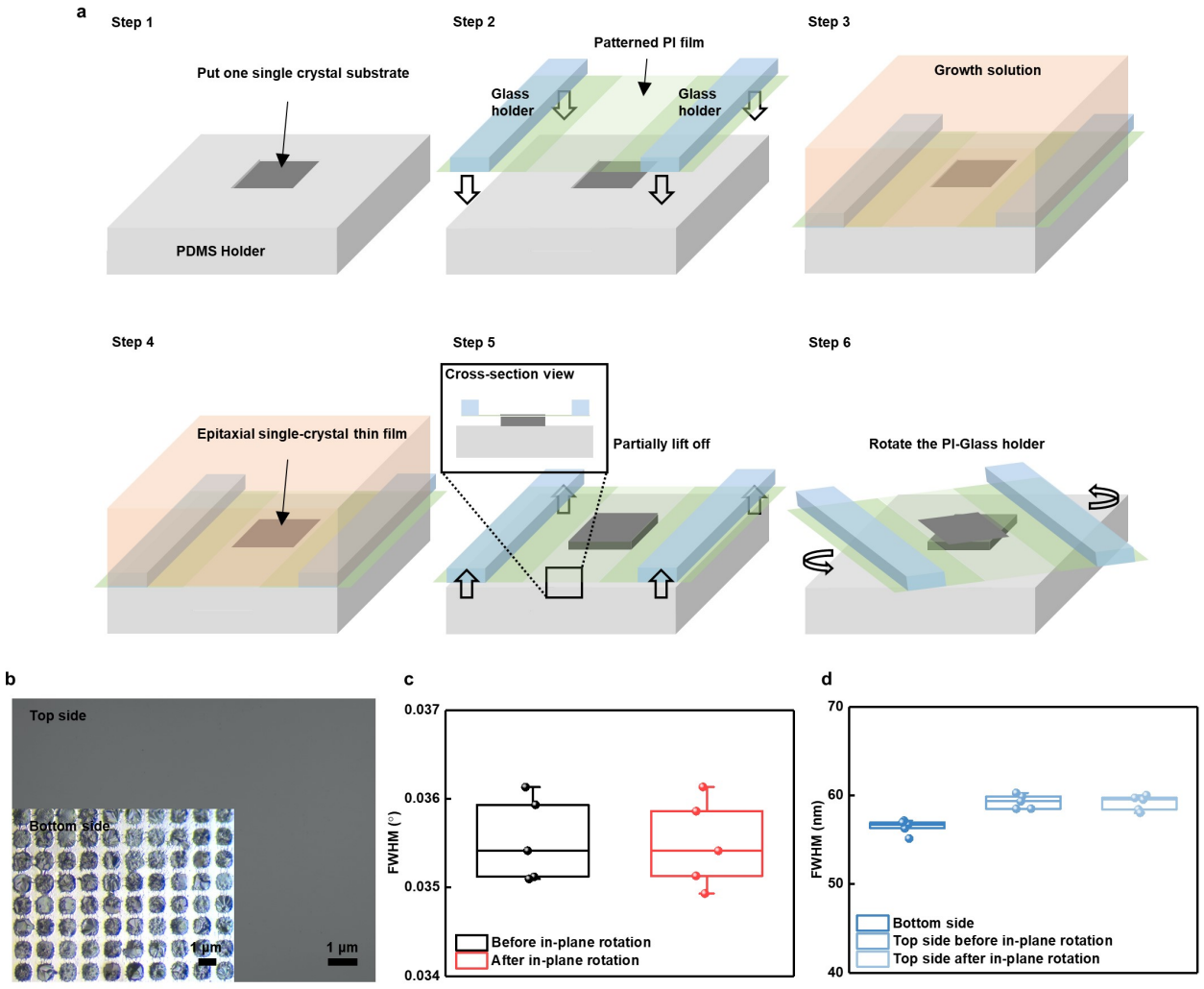

Supplementary Fig. 1 | The growth/transfer process and quality studies of detached single-crystal $MAPbI_3$ thin films. a, detailed schematics of the growth/transfer process. Critical components in each step are labelled. **b**, Optical images show the single-crystal $MAPbI_3$ after in-plane rotation. The inset image shows the bottom surface with the PI mask, where the broken micro-rods can be clearly seen. FWHM results from **c,** XRD ω scan and **d,** PL measurements of the single-crystal $MAPbI_3$ before and after in-plane rotation.

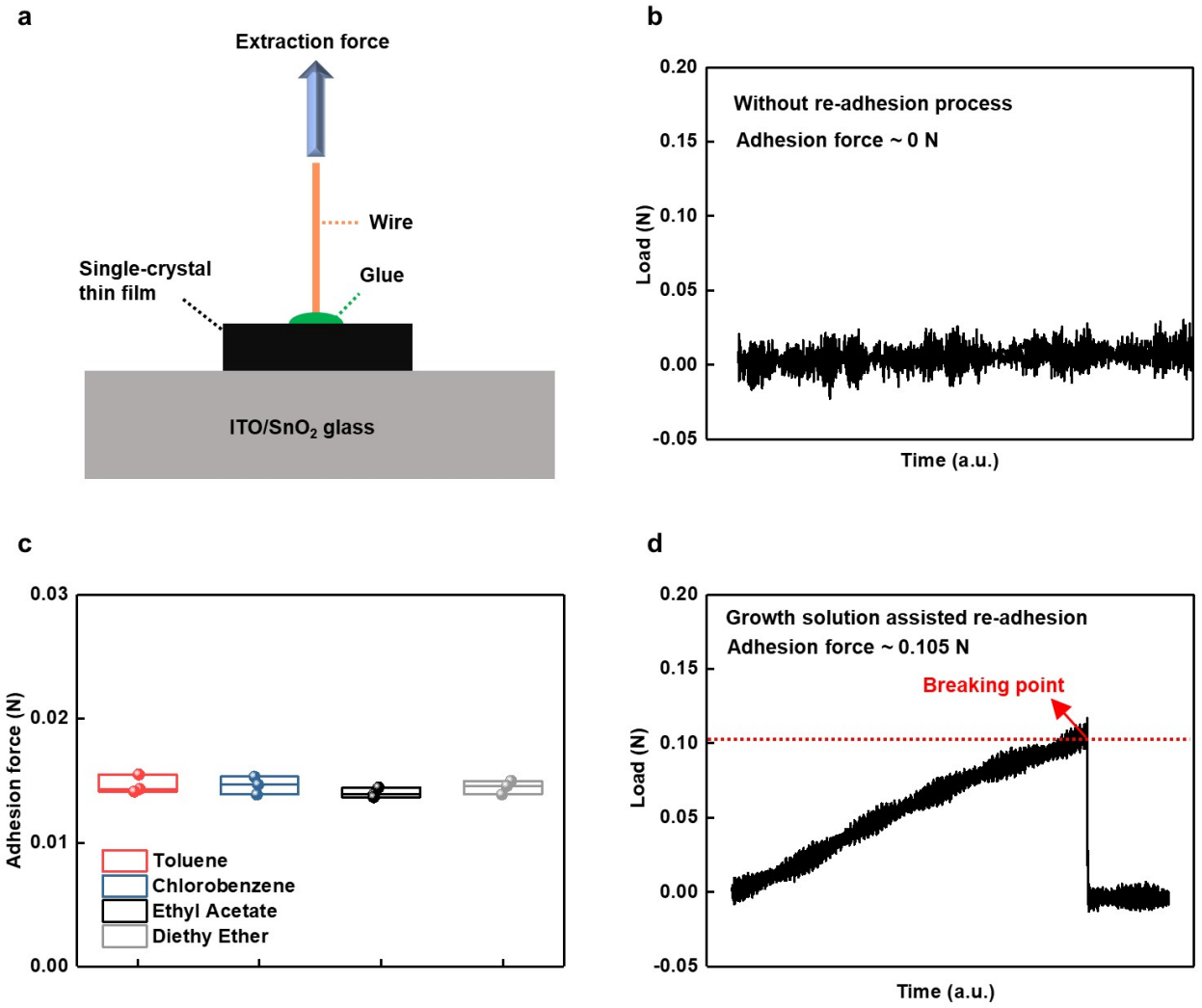

Supplementary Fig. 2 | The adhesion force measurement. a, The schematic testing setup for the adhesion force measurement. A Cu wire is fixed onto a single-crystal thin film for applying an external force. **b**, No adhesion force can be measured without a solvent-assisted re-adhesion process. **c**, Commonly used antisolvents for preparing hybrid perovskites are tested in the transferring process. No obvious difference in the adhesion force to the substrate can be observed, which are all relatively weak. **d**, For the growth solution assisted re-adhesion, delamination happens when the external load reaches ~0.105 N, which indicates good interfacial contact.

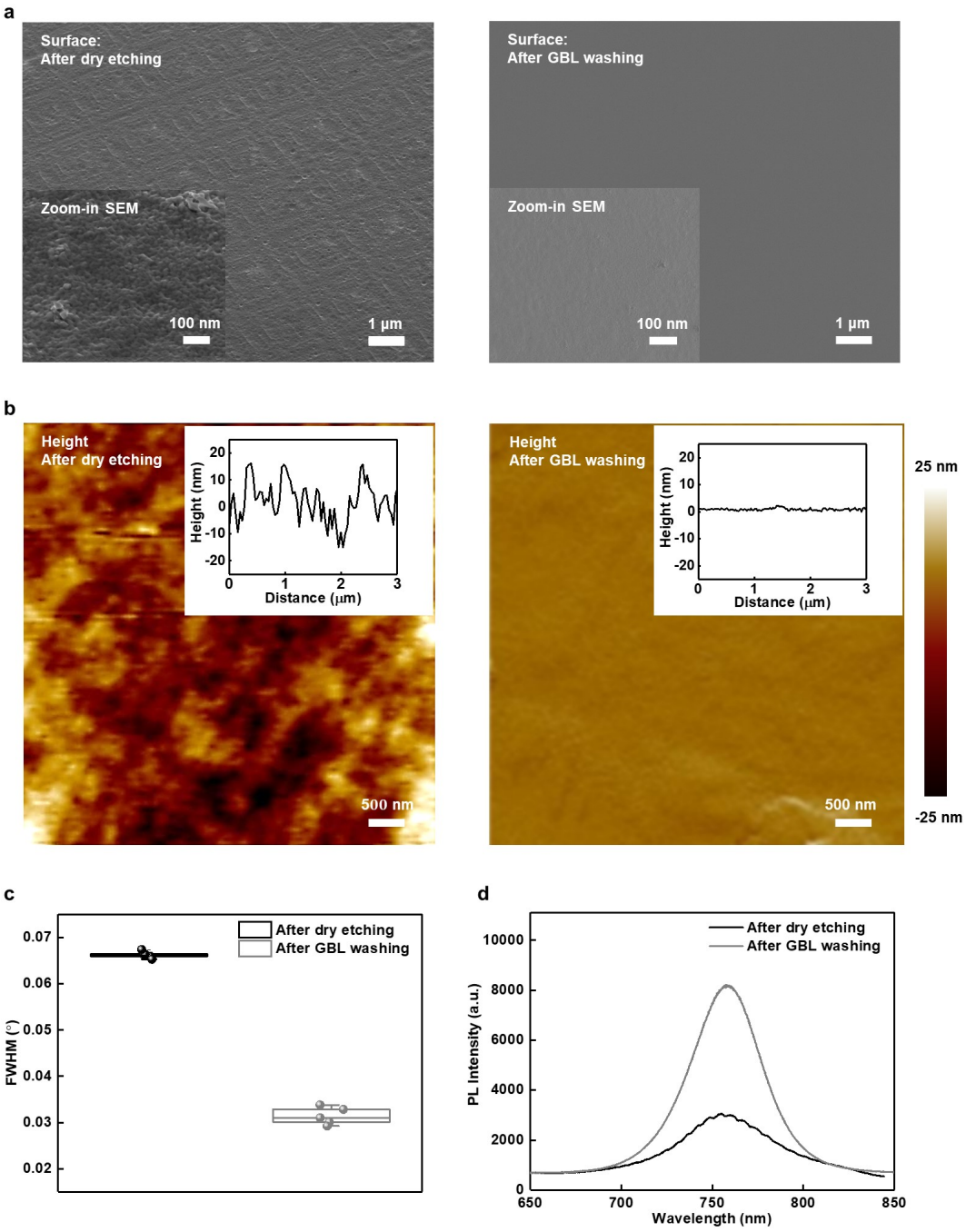

Supplementary Fig. 3 | Surface characterization of the crystals after etching and GBL washing. a, SEM images showing the crystal surface after dry etching and after GBL washing. The rough surface caused by dry etching can be fully removed by GBL washing. **b**, AFM measurement results of a transferred single-crystal $MAPbI_3$ surface before and after GBL washing. The rough surface caused by dry etching can be effectively smoothed by GBL washing. **c**, XRD ω scan measurements showing the huge difference before and after the washing, indicating that dry etching can cause serious damage to the crystal quality. **d,** PL measurements also reveal the same phenomenon, where the unwashed crystal shows a much weaker PL intensity and a broader peak.

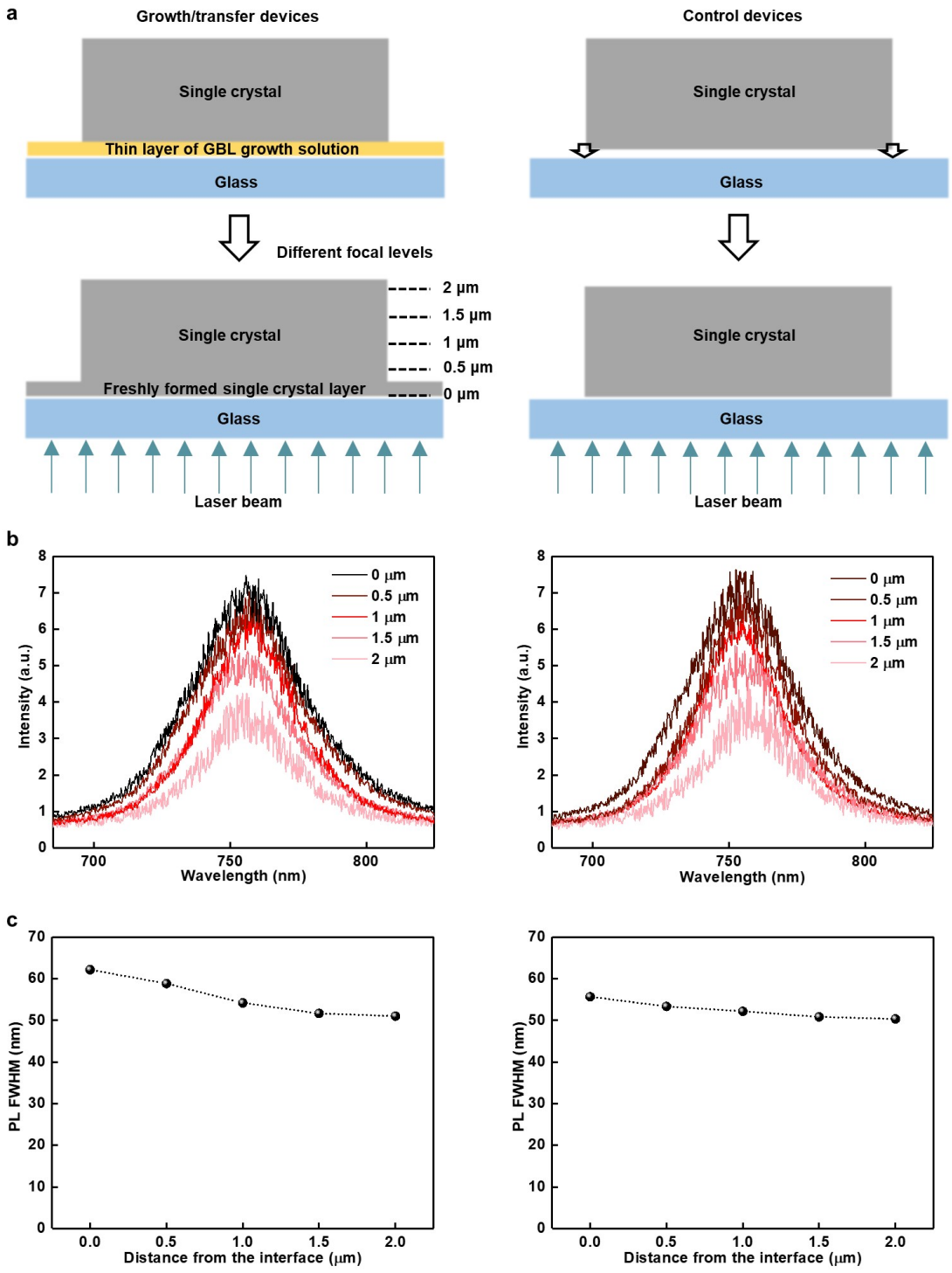

Supplementary Fig. 4 | Thickness-dependent PL measurements. a, Schematic setups of characterizing the growth/transfer and the control devices. **b**, The PL measurement results of the growth/transfer and control devices. **c**, The fitted FWHM results of both devices indicating that there is slight degradation of the crystallinity in the growth/transfer device because of the impurities and defects introduced during the re-growth process, which can potentially be improved by interfacial passivation.

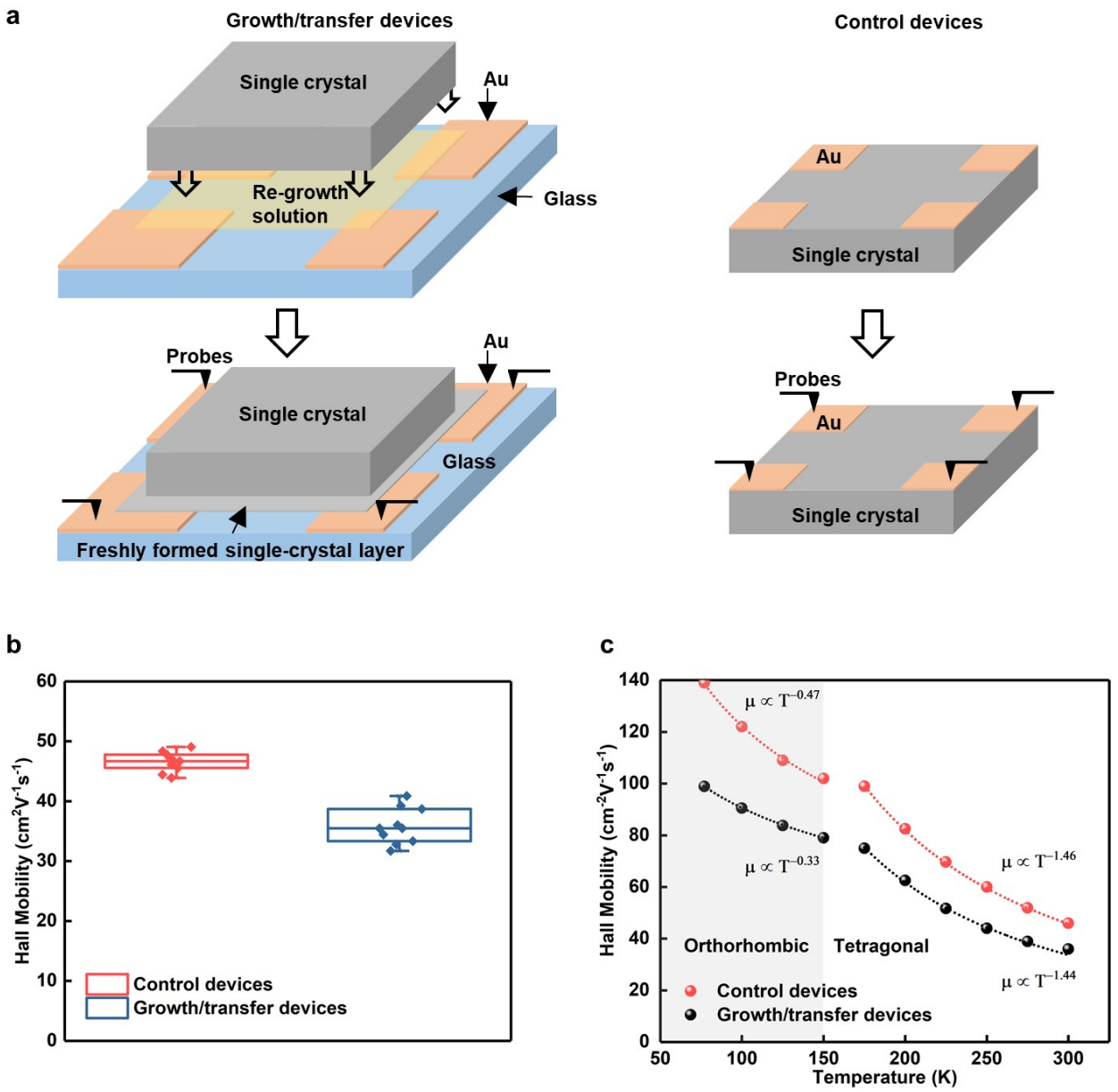

Supplementary Fig. 5 | Interfacial Hall mobility measurements. a, Schematic setups of the growth/transfer and control devices. **b**, Interfacial Hall mobility results showing that the growth/transfer devices have slightly lower mobilities and larger measurement variations compared with the control devices. **c**, Temperature-dependent interfacial Hall mobility measurement showing a noticeable difference in power exponents (~-0.33) for the growth/transfer devices compared with the control devices (~-0.47) under low temperatures, which can be attributed to the increased interfacial impurity scattering of the growth/transfer devices.

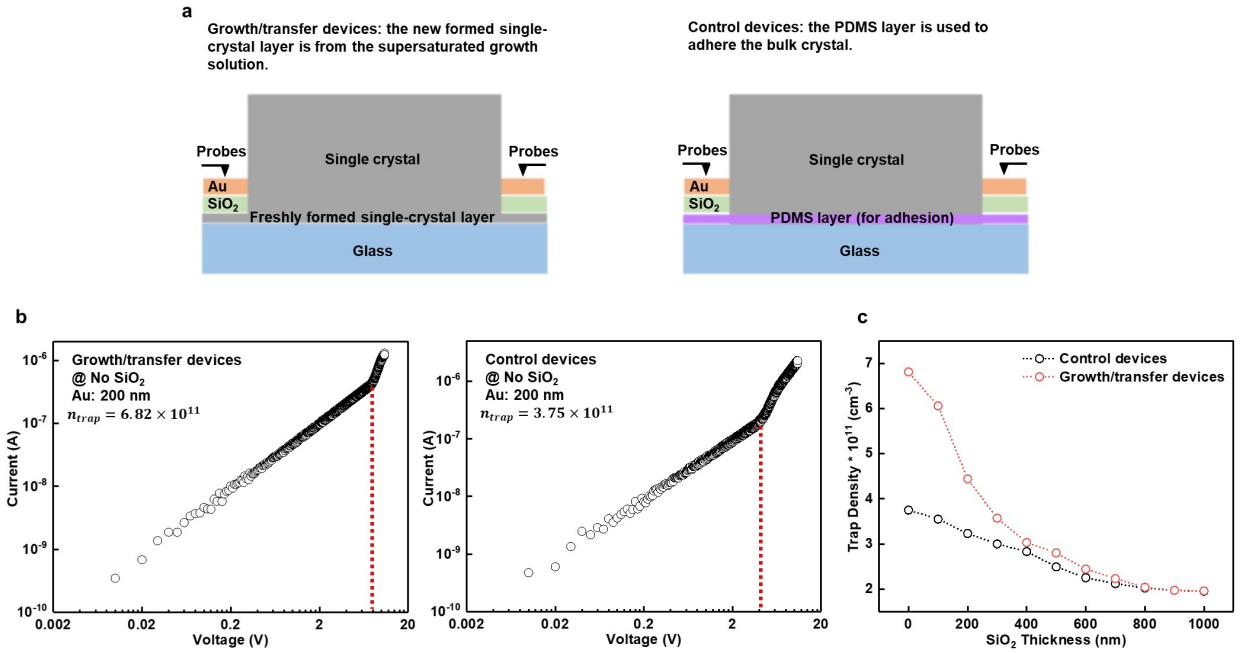

Supplementary Fig. 6 | Interfacial trap density measurements. a, Schematic setups. **b**, The calculated trap densities at the interfaces of the growth/transfer and control devices. **c**, Interfacial trap density results showing that the growth/transfer device has a higher trap density close to the interface than that distant from the interface.

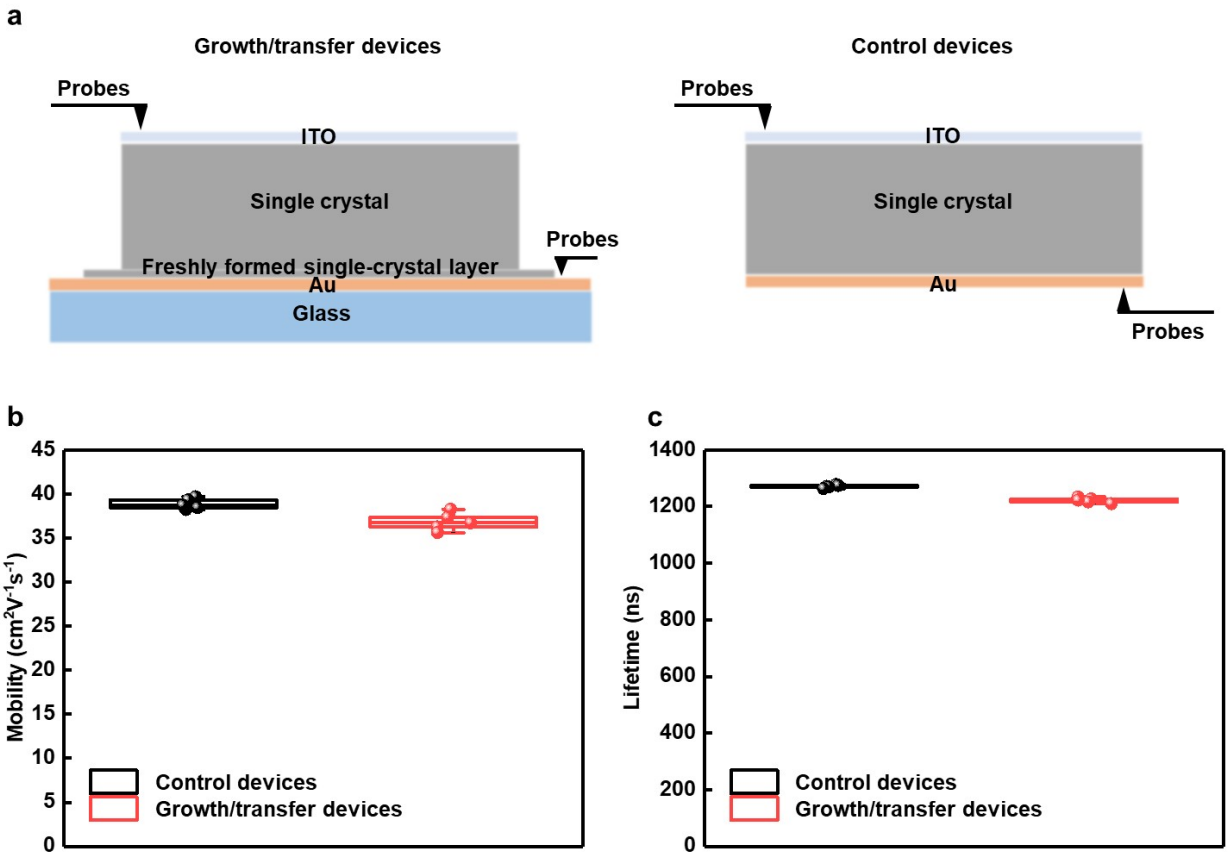

Supplementary Fig. 7 | TPC and TPV measurements. **a**, Schematic setups. **b**, TPC measurements showing that the growth/transfer devices have slightly lower mobilities compared with the control devices. **c,** TPV measurements showing that the growth/transfer devices have slightly shorter lifetimes compared with the control devices. Those results illustrate that the re-growth process can slightly decrease the electronic properties of the crystals (~4-5%).

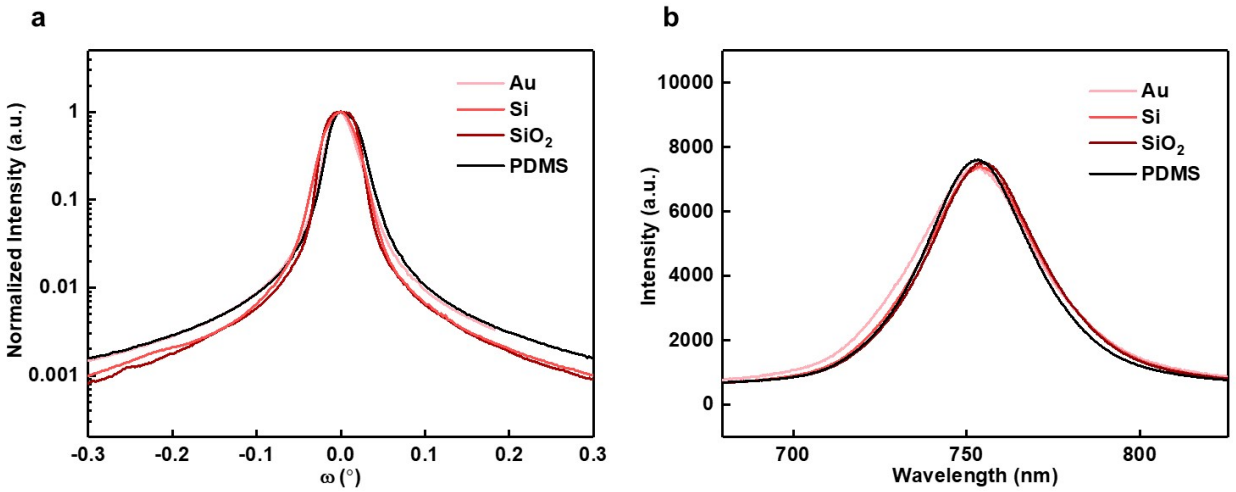

Supplementary Fig. 8 | Substrate-dependent interfacial crystal quality characterized by XRD and PL measurements. a, XRD ω scan with transferred single-crystal $MAPbI_3$ on different substrates. **b**, PL measurements with transferred single-crystal $MAPbI_3$ on different substrates. Both kinds of measurements do not show obvious difference among different substrates, indicating the crystal quality is substrate-independent.

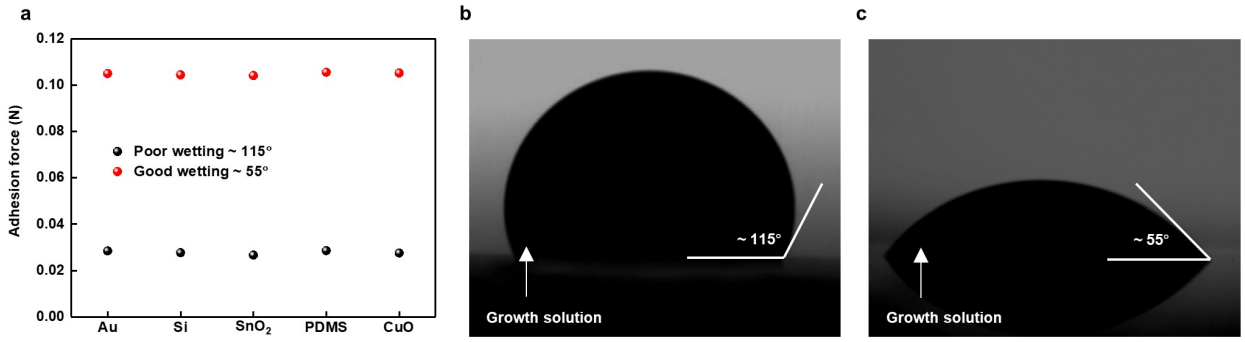

Supplementary Fig. 9 | Adhesion force and contact angle measurements. a, Measured adhesion force between the transferred single-crystal $MAPbI_3$ and different substrates with good and poor wetting conditions. Good wetting can always give a strong adhesion force regardless of the substrate. Contact angle measurements on an Au surface after being treated by UV-Ozone for **b**, 2 min and **c**, 10 min. By controlling the surface treatment, the wetting conditions and contact angles can be well controlled.

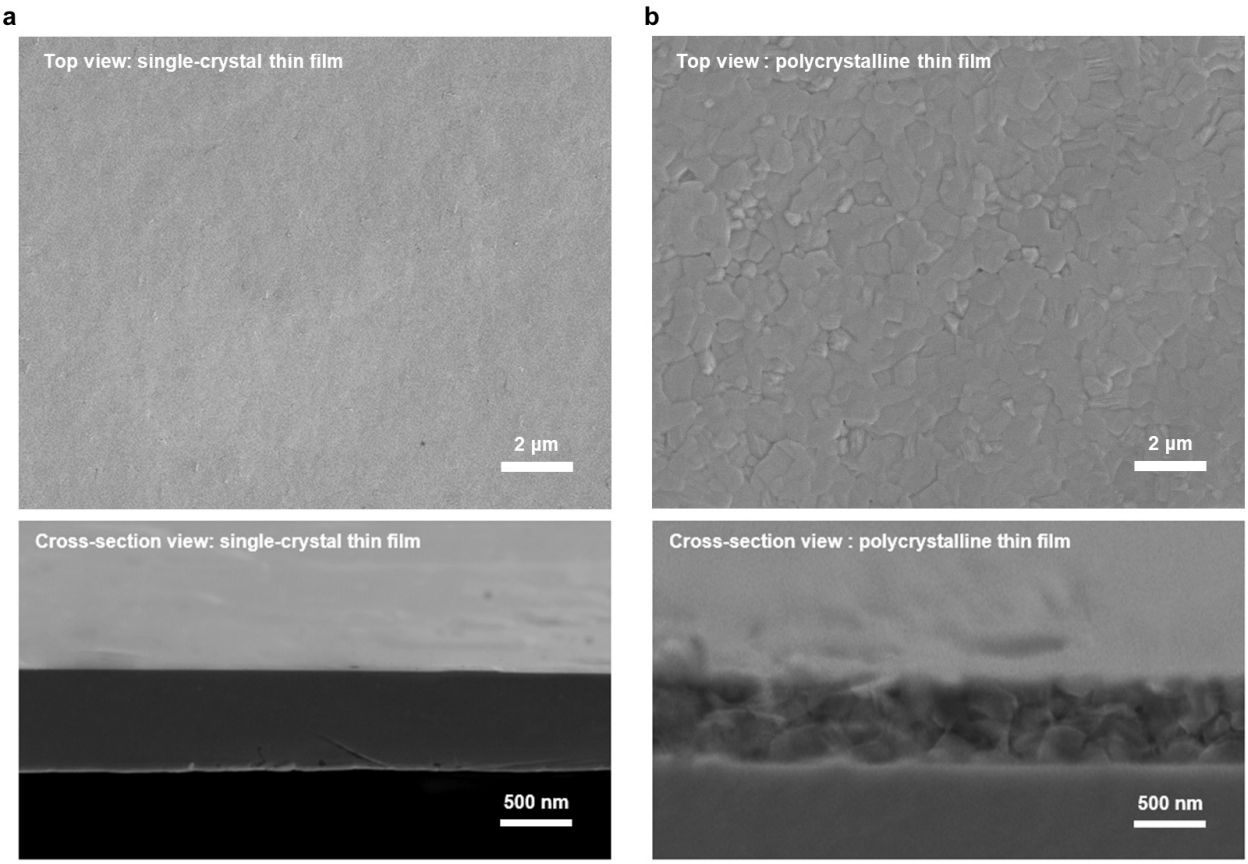

Supplementary Fig. 10 | Close-up views of the single-crystal and polycrystalline $MAPbI_3$. a, SEM images of the single-crystal $MAPbI_3$ thin film (top) from the top and (bottom) from the cross-section views, where no grain boundary can be seen, which is qualitatively different from the polycrystalline structure in **b**.

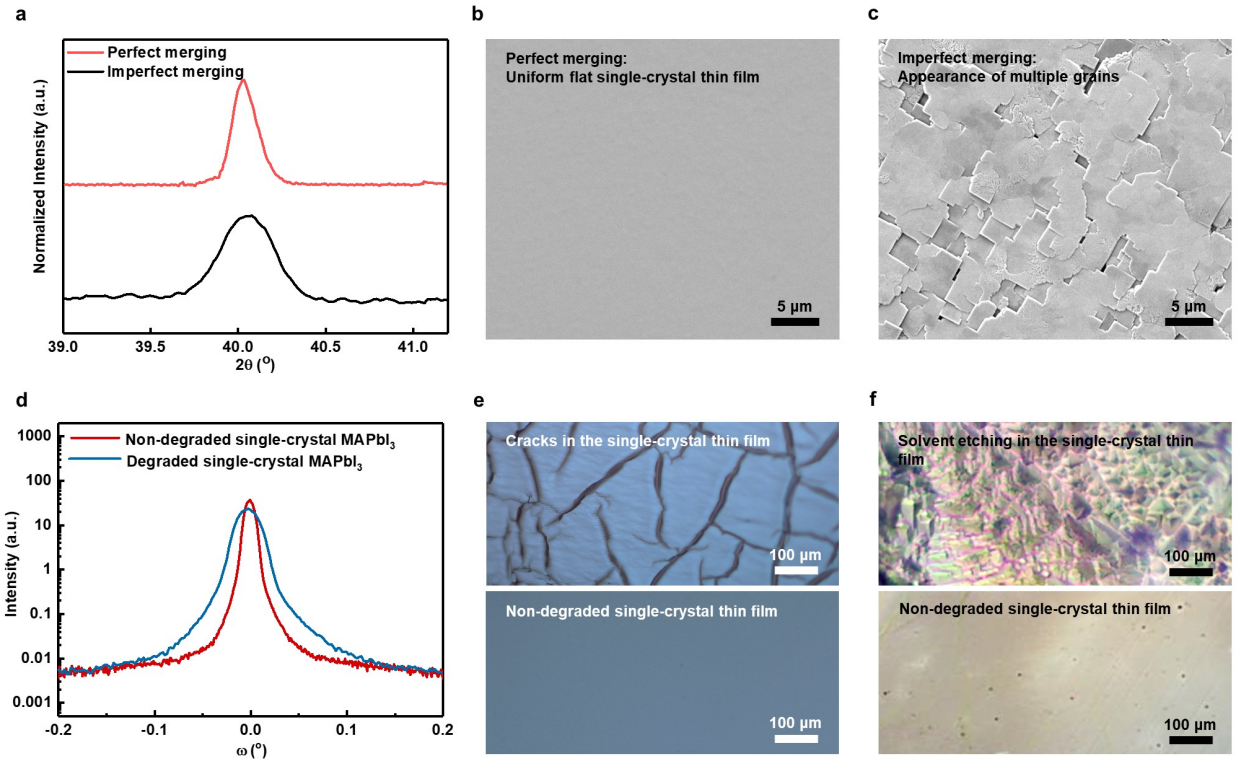

Supplementary Fig. 11 | Structural and morphological studies on the single-crystal thin film quality fabricated by the growth/transfer method. a, The (400) peaks in the XRD *θ-2θ* scan showing perfectly and imperfectly merged single-crystal thin films. The imperfect thin film shows a broad XRD peak due to the existence of small grains. SEM images show the top view of **b**, a perfect single-crystal thin film and **c**, an imperfect single-crystal thin film with multiple grains. **d**, XRD ω scans of a degraded and a non-degraded single-crystal $MAPbI_3$ thin films after the transfer and re-adhesion processes. The degraded single-crystal thin film exhibits a broad peak, which indicates a poor crystallinity. The degradations can come from either **e**, the improper lifting transfer process or **f**, improper use of the re-adhesion solvent.

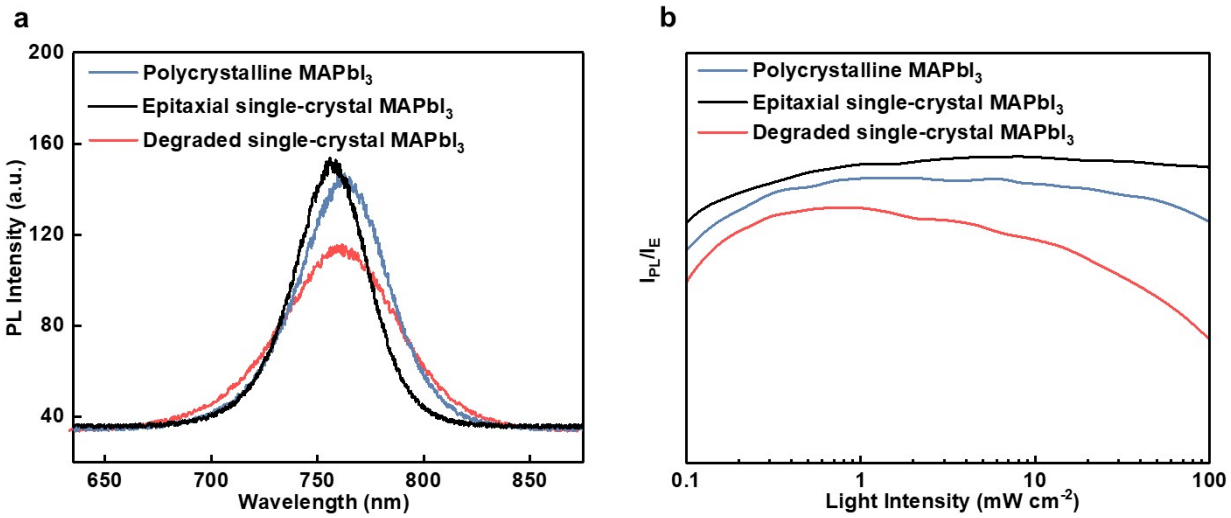

Supplementary Fig. 12 | PL studies on the quality of $MAPbI_3$ thin films. a, Three different types of $MAPbI_3$ thin films showing different PL measurement results. The polycrystalline thin film shows a little redshift compared with the single-crystal cases. The degraded single-crystal thin film shows a broad PL peak, which can be ascribed to a low crystal quality. **b**, I_{PL}/I_E comparisons showing that the polycrystalline and degraded single-crystal thin films exhibit a decreasing tendency with increasing light intensity, which provides additional evidence for their lower crystal qualities.

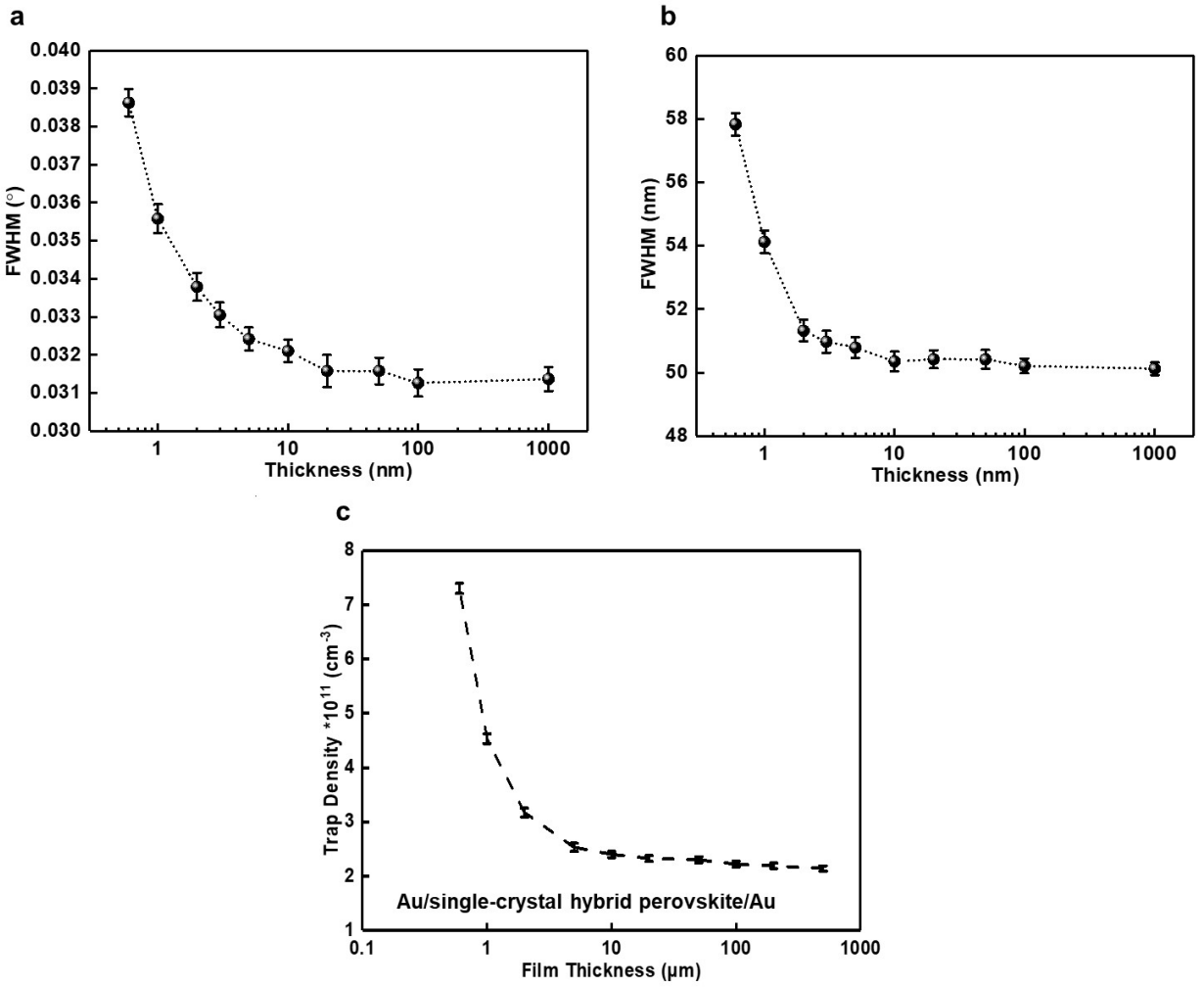

Supplementary Fig. 13 | Thickness dependent crystal qualities. a, XRD ω scan, **b**, PL measurements with different thicknesses of the crystals, and **c,** Trap density measurements. All measurements give the same trend that thicker crystals give better crystal qualities. Error bars come from three different measurements under the same scan condition.

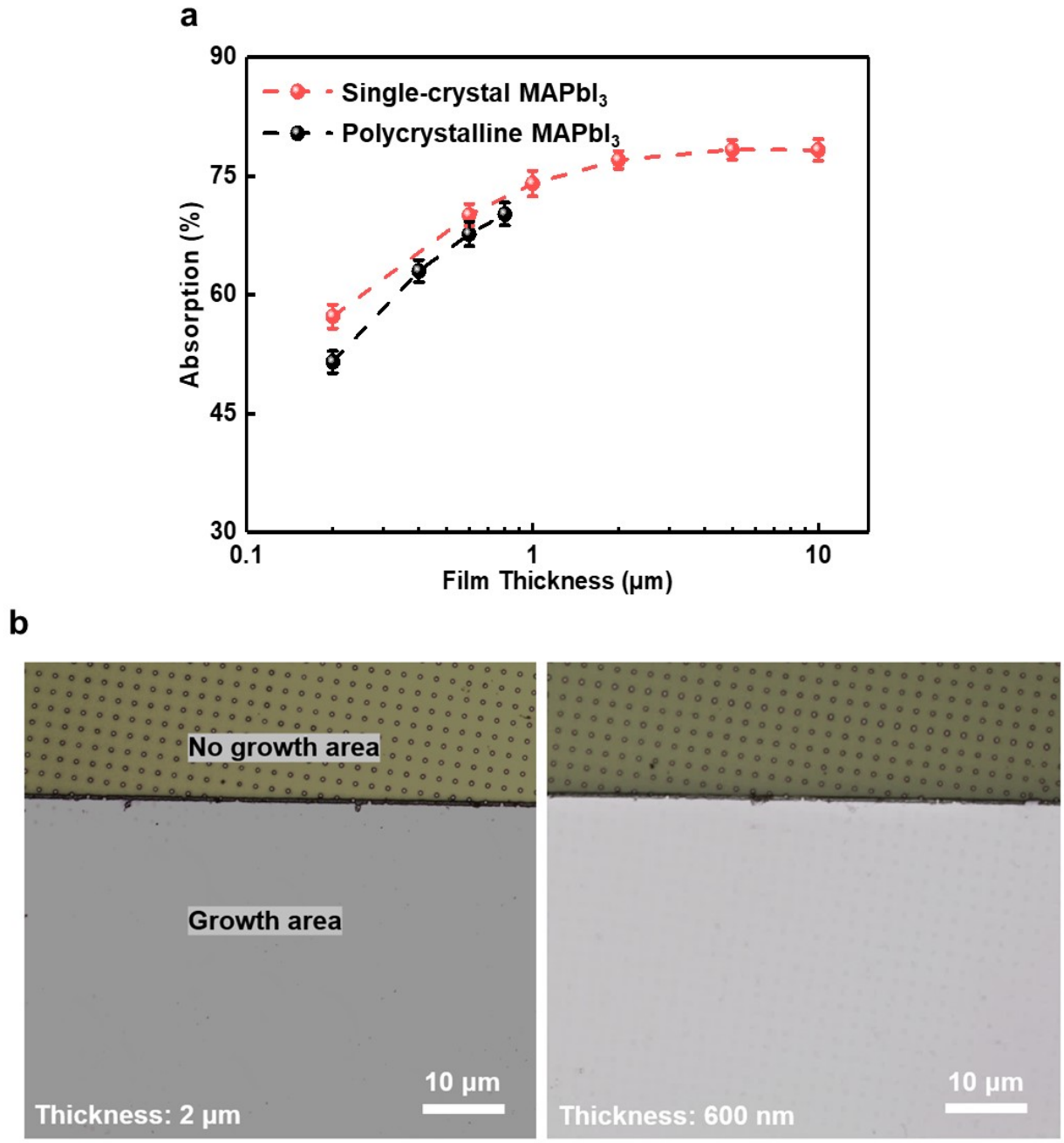

Supplementary Fig. 14 | Thickness dependent optical characterizations. a, UV-vis absorption measurements with different thicknesses for both single-crystal and polycrystalline $MAPbI_3$ thin films. **b**, Optical images showing a ~2 μm single-crystal film (left) and a ~600 nm single-crystal film (right) before transferring. The no growth area is achieved by applying a piece of tape to block growth on the patterned sites. The thickness comparison shows that a 600 nm thin film is insufficient to absorb all of the visible light.

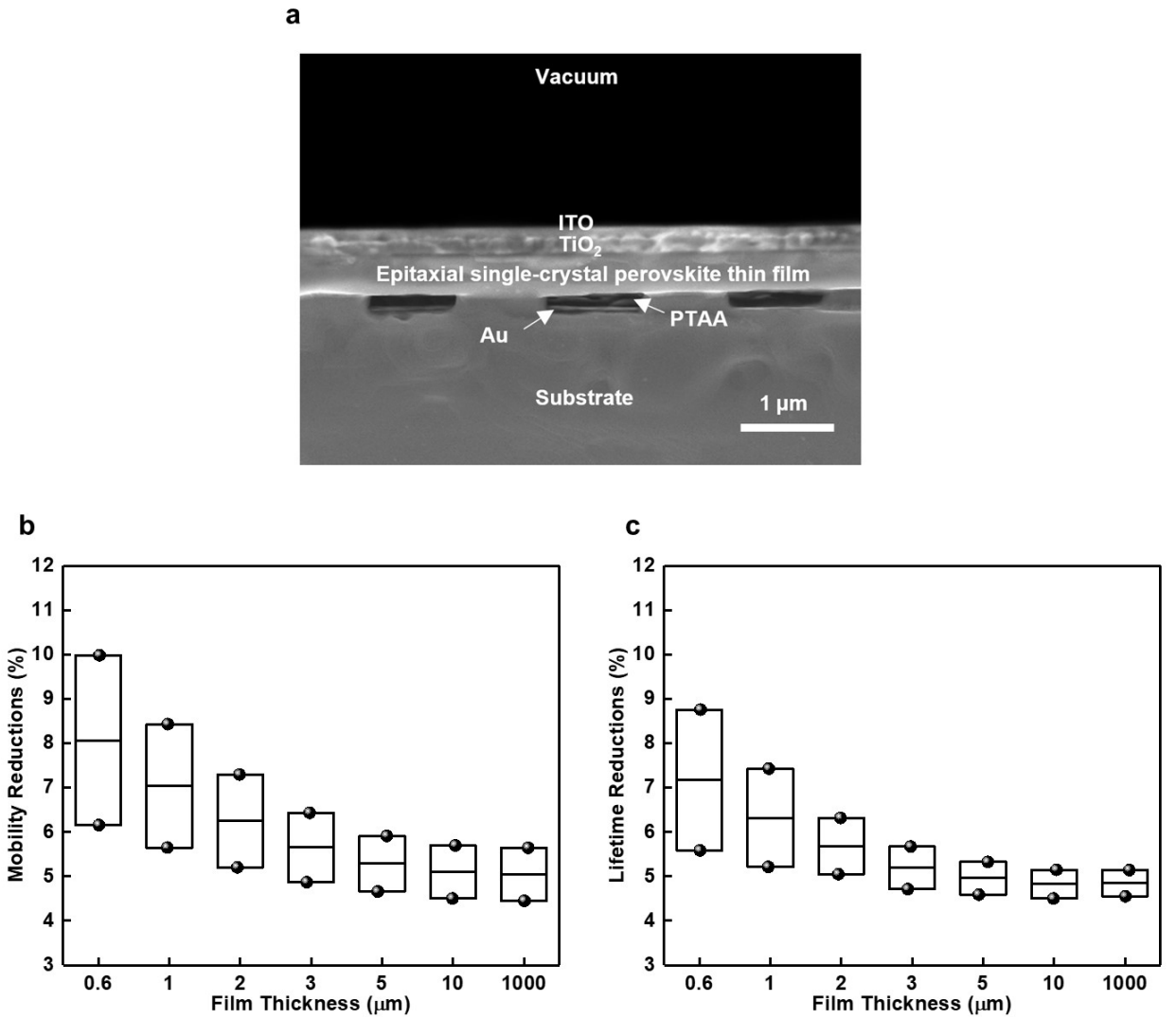

Supplementary Fig. 15 | The in situ fabricated devices and thickness-dependent carrier dynamics. a, The *in-situ* fabricated devices do not require additional peeling off the epitaxial single-crystal thin film. **b**, Mobility reductions in the $MAPbI_3$ single-crystal thin films with different thicknesses. Larger discrepancy exists in thinner films. **c**, Lifetime reductions in $MAPbI_3$ single-crystal thin films with different thicknesses. A similar tendency to the mobility reduction can be observed, indicating that the electrical measurements in thinner films are more easily to be influenced by solution treatments.

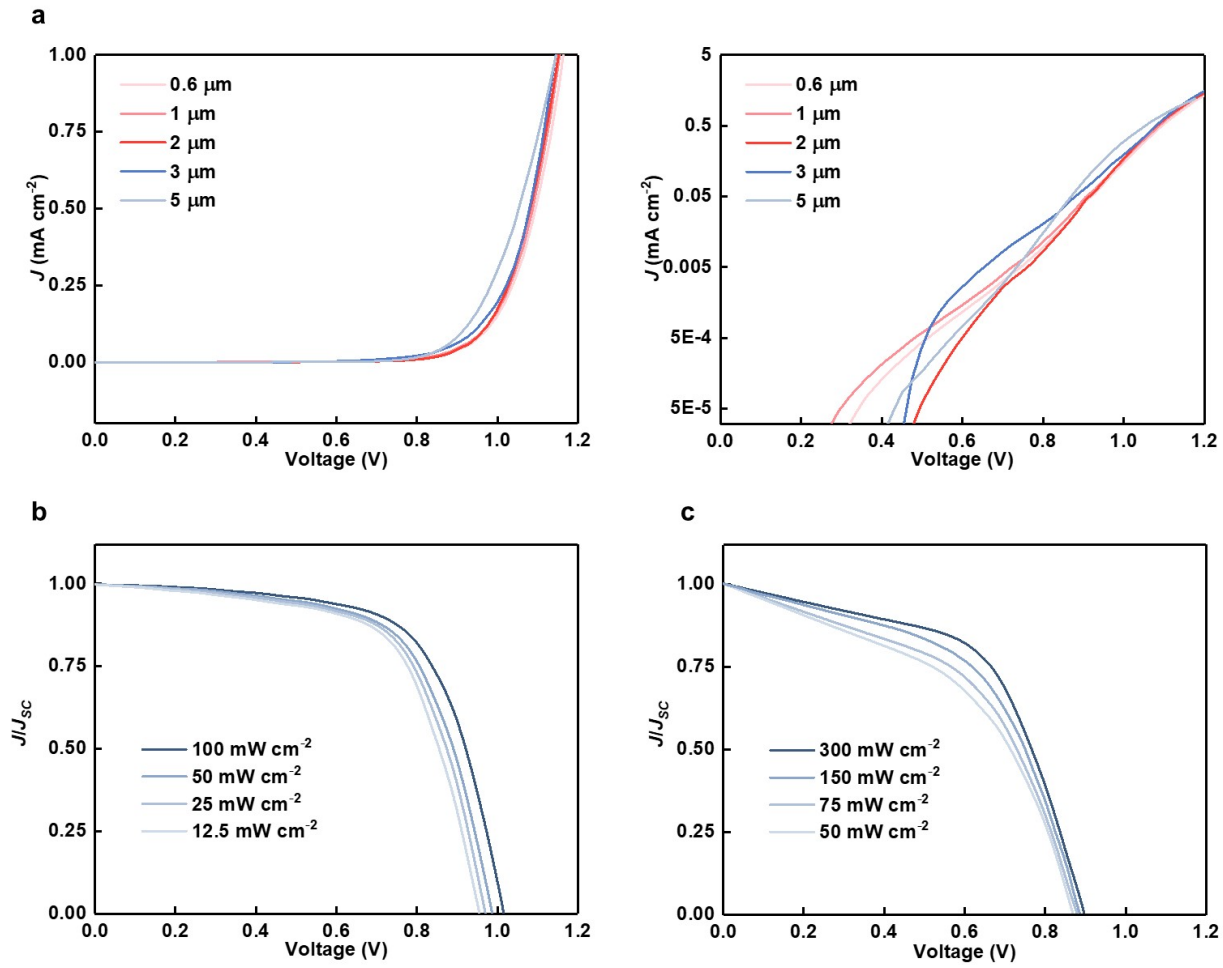

Supplementary Fig. 16 | Dark and light J-V curve measurements. a, Linear scale (left) and logarithm scale (right) dark *J-V* curves measured with different single-crystal perovskite thicknesses. The dark current is several orders of magnitude lower than the photocurrent in Figure 2b. **b**, Light *J-V* curves measured on a 600 nm thick single-crystal thin film with different light intensities. Even under the lowest 12.5 mW cm^{-2} intensity, the dark injection near the open circuit voltage condition is still insignificant, which means the shunt resistance is negligible even in the thinnest film. **c**, Light *J-V* curves measured on a 5 μm thick single-crystal thin film with different light intensities. The FF does not change significantly with an increasing light intensity, which means the series resistance does not contribute much to the *J-V* measurement results.

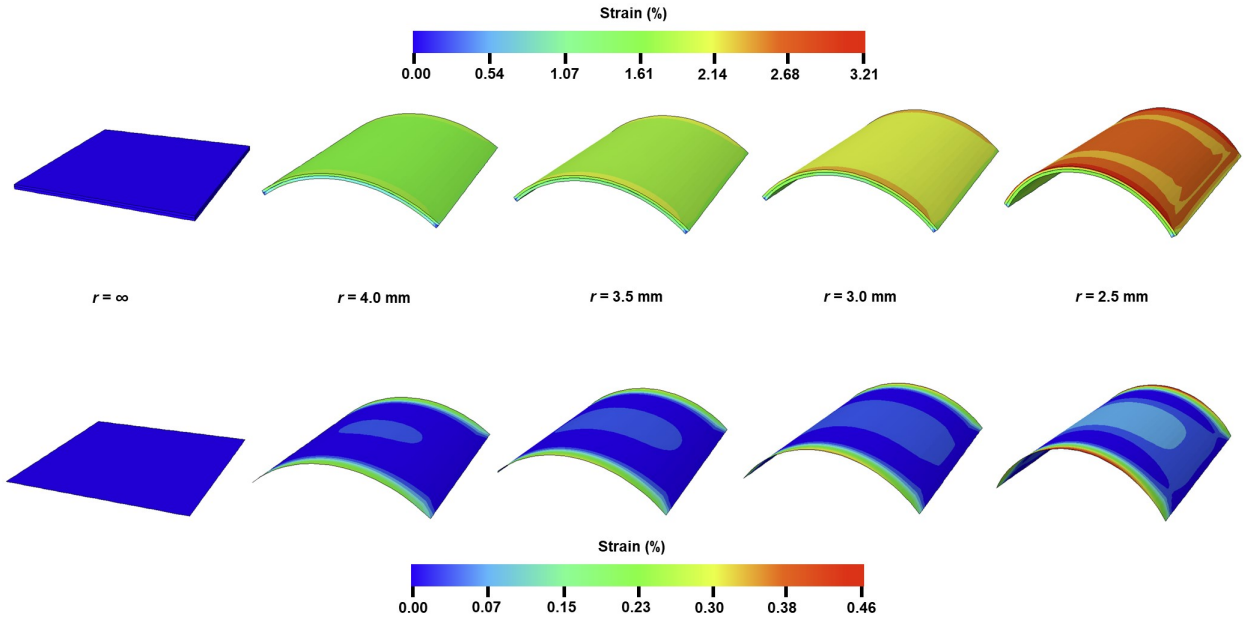

Supplementary Fig. 17 | Simulation of strain distribution in a flexible single-crystal perovskite device. Finite element analysis simulations are shown under different bending radii. The results in the top panels correspond to the entire sandwich structure, i.e., PET/single-crystal $MAPbI_3$/SU8-PDMS. The results in the bottom panels correspond to the extracted perovskite layer only (with the other layers hidden). At a bending radius of 2.5 mm, most parts of the perovskite layer have a principal strain of less than 0.25%. The edge areas show a principal strain of around 0.36%, which is close to the failure strain of this material.

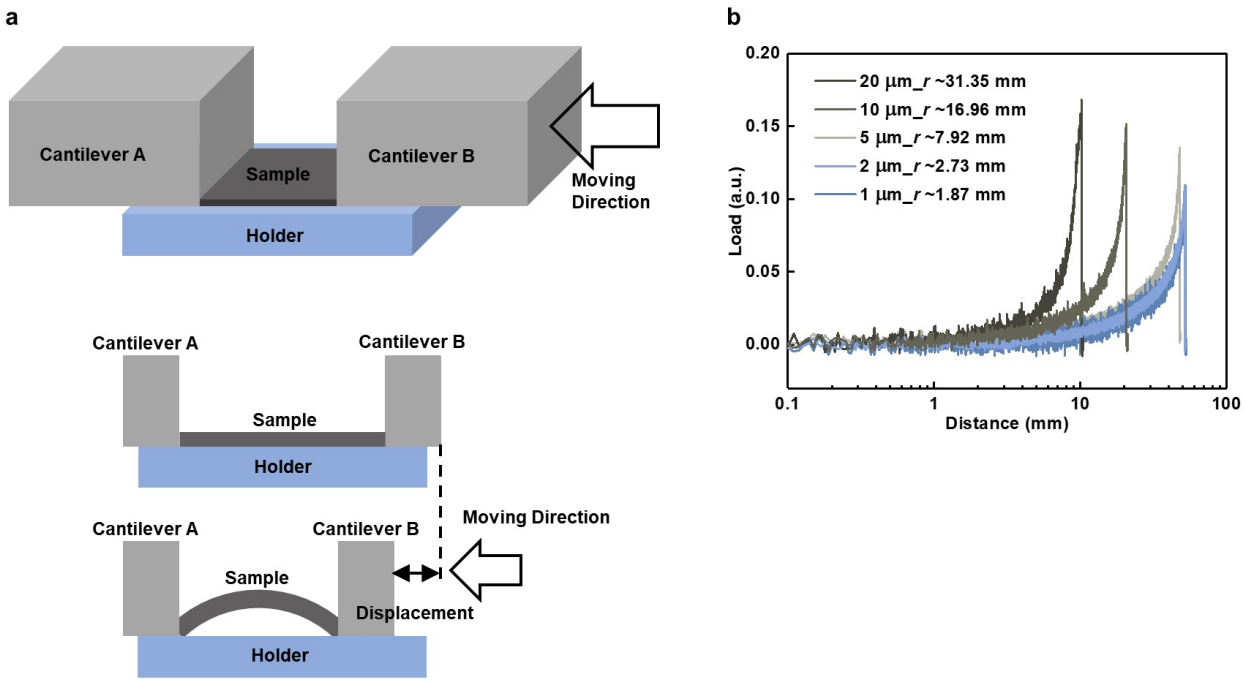

Supplementary Fig. 18 | Flexibility tests of the NMP design. a, Schematics of the measurement setup. A 5 cm by 5 cm sample is used to do the test, where the single-crystal perovskite crystal is at the NMP of the sample. The displacement is used to calculate the bending radius. **b**, Testing results showing remarkable flexibility of such brittle single-crystal perovskites. The thinner the perovskite crystal is, the smaller it can be bent.

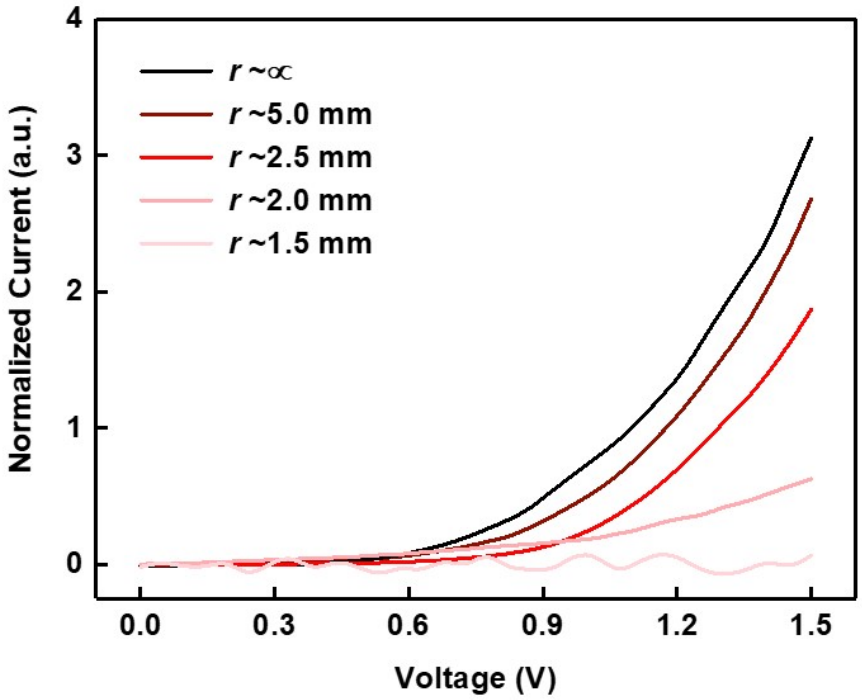

Supplementary Fig. 19 | IV measurements of the flexible single-crystal $MAPbI_3$ under different bending radii. The results show a significant reduction in the current when the device is bent at $r \sim 2$ mm.

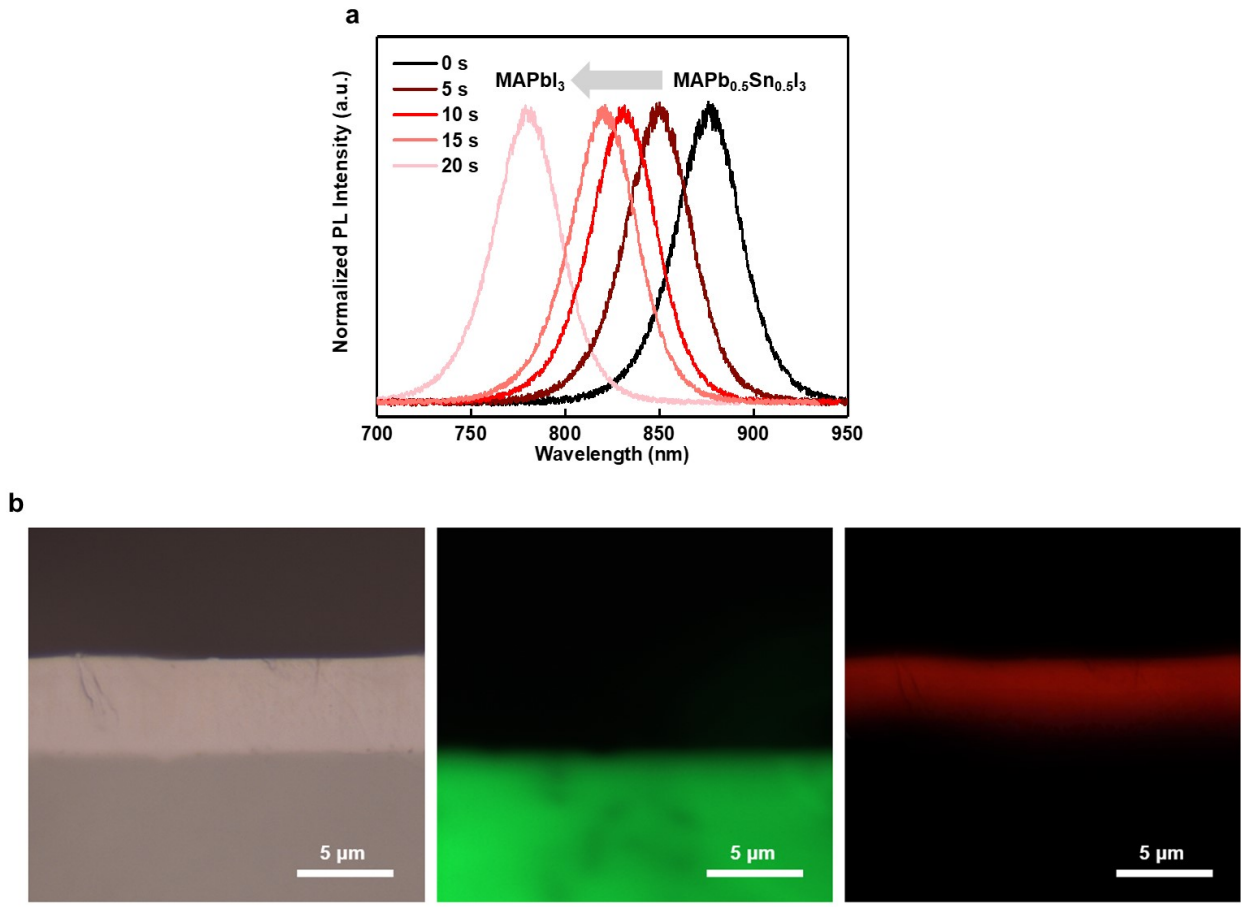

Supplementary Fig. 20 | PL measurements of graded single-crystal $MAPb_{0.5+x}Sn_{0.5-x}I_3$. a, PL measurements of graded single-crystal $MAPb_{0.5+x}Sn_{0.5-x}I_3$ at different growth time-stages. All samples are measured only at the top surface. A blue shift of the PL as time increases corresponds to an increased bandgap from the $MAPb_{0.5}Sn_{0.5}I_3$ side to the $MAPbI_3$ side. **b**, An optical image (left) shows the epitaxially grown graded single-crystal $MAPb_{0.5+x}Sn_{0.5-x}I_3$ on top of the single-crystal $MAPbBr_3$ substrate. The middle fluorescent image is from $MAPbBr_3$ while the right fluorescent image is from Pb rich part in the graded single-crystal $MAPb_{0.5+x}Sn_{0.5-x}I_3$.

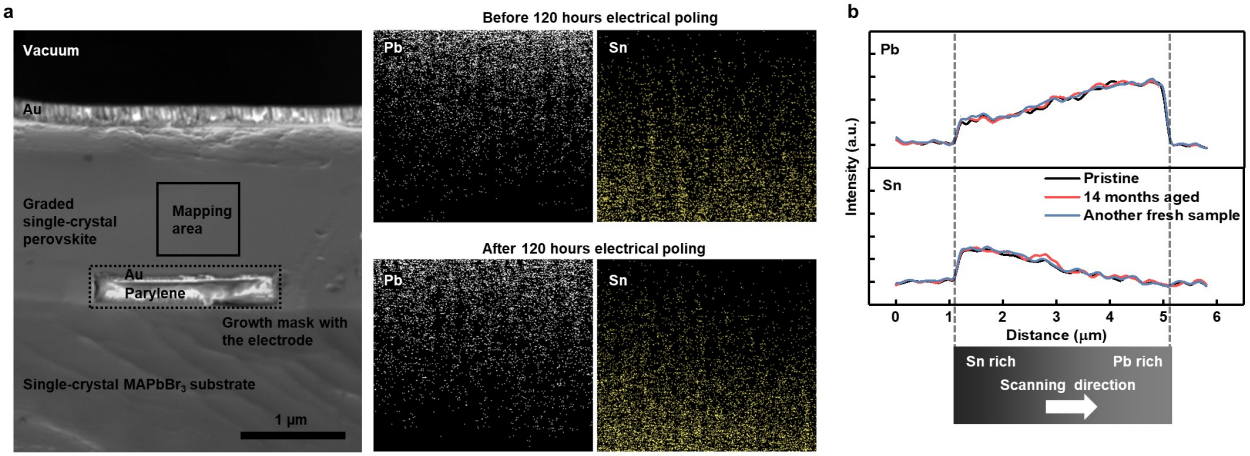

Supplementary Fig. 21 | Cross-sectional linear energy-dispersive x-ray spectroscopy (EDX) measurements. a, EDX mapping of the graded single-crystal $MAPb_{x+0.5}Sn_{x-0.5}I_3$. The patterned parylene/Au serves as the bottom electrode while the top Au electrode is evaporated by e-beam evaporation. The sample is kept in a dark dry box while a 1.2 V DC bias is applied. No noticeable Sn/Pb ion migration happens after 120 hours of electrical poling. **b,** EDX linear scans with gradient intensities of Sn and Pb along the scan direction, which confirms the gradually alloyed structure. A repeated measurement, after 14 months storage in the vacuum box, reveals the stability of the single-crystal $MAPb_{x+0.5}Sn_{x-0.5}I_3$.

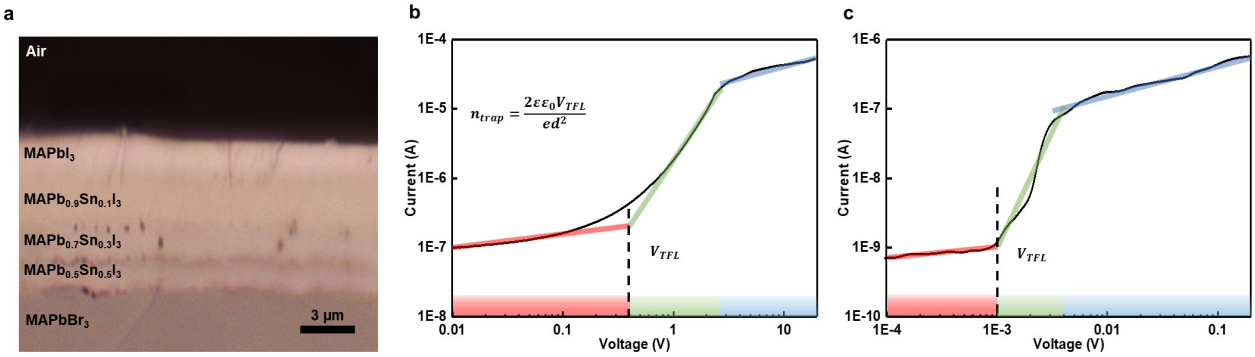

Supplementary Fig. 22 | A single-crystal perovskite structure with distinct heterojunctions. **a,** An optical image showing the multilayered single-crystal perovskite with clear heterojunction interfaces between adjacent layers. *I-V* measurements of the trap densities in **b**, a double-layered single-crystal $MAPbI_3$-$MAPb_{0.5}Sn_{0.5}I_3$ and **c**, a graded $MAPb_{0.5+x}Sn_{0.5-x}I_3$ structure. The heterojunction double-layer shows a higher trap density $n_{trap} = 1.77\times10^{14}\ cm^{-3}$ than $n_{trap} = 3.34\times10^{12}\ cm^{-3}$ of the graded structure. The single-crystal perovskite thickness is ~10 μm for both cases.

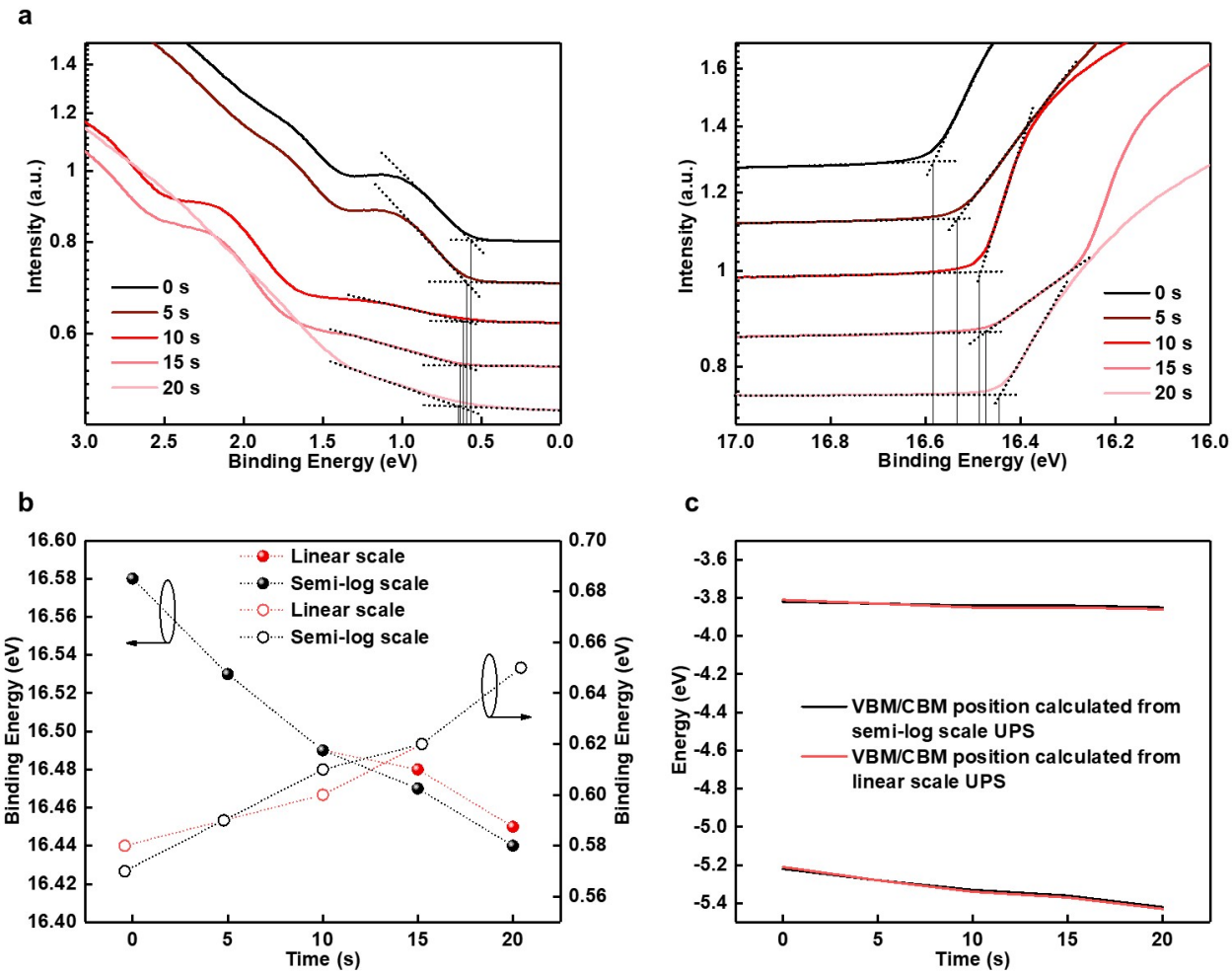

Supplementary Fig. 23 | UPS measurements of the graded epitaxial single-crystal $MAPb_{0.5+x}Sn_{0.5-x}I_3$. **a**, Semi-log plots are used to identify the VBM position from the low binding energy cutoff (left) and the high binding energy cutoff (right). **b**, Comparing binding energies from the linear scale plots and the semi-log scale plots, the difference is considered to be negligible in this case. **c**, Summarized band diagrams calculated from the UPS data in both linear scale and semi-log scale. No obvious difference can be found.

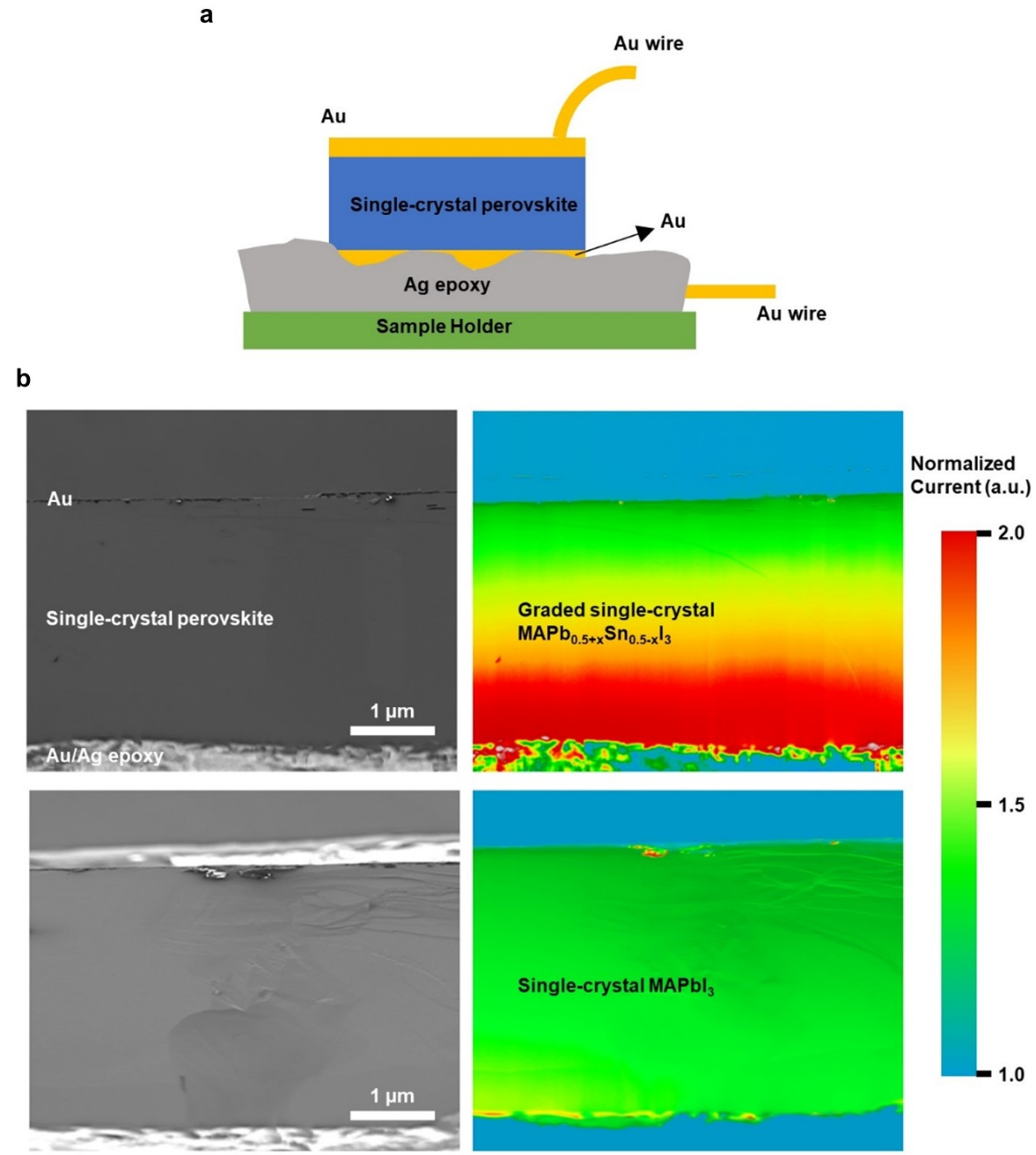

Supplementary Fig. 24 | EBIC mapping with symmetric electrodes. a, The schematic measurement setup. Same Au electrodes are used on both sides. **b**, The graded current output can only be observed in the graded single-crystal perovskite, which excludes the possible influence from the electrodes to the EBIC measurements.

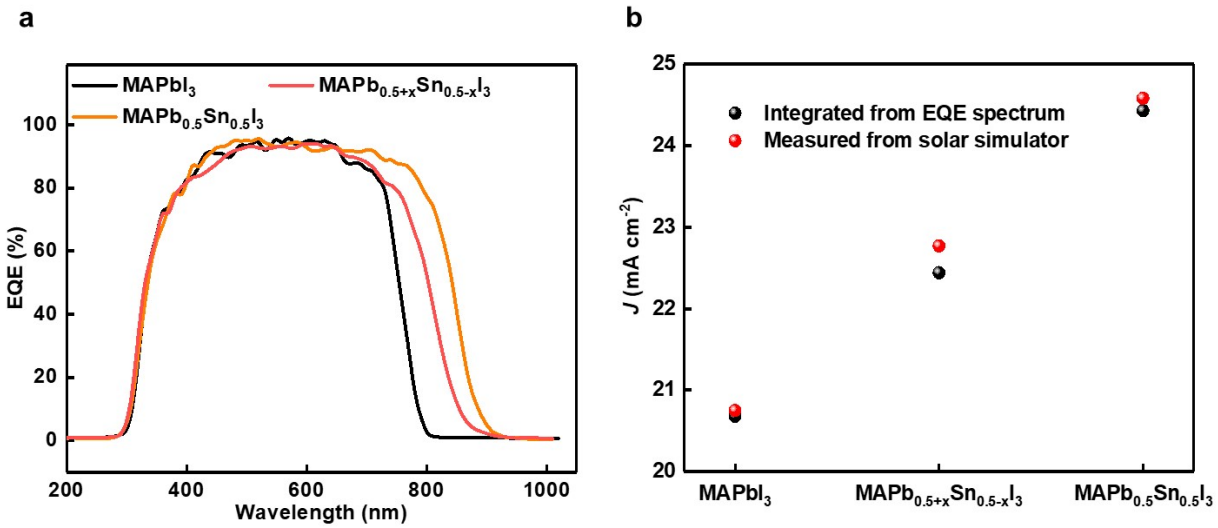

Supplementary Fig. 25 | EQE measurements with different absorbers. a, Bandgap-graded single-crystal $MAPb_{0.5+x}Sn_{0.5-x}I_3$ photovoltaic devices show a median averaged current density (integrated EQE) compared with single-crystal $MAPbI_3$ and compositionally uniform single-crystal $MAPb_{0.5}Sn_{0.5}I_3$. More Sn content leads to a lower bandgap and exciton dissociation energy, and thus a higher EQE. **b**, Current density from integrated EQE measurements, which matches the *J-V* results and confirms the higher current density is due to the Sn doping.

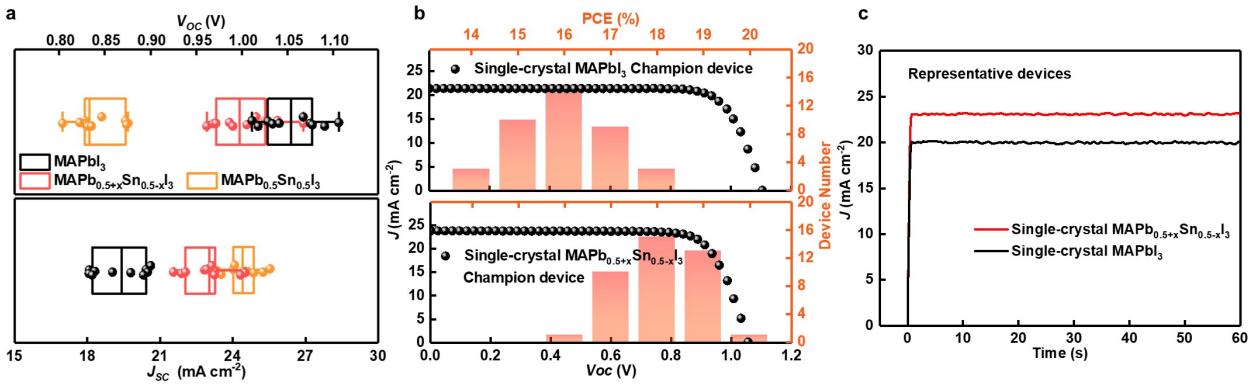

Supplementary Fig. 26 | The statistical device performance distributions. a, Bandgap-graded $MAPb_{0.5+x}Sn_{0.5-x}I_3$ showing a higher J_{SC} than $MAPbI_3$ and relatively maintained V_{OC}. **b**, PCE distributions for single-crystal $MAPbI_3$ (top) and graded single-crystal $MAPb_{0.5+x}Sn_{0.5-x}I_3$ (bottom) photovoltaic devices. The graded single-crystal photovoltaics show overall better performance (with the highest PCE ~ 20.04%) than the compositionally uniform single-crystal photovoltaics. **c**, Measured photocurrent at maximum power points for representative devices as a function of time.

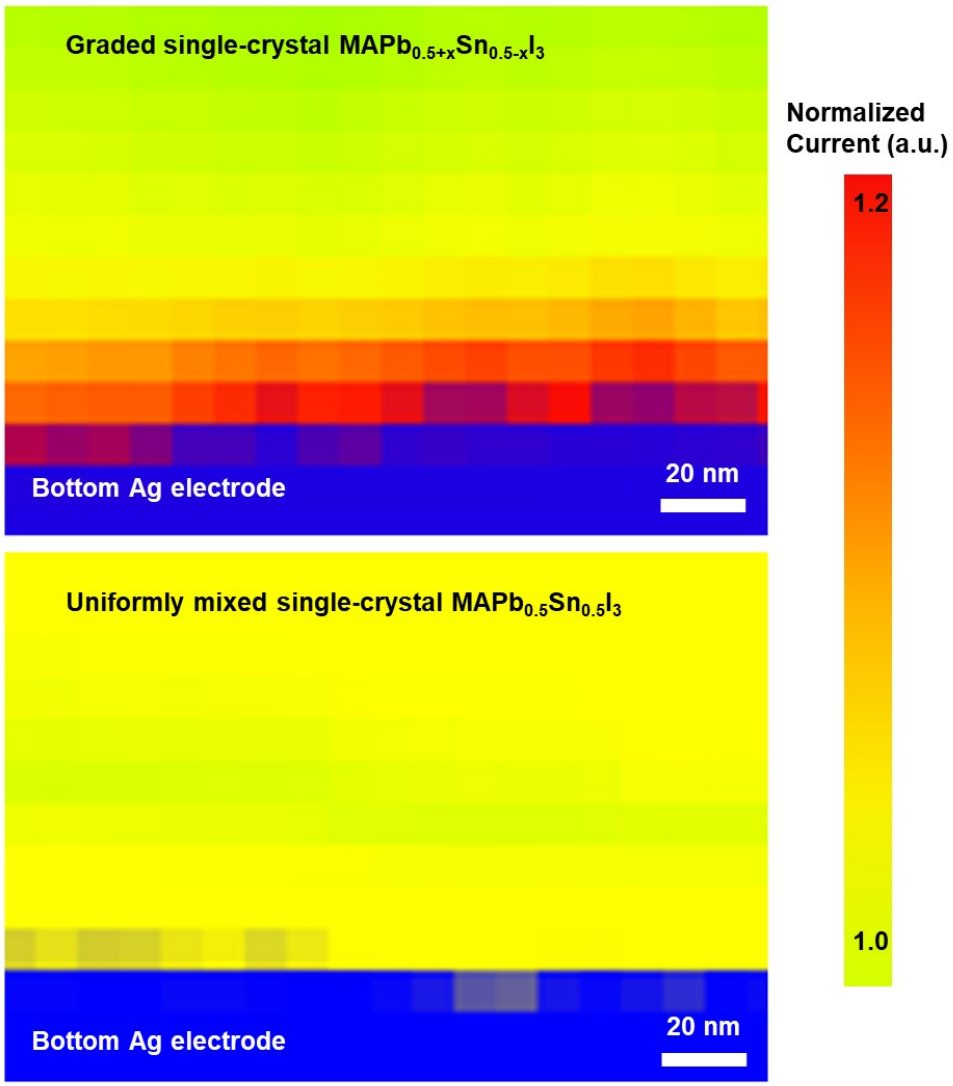

Supplementary Fig. 27 | Close-up EBIC mapping results at the interface. In the graded single-crystal $MAPb_{0.5+x}Sn_{0.5-x}I_3$, the interfacial region with the bottom electrode shows stronger current signals than regions away from the interface, which is because of the gradually mixed Pb and increased bandgap. The compositionally uniform single-crystal $MAPb_{0.5}Sn_{0.5}I_3$ shows uniform current signals. However, the interfacial region in the graded single-crystal $MAPb_{0.5+x}Sn_{0.5-x}I_3$ (where the composition is $MAPb_{0.5}Sn_{0.5}I_3$ at the interfacial region) always gives even stronger signals than the compositionally uniform single-crystal $MAPb_{0.5}Sn_{0.5}I_3$. The stronger signals are likely due to the easier exciton separation and carrier collection facilitated by the graded bandgap in the $MAPb_{0.5}Sn_{0.5}I_3$.

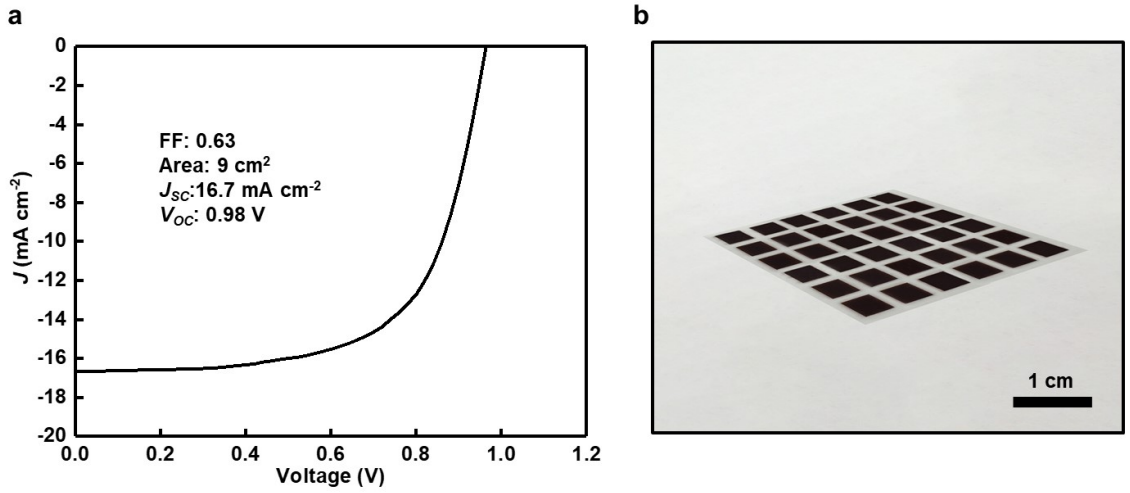

Supplementary Fig. 28 | Large-scale flexible single-crystal perovskite photovoltaics. a, The *J-V* measurement of the best large-scale flexible single-crystal perovskite photovoltaic device, which results in a PCE ~10.3% with a working area of around 9 cm^2. **b**, An optical image showing the island-bridge structure before depositing Spiro-MeOTAD and Au. Each black single-crystal perovskite is around 5 mm by 5 mm.

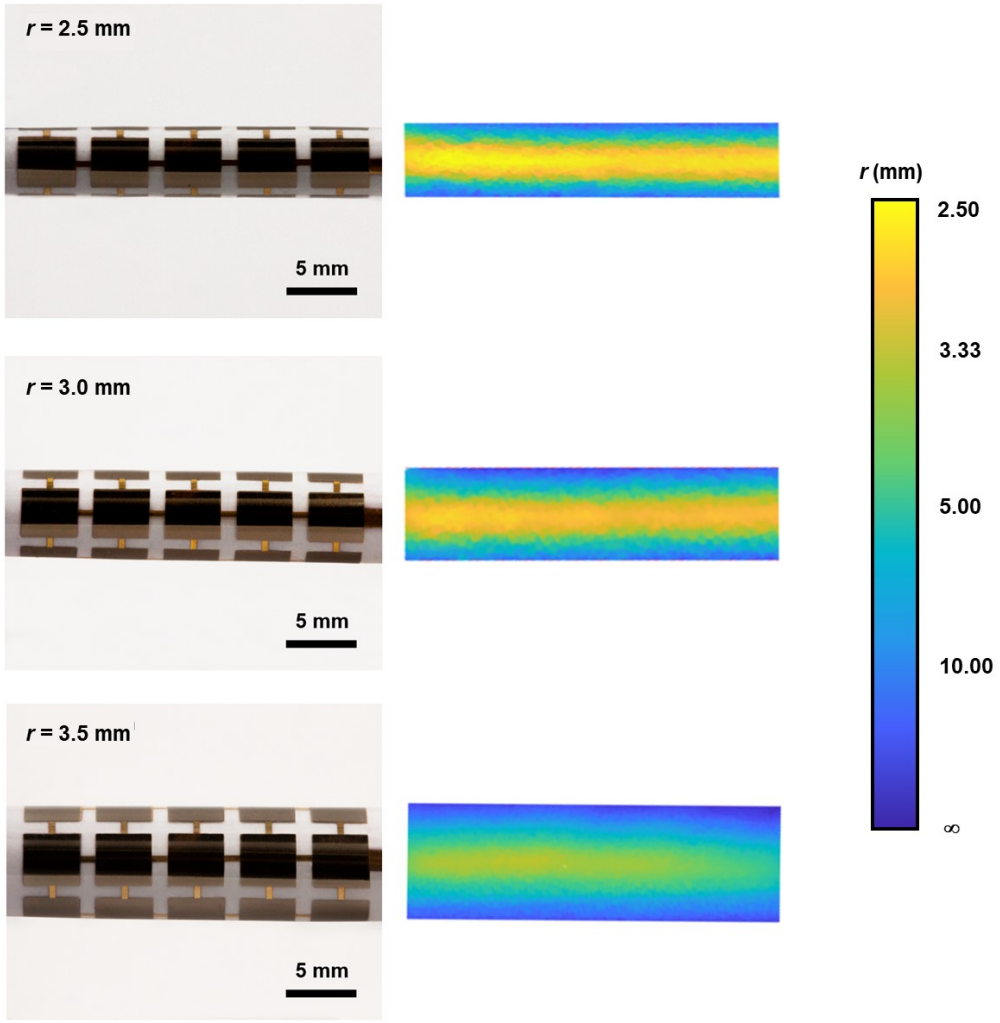

Supplementary Fig. 29 | Bending radius distribution mapping. The results show that the minimum bending radius occurs at the middle line of the device. Most parts of the device will not experience such extreme bending conditions.

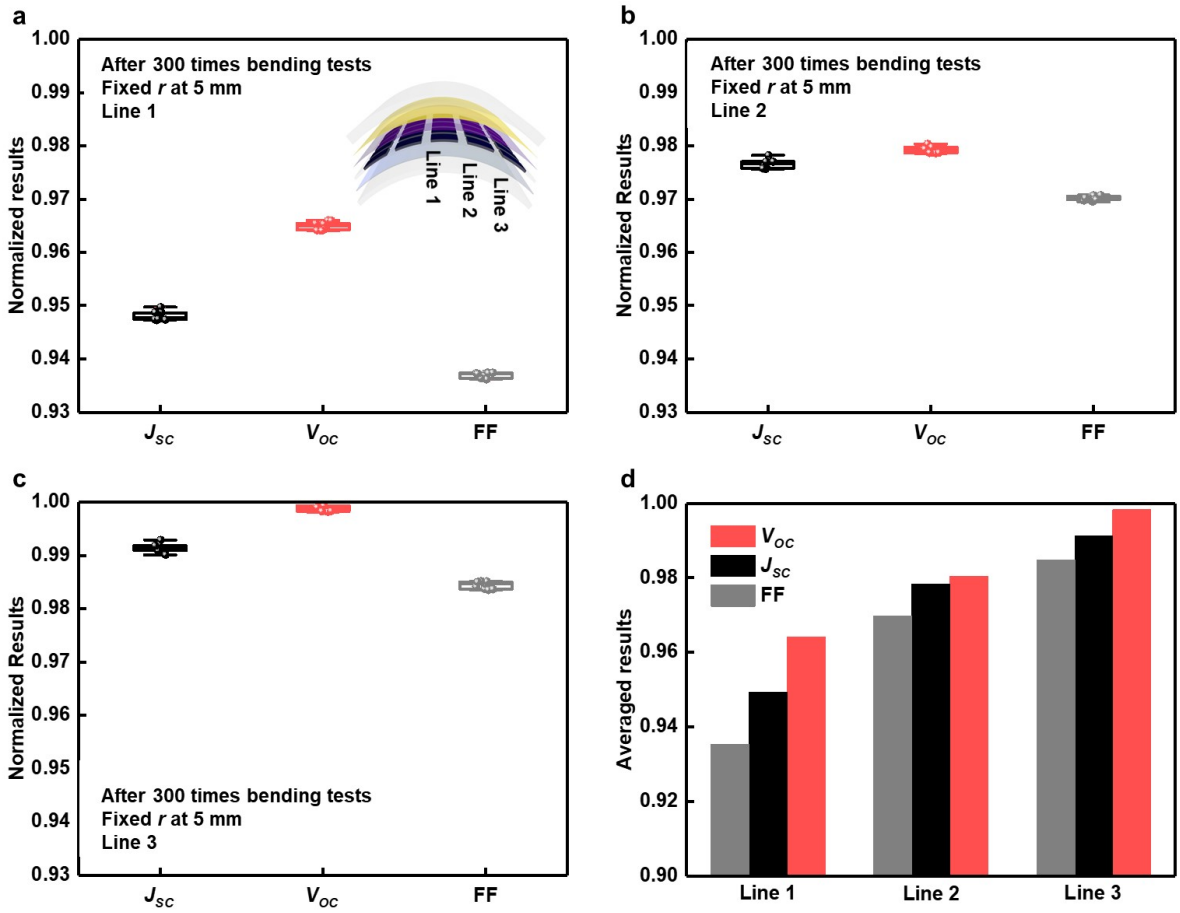

Supplementary Fig. 30 | Cyclic bending tests. The results for different pixels in line 1, line 2, and line 3 after cycling for 300 times are shown in **a**, **b**, and **c**, respectively. The inset schematics in **a** show the non-uniform bending conditions for different pixels. Line 1, line 2, and line 3 undergo different bending radii during the cycling. **d**, The comparison of V_{OC}, J_{SC}, and FF among different lines showing the impact of different bending curvatures on the device performance.

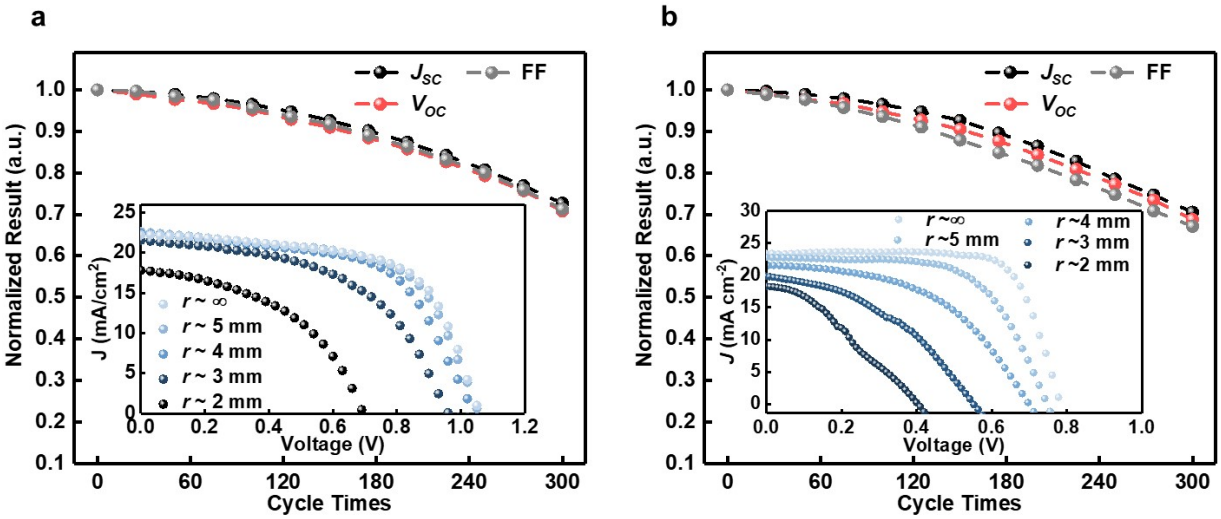

Supplementary Fig. 31 | Cyclic flexibility tests of polycrystalline structures. The test results are for **a**, polycrystalline $MAPbI_3$ and **b**, polycrystalline $MAPb_{0.5}Sn_{0.5}I_3$. The insets show *J-V* curves with different bending radii. All of these results demonstrate obvious degradation of the device performance, likely due to the grain boundary facilitated ion/molecule migration.

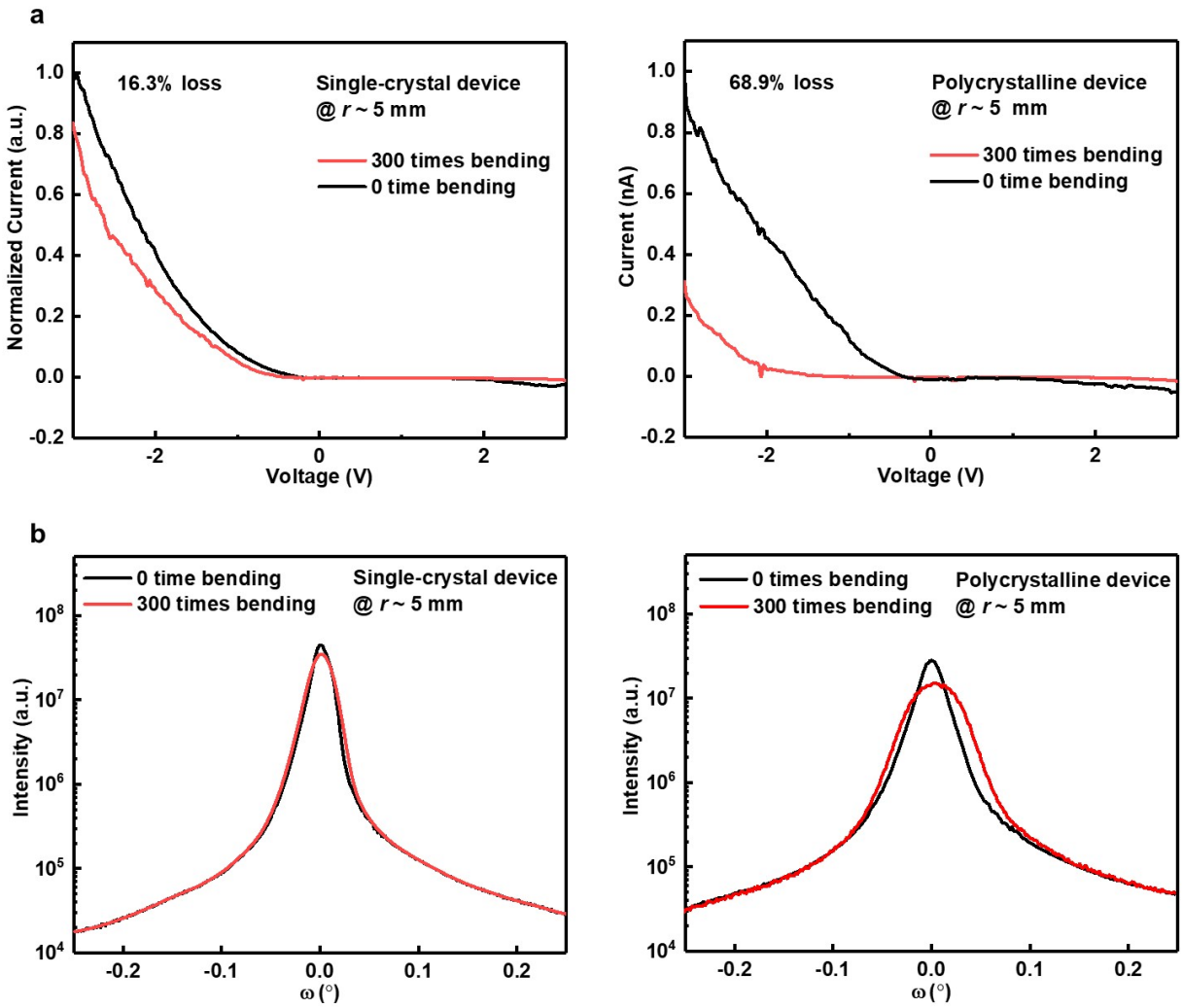

Supplementary Fig. 32 | Bending stability characterizations between single-crystal and polycrystalline structures. a, *I-V* measurement results of the single-crystal device (left) and the polycrystalline device (right). **b**, XRD ω scan measurement results of the single-crystal (left) and the polycrystalline (right). The single-crystal is more resistant to fatigue than the polycrystalline.

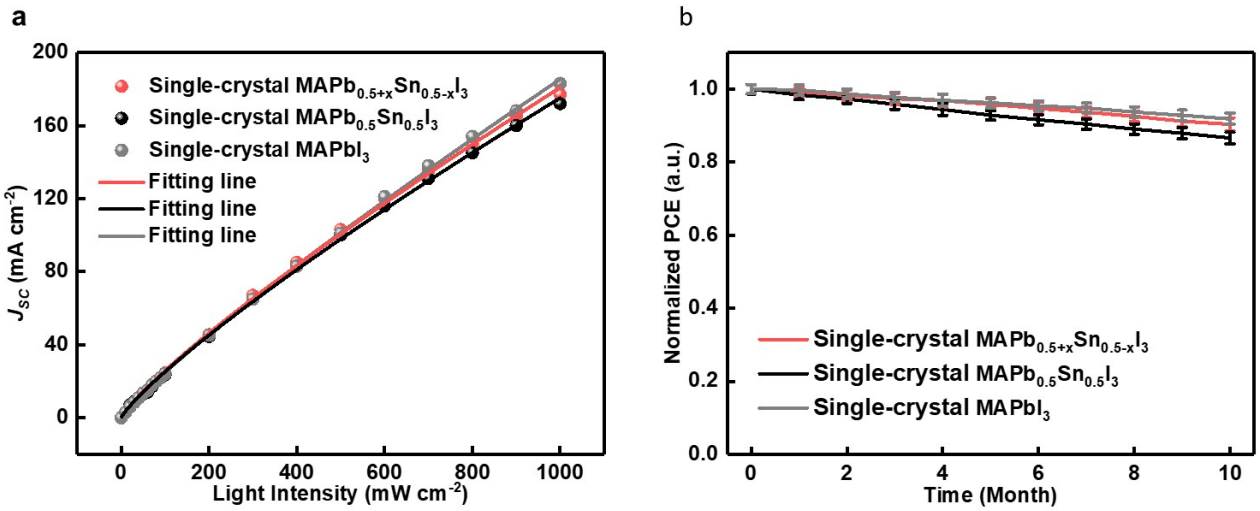

Supplementary Fig. 33 | Single-crystal photovoltaics stability measurements. a, Stress stability and **b**, long-term stability tests of three single-crystal photovoltaics with different compositions. The single-crystal devices show no obvious difference in stabilities. Error bars come from three different measurements with different aperture positions.

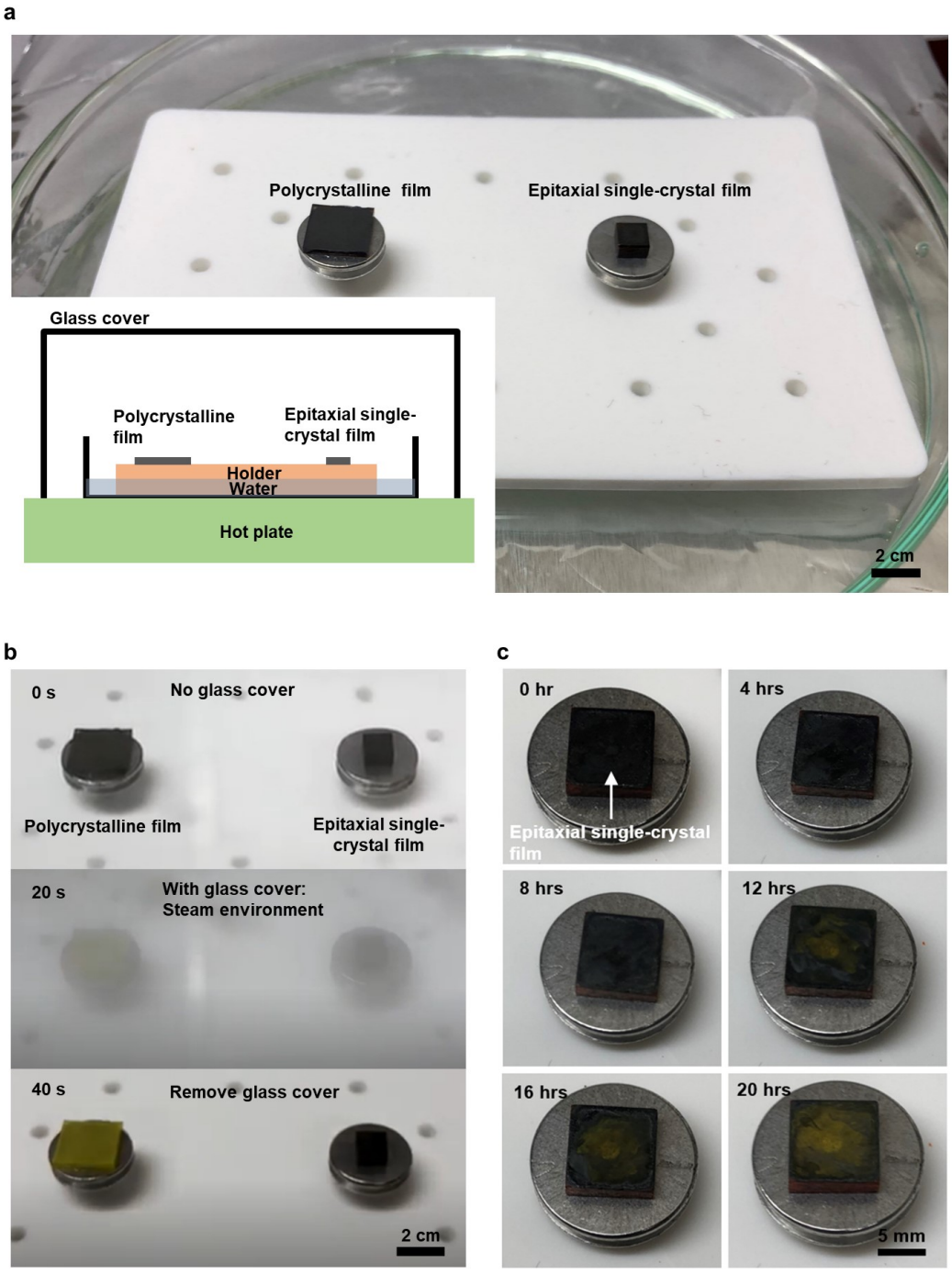

Supplementary Fig. 34 | Accelerated thermal and humidity tests. a, Experimental setups for thermal and humidity tests. The hot plate temperature is set to be 100 °C. Inset schematics show the entire setup, which gives a qualitative comparison between the polycrystalline $MAPb_{0.5}Sn_{0.5}I_3$ film and the single-crystal $MAPb_{0.5}Sn_{0.5}I_3$ film under hot and humid conditions. **b**, Polycrystalline $MAPb_{0.5}Sn_{0.5}I_3$ film exhibits rapid color change and phase transition while the single-crystal $MAPb_{0.5}Sn_{0.5}I_3$ film remains intact. **c**, Extended monitoring of the single-crystal $MAPb_{0.5}Sn_{0.5}I_3$ film under the same condition. The degradation rate of the single crystal is much slower than that of the procrystalline.

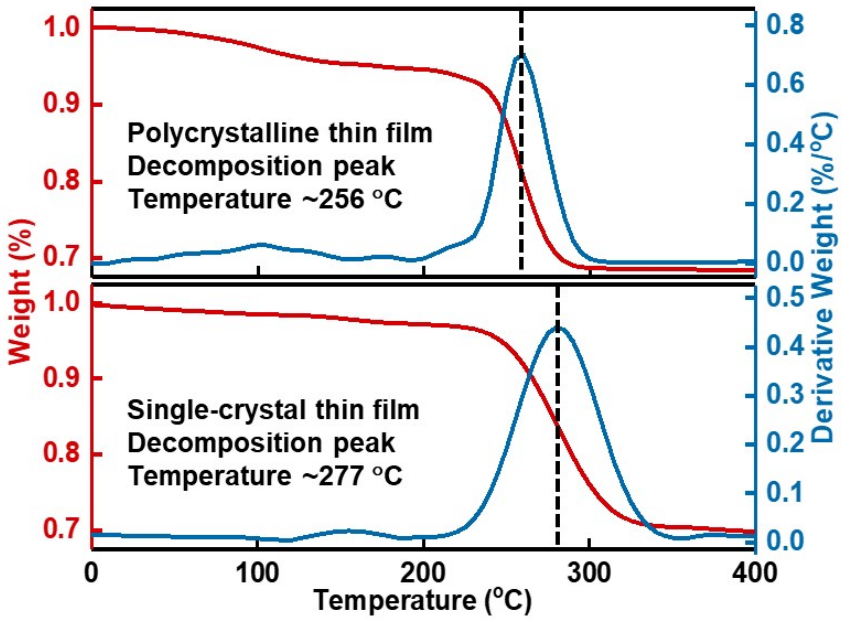

Supplementary Fig. 35 | Thermogravimetric analysis characterizations for the polycrystalline $MAPb_{0.5}Sn_{0.5}I_3$ and the graded single-crystal $MAPb_{0.5+x}Sn_{0.5-x}I_3$ films. The results show a faster degradation of the polycrystalline film at a lower decomposition temperature than the single-crystal film.

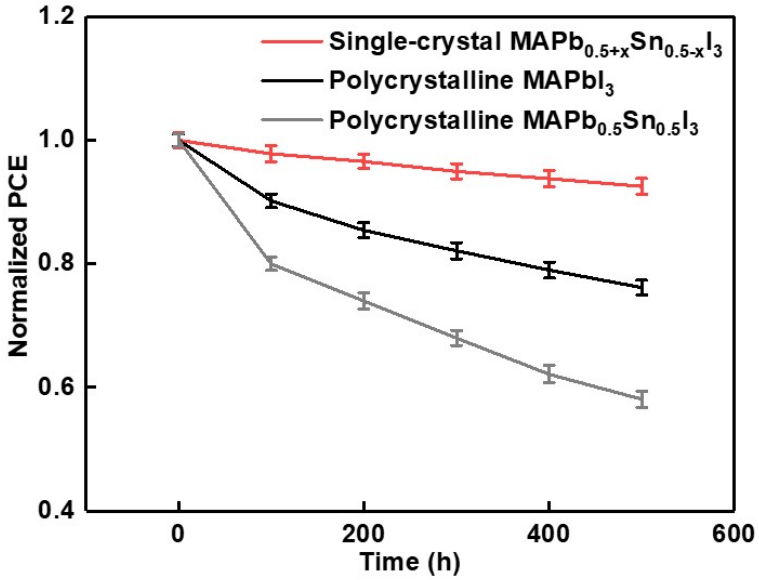

Supplementary Fig. 36 | Long-time continuous illumination stability tests with the PTAA as the HTL layer. The PTAA-based devices exhibit better thermal and light stability under the continuous illumination condition than the Spiro-based devices. Therefore, the difference between the perovskite structures can be more easily revealed. The single-crystal devices exhibit better device stability than the polycrystalline counterparts.

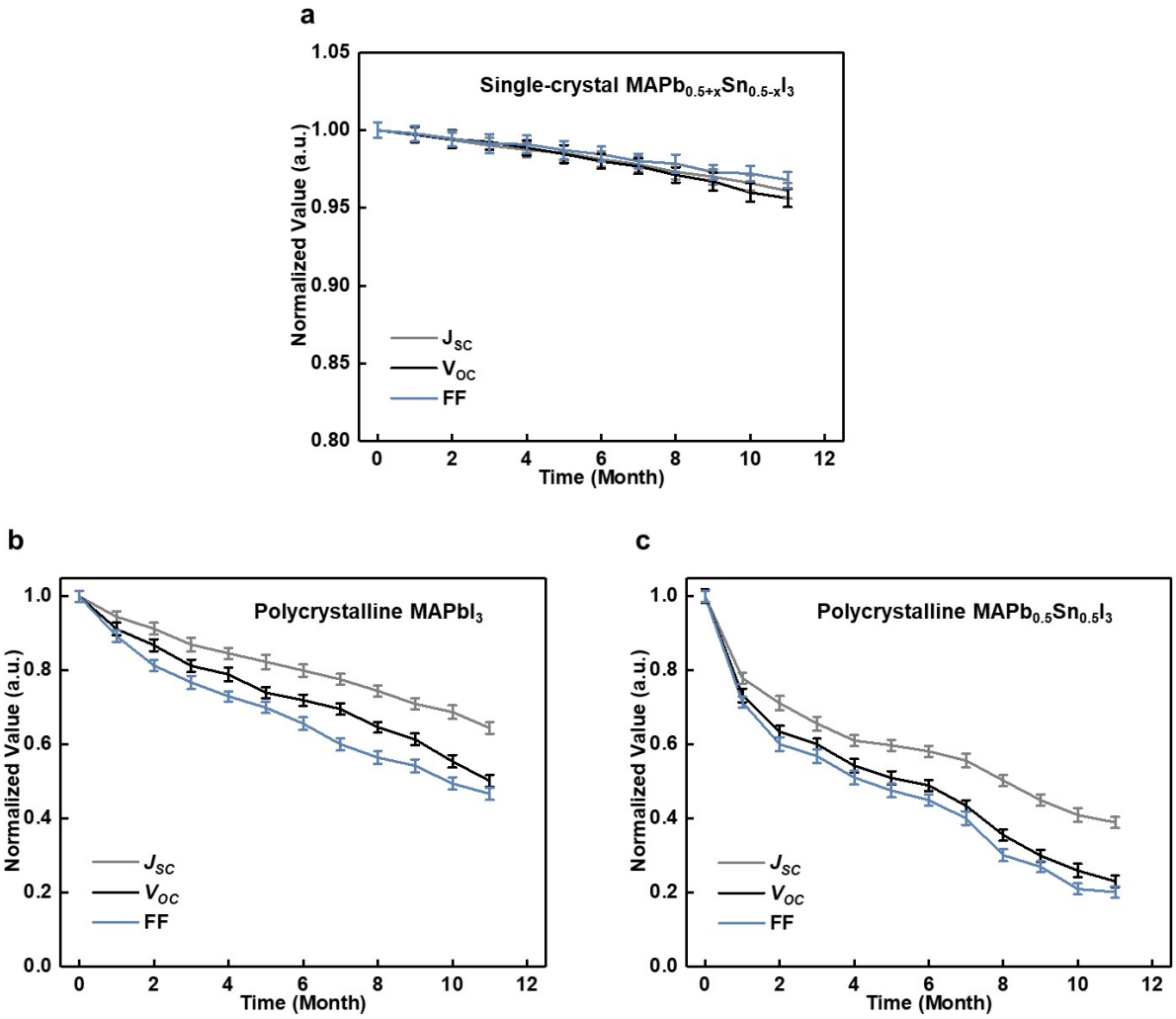

Supplementary Fig. 37 | Long-time stability measurements of photovoltaic devices. V_{OC}, J_{SC}, and FF data for PCE measurements in **a**, single-crystal $MAPb_{0.5+x}Sn_{0.5-x}I_3$, **b**, polycrystalline $MAPbI_3$, and c, polycrystalline $MAPb_{0.5}Sn_{0.5}I_3$ photovoltaic devices. Error bars come from three different measurements with different aperture positions.

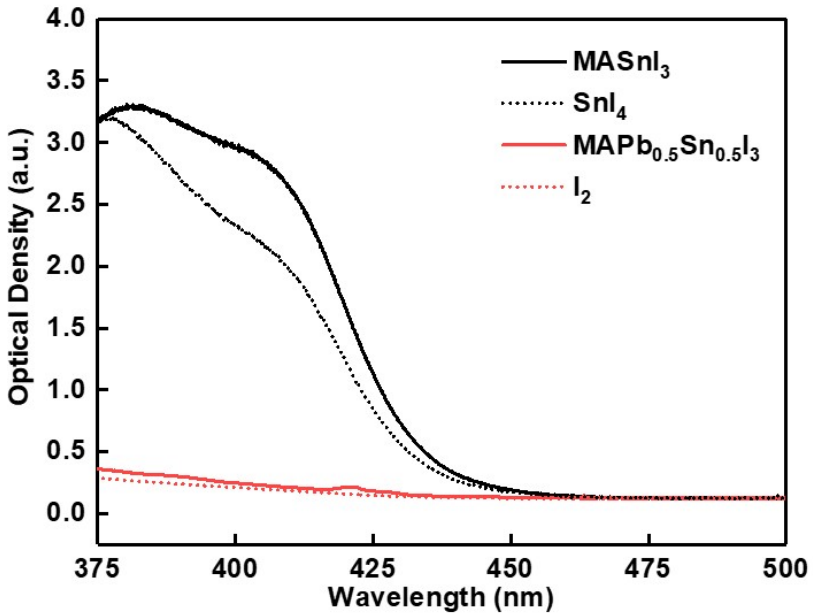

Supplementary Fig. 38 | Absorption measurements on single-crystal perovskite solutions. Purely Sn-based single-crystal perovskite and Pb-Sn mixed single-crystal perovskite exhibit different absorption peaks, indicating that the major by-products resulted from oxidations are different.

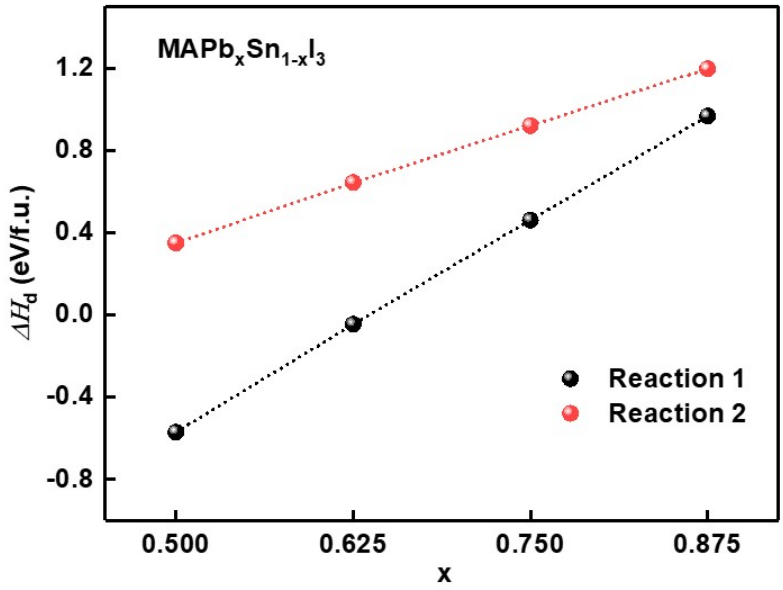

Supplementary Fig. 39 | Simulation results on decomposition enthalpies of different Pb-Sn ratios. In the Pb-Sn mixed system, reaction (1) is more favorable at any Pb-Sn ratios than reaction (2), which is consistent with the optical absorption results that the major by-products after oxidation are different from the purely Sn based system. Additionally, increasing the Pb ratio can further slow down the oxidation rate.

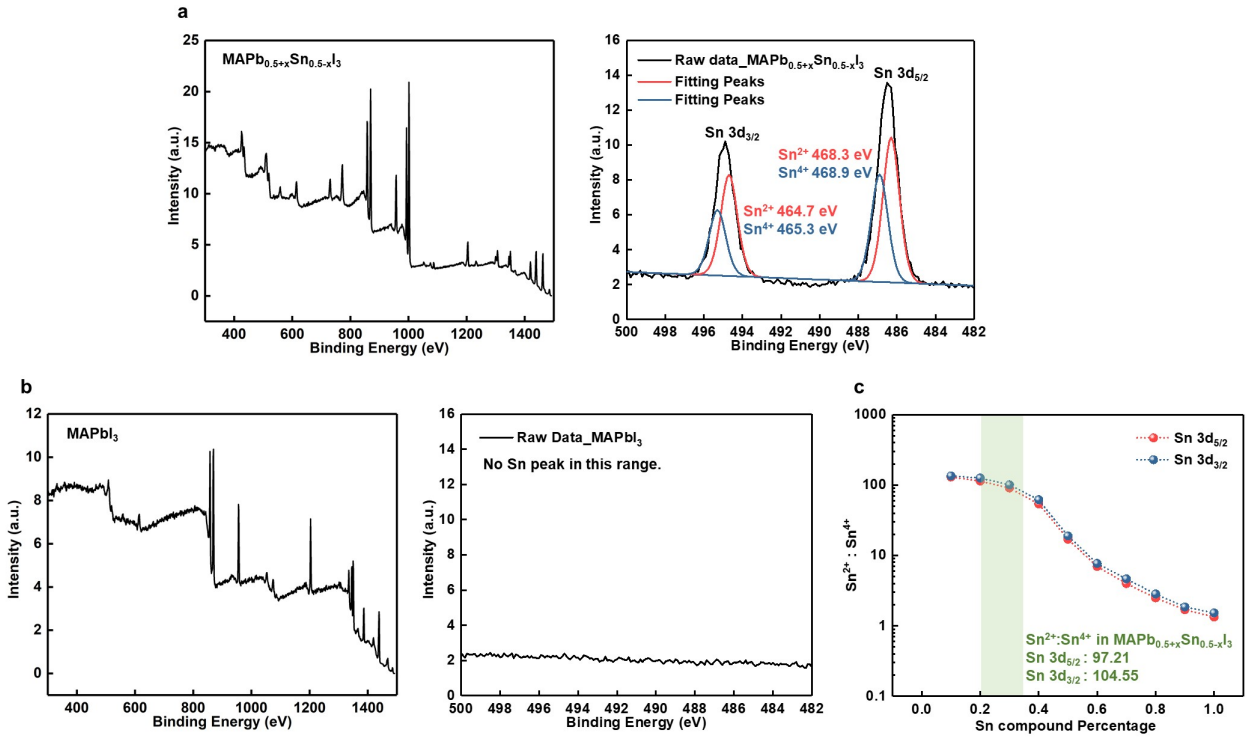

Supplementary Fig. 40 | XPS measurements with different Pb-Sn single-crystal compositions. a, XPS spectrum measured for single-crystal $MAPb_{0.5+x}Sn_{0.5-x}I_3$ (left) and zoom-in spectrum for typical Sn peaks in single-crystal $MASnI_3$ (right). Strong Sn^{2+} and Sn^{4+} peaks can be fitted. **b**, XPS spectrum measured for a control sample of single-crystal $MAPbI_3$ (left) and zoom-in spectrum for typical Sn peaks in single-crystal $MAPbI_3$ (right). No Sn peak can be found. **c**, Estimated Sn ratios in the single-crystal $MAPb_{0.5+x}Sn_{0.5-x}I_3$. The y-axis is the XPS peak ratio of Sn^{2+} to Sn^{4+}. We prepared and characterized samples with different Pb-Sn ratios using XPS. Under the same condition (preparation environment, transfer loading time, etc), increasing the Pb ratio can slow down the oxidation rate of Sn^{2+}. The shaded region is the estimated real Sn ratio in the graded single-crystal $MAPb_{0.5+x}Sn_{0.5-x}I_3$.

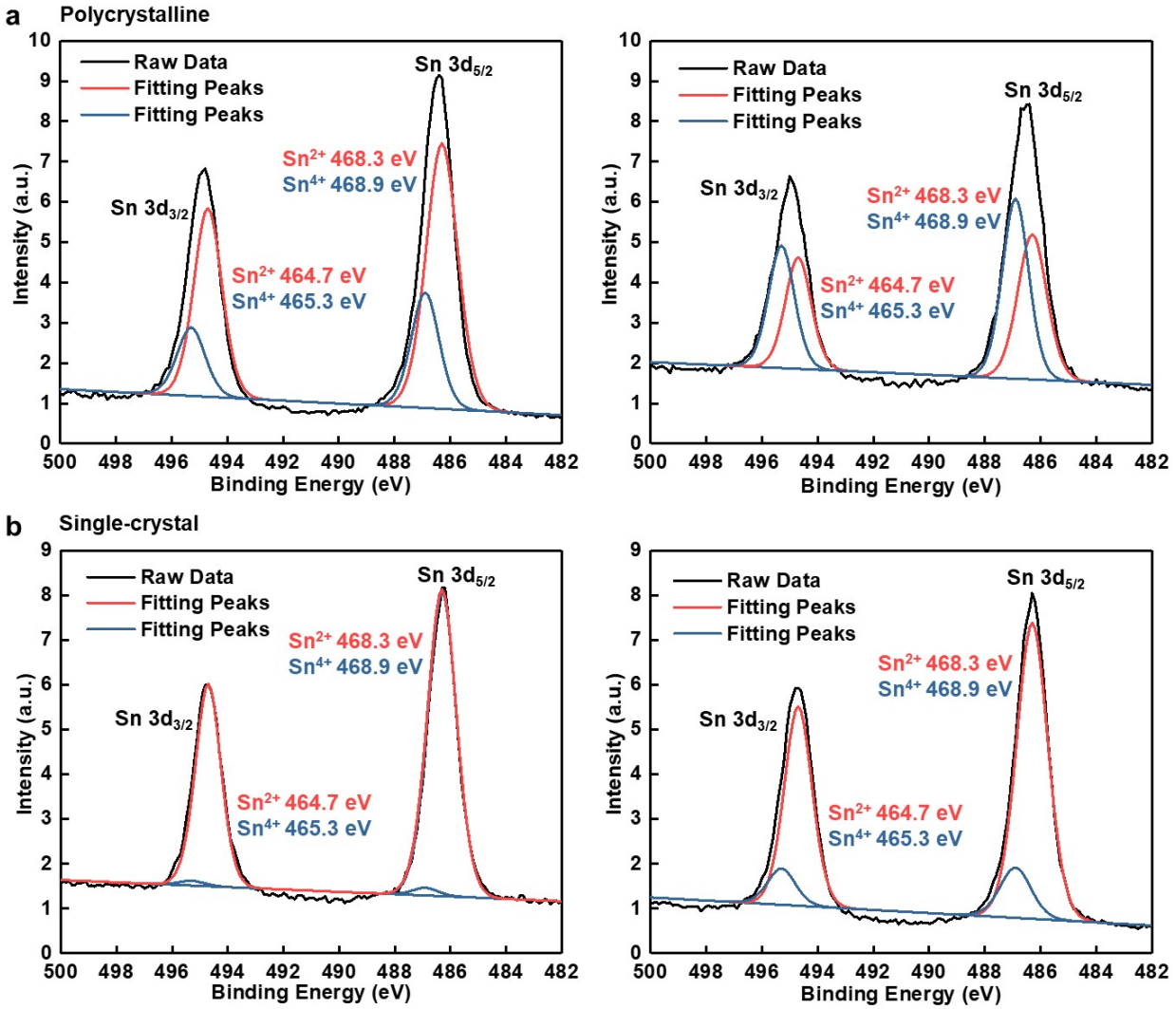

Supplementary Fig. 41 | Sn^{2+} oxidation mechanism studies with different crystal structures. **a**, XPS results of freshly prepared polycrystalline $MAPb_{0.5}Sn_{0.5}I_3$ (left) and aged polycrystalline $MAPb_{0.5}Sn_{0.5}I_3$ (right), where strong Sn^{4+} peaks can be fitted. **b**, XPS results of freshly prepared single-crystal $MAPb_{0.5}Sn_{0.5}I_3$ (left) and aged single-crystal $MAPb_{0.5}Sn_{0.5}I_3$ (right) under the same conditions, where the intensity of fitted Sn^{4+} peaks are much weaker than those in the polycrystalline samples, indicating the Sn^{2+} oxidation rate is much slower in the single-crystal than in the polycrystalline.

Single-crystal Thickness (μm)	J_{SC} (mA/cm^2)	V_{OC} (V)	FF (%)
~0.6	16.8	1.08	76
~0.9	17.4	1.07	76
~1.2	18.0	1.06	75
~1.5	18.7	1.06	74
~1.8	19.6	1.05	73
~2.1	20.1	1.03	72
~2.4	19.8	1.00	71

Supplementary Table 1. Absorber-thickness dependent photovoltaic performance. The data for each thickness is averaged from three separate devices. The thickness control is achieved by changing the growth time. All devices are in situ fabricated without transferring to isolate any possible confounding factors. The device structure is shown in Supplementary Fig. 15.

REFERENCES

1 Yang, W. S. et al. Iodide management in formamidinium-lead-halide-based perovskite layers for efficient solar cells. *Science* **356**, 1376-1379 (2017).

2 Lin, K. et al. Perovskite light-emitting diodes with external quantum efficiency exceeding 20 percent. *Nature* **562**, 245-248 (2018).

3 Feng, J. et al. Single-crystalline layered metal-halide perovskite nanowires for ultrasensitive photodetectors. *Nat. Electron.* **1**, 404-410 (2018).

4 NREL. *Best Research-Cell Efficiency Chart*.

5 Wang, Q. et al. Large fill-factor bilayer iodine perovskite solar cells fabricated by a low-temperature solution-process. *Energy Environ. Sci.* **7**, 2359-2365 (2014).

6 Chen, Z. et al. Thin single crystal perovskite solar cells to harvest below-bandgap light absorption. *Nat. Commun.* **8**, 1890 (2017).

7 Huang, Y. et al. The Exploration of Carrier Behavior in the Inverted Mixed Perovskite Single-Crystal Solar Cells. *Adv. Mater. Interfaces* **5**, 1800224 (2018).

8 Lee, L. et al. Wafer-scale single-crystal perovskite patterned thin films based on geometrically-confined lateral crystal growth. *Nat. Commun.* **8**, 15882 (2017).

9 Leblebici, S. Y. et al. Facet-dependent photovoltaic efficiency variations in single grains of hybrid halide perovskite. *Nat. Energy* **1**, 16093 (2016).

10 Zhang, W. et al. Enhanced optoelectronic quality of perovskite thin films with hypophosphorous acid for planar heterojunction solar cells. *Nat. Commun.* **6**, 10030 (2015).

11 Zheng, G. et al. Manipulation of facet orientation in hybrid perovskite polycrystalline films by cation cascade. *Nat. Commun.* **9**, 2793 (2018).

12 Zhao, Y. et al. Perovskite seeding growth of formamidinium-lead-iodide-based perovskites for efficient and stable solar cells. *Nat. Commun.* **9**, 1607 (2018).

13 Liu, Y. et al. Single-Crystal-like Perovskite for High-Performance Solar Cells Using the Effective Merged Annealing Method. *ACS Appl. Mater. Interfaces* **9**, 12382-12390 (2017).

14 Saidaminov, M. I. et al. High-quality bulk hybrid perovskite single crystals within minutes by inverse temperature crystallization. *Nat. Commun.* **6**, 7586 (2015).

15 Liu, M., Johnston, M. B. & Snaith, H. J. Efficient planar heterojunction perovskite solar cells by vapour deposition. *Nature* **501**, 395-398 (2013).

16 Chen, Z. et al. Single-Crystal $MAPbI_3$ Perovskite Solar Cells Exceeding 21% Power Conversion Efficiency. *ACS Energy Lett.* **4**, 1258-1259 (2019).

17 Lv, Q. et al. A universal top-down approach toward thickness-controllable perovskite single-crystalline thin films. *J. Mater. Chem. C* **6**, 4464-4470 (2018).

18 A decade of perovskite photovoltaics. *Nat. Energy* **4**, 1-1 (2019).

19 Lei, Y. et al. Controlled Homoepitaxial Growth of Hybrid Perovskites. *Adv Mater* **30**, e1705992 (2018).

20 Matthews, J. *Epitaxial growth*. (Elsevier, 2012).

21 Shi, D. et al. Low trap-state density and long carrier diffusion in organolead trihalide perovskite single crystals. *Science* **347**, 519-522 (2015).

22 Dong, Q. et al. Electron-hole diffusion lengths> 175 μm in solution-grown $CH_3NH_3PbI_3$ single crystals. *Science* **347**, 967-970 (2015).

23 Chen, Z. et al. Thin single crystal perovskite solar cells to harvest below-bandgap light absorption. *Nat. Commun.* **8**, 1890 (2017).

24 Wei, W. et al. Monolithic integration of hybrid perovskite single crystals with heterogenous substrate for highly sensitive X-ray imaging. *Nat. Photonics* **11**, 315 (2017).
25 Pearson, A. J. et al. Oxygen degradation in mesoporous $Al_2O_3/CH_3NH_3PbI_{3-x}Cl_x$ perovskite solar cells: kinetics and mechanisms. *Adv. Energy Mater.* **6**, 1600014 (2016).
26 Cowan, S. R., Roy, A. & Heeger, A. J. Recombination in polymer-fullerene bulk heterojunction solar cells. *Phys. Rev. B* **82**, 245207 (2010).
27 Olthof, S. & Meerholz, K. Substrate-dependent electronic structure and film formation of $MAPbI_3$ perovskites. *Sci. Rep.* **7**, 40267 (2017).
28 Climent-Pascual, E. et al. Influence of the substrate on the bulk properties of hybrid lead halide perovskite films. *J. Mater. Chem. A* **4**, 18153-18163 (2016).
29 Zhang, C. et al. Influence of different TiO_2 blocking films on the photovoltaic performance of perovskite solar cells. *Appl. Surf. Sci.* **388**, 82-88 (2016).
30 Fakharuddin, A., Schmidt- Mende, L., Garcia- Belmonte, G., Jose, R. & Mora- Sero, I. Interfaces in perovskite solar cells. *Adv. Energy Mater.* **7**, 1700623 (2017).
31 Furukawa, Y., Sato, M., Kitamura, K., Yajima, Y. & Minakata, M. Optical damage resistance and crystal quality of $LiNbO_3$ single crystals with various Li/Nb ratios. *J. Appl. Phys.* **72**, 3250-3254 (1992).
32 Liang, R., Bonn, D. & Hardy, W. Growth of high quality YBCO single crystals using $BaZrO_3$ crucibles. *Physica C: Superconductivity* **304**, 105-111 (1998).
33 Amano, H., Sawaki, N., Akasaki, I. & Toyoda, Y. Metalorganic vapor phase epitaxial growth of a high quality GaN film using an AlN buffer layer. *Appl. Phys. Lett.* **48**, 353-355 (1986).
34 Gfroerer, T. H. Photoluminescence in analysis of surfaces and interfaces. *Encyclopedia of analytical chemistry: applications, theory and instrumentation* (2006).
35 Zhang, D. et al. Atomic-resolution transmission electron microscopy of electron beam–sensitive crystalline materials. *Science* **359**, 675-679 (2018).
36 Tritt, T. M. *Thermal conductivity: theory, properties, and applications*. (Springer Science & Business Media, 2005).
37 Gantmakher, V. & Levinson, Y. *Carrier scattering in metals and semiconductors*. Vol. 19 (Elsevier, 2012).
38 Karakus, M. et al. Phonon–electron scattering limits free charge mobility in methylammonium lead iodide perovskites. *J. Phys. Chem. Lett.* **6**, 4991-4996 (2015).
39 Milot, R. L., Eperon, G. E., Snaith, H. J., Johnston, M. B. & Herz, L. M. Temperature-dependent charge- carrier dynamics in $CH_3NH_3PbI_3$ perovskite thin films. *Adv. Funct. Mater.* **25**, 6218-6227 (2015).
40 Biewald, A. et al. Temperature dependent ambipolar charge carrier mobility in large crystal hybrid halide perovskite thin films. *ACS Appl. Mater. Interfaces* (2019).
41 Filippetti, A., Mattoni, A., Caddeo, C., Saba, M. & Delugas, P. Low electron-polar optical phonon scattering as a fundamental aspect of carrier mobility in methylammonium lead halide $CH_3NH_3PbI_3$ perovskites. *Phys. Chem. Chem. Phys.* **18**, 15352-15362 (2016).
42 Liu, Y. et al. A 1300 mm^2 Ultrahigh- Performance Digital Imaging Assembly using High- Quality Perovskite Single Crystals. *Adv. Mater.* **30**, 1707314 (2018).
43 Liu, Y. et al. 120 mm single-crystalline perovskite and wafers: towards viable applications. *Sci. China Chem.* **60**, 1367-1376 (2017).
44 Klug, H. P. & Alexander, L. E. X-ray diffraction procedures: for polycrystalline and

amorphous materials. *X-Ray Diffraction Procedures: For Polycrystalline and Amorphous Materials, 2nd Edition, by Harold P. Klug, Leroy E. Alexander, pp. 992. ISBN 0-471-49369-4. Wiley-VCH, May 1974.*, 992 (1974).

45 Liu, Y. et al. Thinness- and shape- controlled growth for ultrathin single- crystalline perovskite wafers for mass production of superior photoelectronic devices. *Adv. Mater.* **28**, 9204-9209 (2016).

46 Stranks, S. D. et al. Electron-hole diffusion lengths exceeding 1 micrometer in an organometal trihalide perovskite absorber. *Science* **342**, 341-344 (2013).

47 Xing, G. et al. Long-range balanced electron-and hole-transport lengths in organic-inorganic $CH_3NH_3PbI_3$. *Science* **342**, 344-347 (2013).

48 Nie, W. et al. High-efficiency solution-processed perovskite solar cells with millimeter-scale grains. *Science* **347**, 522-525 (2015).

49 Liu, Z. et al. Gas-solid reaction based over one-micrometer thick stable perovskite films for efficient solar cells and modules. *Nat. Commun.* **9**, 3880 (2018).

50 Park, N.-G. Perovskite solar cells: an emerging photovoltaic technology. *Mater. Today* **18**, 65-72 (2015).

51 Chen, Z. et al. Thin single crystal perovskite solar cells to harvest below-bandgap light absorption. *Nat. Commun.* **8**, 1-7 (2017).

52 Yang, Y. et al. Top and bottom surfaces limit carrier lifetime in lead iodide perovskite films. *Nat. Energy* **2**, 16207 (2017).

53 Unger, E. L. et al. Hysteresis and transient behavior in current–voltage measurements of hybrid-perovskite absorber solar cells. *Energy Environ. Sci.* **7**, 3690-3698 (2014).

54 Correa-Baena, J.-P. et al. Identifying and suppressing interfacial recombination to achieve high open-circuit voltage in perovskite solar cells. *Energy Environ. Sci.* **10**, 1207-1212 (2017).

55 Wolff, C. M. et al. Reduced Interface- Mediated Recombination for High Open- Circuit Voltages in $CH_3NH_3PbI_3$ Solar Cells. *Adv. Mater.* **29**, 1700159 (2017).

56 O'Malley, K. M., Li, C. Z., Yip, H. L. & Jen, A. K. Y. Enhanced open- circuit voltage in high performance polymer/fullerene bulk- heterojunction solar cells by cathode modification with a C_{60} surfactant. *Adv. Energy Mater.* **2**, 82-86 (2012).

57 Leijtens, T. et al. Carrier trapping and recombination: the role of defect physics in enhancing the open circuit voltage of metal halide perovskite solar cells. *Energy Environ. Sci.* **9**, 3472-3481 (2016).

58 de Quilettes, D. W. et al. Impact of microstructure on local carrier lifetime in perovskite solar cells. *Science* **348**, 683-686 (2015).

59 Wu, X. et al. Trap states in lead iodide perovskites. *J. Am. Chem. Soc.* **137**, 2089-2096 (2015).

60 Chen, Q. et al. Controllable self-induced passivation of hybrid lead iodide perovskites toward high performance solar cells. *Nano Lett.* **14**, 4158-4163 (2014).

61 Noel, N. K. et al. Enhanced photoluminescence and solar cell performance via Lewis base passivation of organic–inorganic lead halide perovskites. *ACS Nano* **8**, 9815-9821 (2014).

62 Zheng, X. et al. Defect passivation in hybrid perovskite solar cells using quaternary ammonium halide anions and cations. *Nat. Energy* **2**, 17102 (2017).

63 Jiang, Q. et al. Surface passivation of perovskite film for efficient solar cells. *Nat. Photonics*, 1 (2019).

64 Li, B. et al. Surface passivation engineering strategy to fully-inorganic cubic $CsPbI_3$ perovskites for high-performance solar cells. *Nat. Commun.* **9**, 1076 (2018).
65 Tan, H. et al. Efficient and stable solution-processed planar perovskite solar cells via contact passivation. *Science* **355**, 722-726 (2017).
66 Gere, J. M. & Goodno, B. J. Mechanics of Materials 5th. *Brooks Cole*, 780 (2001).
67 Ćirić, L. et al. Mechanical response of $CH_3NH_3PbI_3$ nanowires. *Appl. Phys. Lett.* **112**, 111901 (2018).
68 Zu, F. et al. Constructing the Electronic Structure of $CH_3NH_3PbI_3$ and $CH_3NH_3PbBr_3$ Perovskite Thin Films from Single-Crystal Band Structure Measurements. *J. Phys. Chem. Lett.* **10**, 601-609 (2019).
69 Endres, J. et al. Valence and conduction band densities of states of metal halide perovskites: a combined experimental–theoretical study. *J. Phys. Chem. Lett.* **7**, 2722-2729 (2016).
70 Kresse, G. & Furthmüller, J. Efficient iterative schemes for ab initio total-energy calculations using a plane-wave basis set. *Phys. Rev. B* **54**, 11169 (1996).
71 Perdew, J. P., Burke, K. & Ernzerhof, M. Generalized gradient approximation made simple. *Phys. Rev. Lett.* **77**, 3865 (1996).
72 Setyawan, W. & Curtarolo, S. High-throughput electronic band structure calculations: Challenges and tools. *Comput. Mater. Sci.* **49**, 299-312 (2010).
73 Cai, S. in *IOP Conf. Ser. Earth Environ. Sci.* 022038 (IOP Publishing).
74 Bokdam, M. et al. Role of polar phonons in the photo excited state of metal halide perovskites. *Sci. Rep.* **6**, 1-8 (2016).
75 Yan, W. et al. Increasing open circuit voltage by adjusting work function of hole-transporting materials in perovskite solar cells. *Nano Res.* **9**, 1600-1608 (2016).
76 Suarez, B. et al. Recombination study of combined halides (Cl, Br, I) perovskite solar cells. *J. Phys. Chem. Lett.* **5**, 1628-1635 (2014).
77 Yan, W. et al. High-performance hybrid perovskite solar cells with open circuit voltage dependence on hole-transporting materials. *Nano Energy* **16**, 428-437 (2015).
78 Yang, Z. et al. Stable Low- Bandgap Pb–Sn Binary Perovskites for Tandem Solar Cells. *Adv. Mater.* **28**, 8990-8997 (2016).
79 Alshekhli, B. A. Theoretical Analysis of $Al_xGa_{1-x}As$/GaAs Graded Band Gap Solar Cell. *Al-Nahrain J. Sci.* **14**, 66-72 (2011).
80 Dullweber, T., Rau, U. & Schock, H. A new approach to high-efficiency solar cells by band gap grading in Cu (In, Ga) Se2 chalcopyrite semiconductors. *Sol. Energy Mater. Sol. Cells* **67**, 145-150 (2001).
81 Feng, J. Mechanical properties of hybrid organic-inorganic CH3NH3BX3 (B= Sn, Pb; X= Br, I) perovskites for solar cell absorbers. *APL Mater.* **2**, 081801 (2014).
82 Faghihnasiri, M., Izadifard, M. & Ghazi, M. E. DFT study of mechanical properties and stability of cubic methylammonium lead halide perovskites ($CH_3NH_3PbX_3$, X= I, Br, Cl). *J. Phys. Chem. C* **121**, 27059-27070 (2017).
83 Saraf, R., Tsui, T. & Maheshwari, V. Modulation of Mechanical Properties and Stable Light Energy Harvesting by Poling in Polymer Integrated Perovskite Films: A Wide Range, Linear and Highly Sensitive Tactile Sensor. *J. Mater. Chem. A* (2019).
84 Rakita, Y., Cohen, S. R., Kedem, N. K., Hodes, G. & Cahen, D. Mechanical properties of $APbX_3$ (A= Cs or CH_3NH_3; X= I or Br) perovskite single crystals. *MRS Commun.* **5**, 623-629 (2015).

85 Sun, S. et al. Factors influencing the mechanical properties of formamidinium lead halides and related hybrid perovskites. *ChemSusChem* **10**, 3740-3745 (2017).
86 Yu, J., Wang, M. & Lin, S. Probing the soft and nanoductile mechanical nature of single and polycrystalline organic–inorganic hybrid perovskites for flexible functional devices. *Acs Nano* **10**, 11044-11057 (2016).
87 Rösler, J., Harders, H. & Baeker, M. *Mechanical behaviour of engineering materials: metals, ceramics, polymers, and composites*. (Springer Science & Business Media, 2007).
88 Mezeix, L. & Green, D. J. Comparison of the mechanical properties of single crystal and polycrystalline yttrium aluminum garnet. *Int. J. Appl. Ceram. Technol.* **3**, 166-176 (2006).
89 Park, N.-G., Grätzel, M., Miyasaka, T., Zhu, K. & Emery, K. Towards stable and commercially available perovskite solar cells. *Nat. Energy* **1**, 16152 (2016).
90 Rong, Y. et al. Challenges for commercializing perovskite solar cells. *Science* **361**, eaat8235 (2018).
91 Rong, Y., Liu, L., Mei, A., Li, X. & Han, H. Beyond efficiency: the challenge of stability in mesoscopic perovskite solar cells. *Adv. Energy Mater.* **5**, 1501066 (2015).
92 Li, X. et al. Improved performance and stability of perovskite solar cells by crystal crosslinking with alkylphosphonic acid ω-ammonium chlorides. *Nat. Chem.* **7**, 703 (2015).
93 Deng, W. et al. Aligned single- crystalline perovskite microwire arrays for high- performance flexible image sensors with long- term stability. *Adv. Mater.* **28**, 2201-2208 (2016).
94 Futscher, M. H. et al. Quantification of ion migration in $CH_3NH_3PbI_3$ perovskite solar cells by transient capacitance measurements. *Mater. Horiz.* (2019).
95 Yun, J. S. et al. Critical role of grain boundaries for ion migration in formamidinium and methylammonium lead halide perovskite solar cells. *Adv. Energy Mater.* **6**, 1600330 (2016).
96 Shao, Y. et al. Grain boundary dominated ion migration in polycrystalline organic–inorganic halide perovskite films. *Energy Environ. Sci.* **9**, 1752-1759 (2016).
97 Ball, J. M. & Petrozza, A. Defects in perovskite-halides and their effects in solar cells. *Nat. Energy* **1**, 16149 (2016).
98 Sherkar, T. S. et al. Recombination in perovskite solar cells: significance of grain boundaries, interface traps, and defect ions. *ACS Energy Lett.* **2**, 1214-1222 (2017).
99 Azpiroz, J. M., Mosconi, E., Bisquert, J. & De Angelis, F. Defect migration in methylammonium lead iodide and its role in perovskite solar cell operation. *Energy Environ. Sci.* **8**, 2118-2127 (2015).
100 Yuan, Y. et al. Electric- field- driven reversible conversion between Methylammonium lead triiodide perovskites and lead iodide at elevated temperatures. *Adv. Energy Mater.* **6**, 1501803 (2016).
101 Seto, J. Y. The electrical properties of polycrystalline silicon films. *J. Appl. Phys.* **46**, 5247-5254 (1975).
102 Liu, L. et al. Grain- Boundary "Patches" by In Situ Conversion to Enhance Perovskite Solar Cells Stability. *Adv. Mater.* **30**, 1800544 (2018).
103 Sun, Q. et al. Role of microstructure in oxygen induced photodegradation of methylammonium lead triiodide perovskite films. *Adv. Energy Mater.* **7**, 1700977 (2017).
104 Shi, J., Xu, X., Li, D. & Meng, Q. Interfaces in perovskite solar cells. *Small* **11**, 2472-2486 (2015).

105 Ono, L. K., Qi, Y. & Liu, S. F. Progress toward stable lead halide perovskite solar cells. *Joule* **2**, 1961-1990 (2018).
106 Hawash, Z., Ono, L. K. & Qi, Y. Recent Advances in Spiro- MeOTAD Hole Transport Material and Its Applications in Organic–Inorganic Halide Perovskite Solar Cells. *Adv. Mater. Interfaces* **5**, 1700623 (2018).
107 Jeon, N. J. et al. A fluorene-terminated hole-transporting material for highly efficient and stable perovskite solar cells. *Nat. Energy* **3**, 682-689 (2018).
108 Xing, J. et al. Ultrafast ion migration in hybrid perovskite polycrystalline thin films under light and suppression in single crystals. *Phys. Chem. Chem. Phys.* **18**, 30484-30490 (2016).
109 Egger, D. A., Edri, E., Cahen, D. & Hodes, G. (ACS Publications, 2015).
110 Eames, C. et al. Ionic transport in hybrid lead iodide perovskite solar cells. *Nat. Commun.* **6**, 1-8 (2015).
111 Rajagopal, A., Yao, K. & Jen, A. K. Y. Toward perovskite solar cell commercialization: a perspective and research roadmap based on interfacial engineering. *Adv. Mater.* **30**, 1800455 (2018).
112 Berhe, T. A. et al. Organometal halide perovskite solar cells: degradation and stability. *Energy Environ. Sci.* **9**, 323-356 (2016).
113 Azpiroz, J. M., Mosconi, E., Bisquert, J. & De Angelis, F. Defect migration in methylammonium lead iodide and its role in perovskite solar cell operation. *Energy & Environmental Science* **8**, 2118-2127 (2015).
114 Haruyama, J., Sodeyama, K., Han, L. & Tateyama, Y. First-principles study of ion diffusion in perovskite solar cell sensitizers. *J. Am. Chem. Soc.* **137**, 10048-10051 (2015).
115 Meloni, S. et al. Ionic polarization-induced current–voltage hysteresis in $CH_3NH_3PbX_3$ perovskite solar cells. *Nat. Commun.* **7**, 1-9 (2016).
116 Futscher, M. H. et al. Quantification of ion migration in $CH_3NH_3PbI_3$ perovskite solar cells by transient capacitance measurements. *Mater. Horiz.* **6**, 1497-1503 (2019).
117 Hao, F., Stoumpos, C. C., Chang, R. P. & Kanatzidis, M. G. Anomalous band gap behavior in mixed Sn and Pb perovskites enables broadening of absorption spectrum in solar cells. *J. Am. Chem. Soc.* **136**, 8094-8099 (2014).
118 Leijtens, T., Prasanna, R., Gold-Parker, A., Toney, M. F. & McGehee, M. D. Mechanism of tin oxidation and stabilization by lead substitution in tin halide perovskites. *ACS Energy Lett.* **2**, 2159-2165 (2017).
119 Zuo, F. et al. Binary- Metal Perovskites Toward High- Performance Planar-Heterojunction Hybrid Solar Cells. *Adv. Mater.* **26**, 6454-6460 (2014).
120 Liu, X. et al. Improved efficiency and stability of Pb–Sn binary perovskite solar cells by Cs substitution. *J. Mater. Chem. A* **4**, 17939-17945 (2016).
121 Li, Y. et al. 50% Sn- Based Planar Perovskite Solar Cell with Power Conversion Efficiency up to 13.6%. *Adv. Energy Mater.* **6**, 1601353 (2016).
122 Yang, Z. et al. Stabilized wide bandgap perovskite solar cells by tin substitution. *Nano Lett.* **16**, 7739-7747 (2016).
123 Eperon, G. E. et al. Perovskite-perovskite tandem photovoltaics with optimized band gaps. *Science* **354**, 861-865 (2016).
124 Boyd, C. C., Cheacharoen, R., Leijtens, T. & McGehee, M. D. Understanding degradation mechanisms and improving stability of perovskite photovoltaics. *Chem. Rev.* **119**, 3418-3451 (2018).

125 Leijtens, T., Bush, K. A., Prasanna, R. & McGehee, M. D. Opportunities and challenges for tandem solar cells using metal halide perovskite semiconductors. *Nat. Energy* **3**, 828 (2018).
126 Saidaminov, M. I. et al. Planar-integrated single-crystalline perovskite photodetectors. *Nat. Commun.* **6**, 8724 (2015).
127 Maculan, G. et al. $CH_3NH_3PbCI_3$ single crystals: inverse temperature crystallization and visible-blind UV-photodetector. *J. Phys. Chem. Lett.* **6**, 3781-3786 (2015).
128 Liu, Y. et al. Multi-inch single-crystalline perovskite membrane for high-detectivity flexible photosensors. *Nat. Commun.* **9** (2018).
129 Wang, S., Jiang, Y., Juarez-Perez, E. J., Ono, L. K. & Qi, Y. Accelerated degradation of methylammonium lead iodide perovskites induced by exposure to iodine vapour. *Nat. Energy* **2**, 1-8 (2016).